MICROWAVE DIELECTRIC MEASUREMENTS ON MEM(TCNQ)$_2$ AND TTF-TCNQ

by

MICHAEL ROBERT MORROW

B.Sc. McMaster University, 1977

A THESIS SUBMITTED IN PARTIAL FULFILLMENT

OF THE REQUIREMENTS FOR THE DEGREE OF

MASTER OF SCIENCE

in

THE FACULTY OF GRADUATE STUDIES

DEPARTMENT OF PHYSICS

We accept this thesis as conforming

to the required standard

THE UNIVERSITY OF BRITISH COLUMBIA

November, 1979

In presenting this thesis in partial fulfilment of the requirements for an advanced degree at the University of British Columbia, I agree that the Library shall make it freely available for reference and study. I further agree that permission for extensive copying of this thesis for scholarly purposes may be granted by the Head of my Department or by his representatives. It is understood that copying or publication of this thesis for financial gain shall not be allowed without my written permission.

Department of Physics

The University of British Columbia
2075 Wesbrook Place
Vancouver, Canada
V6T 1W5

Date November 19/1979

ABSTRACT

The microwave dielectric constant and conductivity of $MEM(TCNQ)_2$ were studied in the neighbourhood of the monomer to dimer transition at 61°C using cavity-perturbation techniques at 9 GHz. The conductivity was found to be in general agreement with four-probe d.c. results. Thus, doubts about the reliability of the d.c. measurements above the destructive transition have been removed.

The complex dielectric constant of TTF-TCNQ at liquid helium temperatures was studied using dielectric resonance techniques. Some anomalies regarding the interpretation of the dielectric resonance mode plots were resolved. Values for ϵ_b' of $(3.0\pm0.4)X10^3$ and for ϵ_a' of greater than 9 were implied by the results.

Finally, preliminary results and proposed directions for a bolometric absorption measurement in TTF-TCNQ in the microwave bands are presented. This technique may prove useful for the direct observation of the pinned charge density wave in TTF-TCNQ.

TABLE OF CONTENTS

LIST OF TABLES

LIST OF FIGURES

ACKNOWLEDGEMENTS

I would like to acknowledge the support and direction of Dr. W.N. Hardy in his supervision of this project. I have also been aided by numerous discussions with Dr. A.J. Berlinsky. Dr. Larry Weiler and his group provided many of the crystals studied in these experiments and I would also like to thank them. The helpful suggestions and technical assistance of Dr. J. Carolan and Dr. J. Eldridge are also gratefully acknowledged. I also wish to thank all of the members of the microwave group for their support and assistance. B. Statt is to be thanked particularly for his invaluable assistance with the computer controlled spectrometer.

I would also like to thank the Natural Sciences and Engineering Research Council for their support in the form of a Science Scholarship.

CHAPTER I

Introduction

In this section we will begin by commenting on quasi-one-dimensional TCNQ salts in general with some discussion of the Peierl's transition, charge density wave formation, and Frohlich superconductivity. We will then describe $MEM(TCNQ)_2$ and, in connection with it, models of one-dimensional stacks in which Coulomb interactions are important. This will serve as introduction for the first part of this work. Finally we will consider TTF-TCNQ , the subject of the second part of this work, and, in particular, the dielectric constant appropriate to the pinned charge density wave model of TTF-TCNQ.

1.1 Quasi-One-Dimensional TCNQ Salts

There are now a large number of charge transfer salts based on the organic electron acceptor, tetracyanoquinodimethane, (TCNQ). These are predominantly 1:1 salts, such as TTF-TCNQ, or 1:2 salts, like MEM$(TCNQ)_2$. A common feature of most of these materials is that the planar TCNQ molecules, seen in Fig. 1, form stacks in which the overlap of the π molecular orbitals is significant. Some planar donor molecules, like tetrathiofulvalene, (TTF), can also form stacks. The interactions of stacks in directions perpendicular to the stacking axis, while strong enough to determine a three-dimensional structure, are usually considerably weaker than those along the stacks. These highly anisotropic materials thus offer the possibility of studying the effects of interactions in one dimension and are often described by the term quasi-one-dimensional.

This name reflects the fact that real systems cannot be purely one-dimensional. In a system with short range interactions and only one dimension, fluctuations will prevent the system from existing in a phase with long range order at any non-zero temperature. This comes about because the contact between regions of differing order parameter is a point and the surface energy involved in creation of such a boundary is independent of the size of the differing region. The entropy

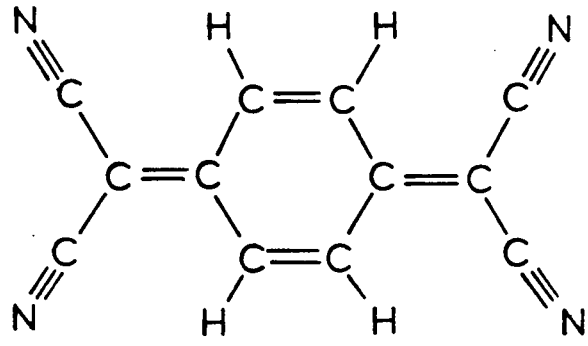

TCNQ

Figure 1. The organic acceptor molecule TCNQ.

contribution to the change in the free energy for creating a boundary somewhere along a chain of M sites goes as TlnM. For large M, this entropy change will always dominate the surface energy increase and the system will be able to lower its free energy by creating boundaries.(Emery,1977).

The fact that phase transitions will not occur in a one-dimensional system does not invalidate the interest in one-dimensional phenomena. In a real quasi-one-dimensional system, the coupling of fluctuations on neighbouring one-dimensional chains can lead to ordering in three dimensions. We go on, then, to discuss briefly some of the properties of purely one-dimensional chains with the implicit understanding that, in any real system, the three-dimensional nature of the lattice would play a part in any phase transition observed.

Perhaps the best known feature of one-dimensional models is the Peierls instability (Peierls ,1955). In a purely one-dimensional system with no interactions and less than 2 electrons per site, the lowest band will be filled up to $k=\pm k_F^o$, where the Fermi vector is given by

(1.1) $$k_F^o = NG_{\|} / 4N_o .$$

Here, N is the number of electrons, N_o the number of sites, each of which can accomodate two electrons, and $G_{\|} = 2\pi/d_{\|}$ is the reciprocal lattice vector for a chain with sites separated by $d_{\|}$. This situation describes a partially filled free electron band and thus a one dimensional metal. The kinetic energy

associated with the electrons near $k=k_F^\circ$ can be lowered if a gap is opened at that point. Such a gap is opened by $2k_F^\circ$ distortions of the electronic system. One thus expects a density fluctuation of wave vector $2k_F^\circ$ to form for a vanishingly small component of the applied potential. This is expressed in terms of the electronic density response function at wave vector q, $\chi(q)$, which measures the ratio of the density fluctuations at q to the component of the applied potential at that wave vector. Toombs (1978) and Berlinsky (1979) discuss the form of $\chi(2k_F^\circ)$. They show that, at low temperatures, it is negative and goes as ln(T).

The force on the lattice includes a term involving $\chi(q)$. Toombs gives the frequency for phonons of wave vector q, $\Omega(q)$, as

$$\Omega^2(q) = \omega_q^2 + (2g^2\omega_q/N\hbar)\chi(q) \tag{1.2}$$

where g is the electron-phonon coupling constant, ω_q is the unperturbed phonon frequency, and N is the number of sites. In this case, $\chi(q)$ is describing the response of the electrons to the perturbation due to phonons of wavevector q. The first term can be thought of as a restoring force due to the lattice itself and the second as a force due to the conduction electrons. Because $\chi(2k_F^\circ)$ is negative and increasing as T is lowered, there will be a temperature, T_o, at which $\Omega^2(2k_F^\circ)$ goes to zero. Berlinsky (1979) shows that the form of $\Omega^2(2k_F^\circ)$ above T_o is given by

$$\Omega^{a}(2k_F^{o}) = (g^{a}\omega_{2k_F^{o}}/\epsilon_F)\ln(T/T_o).$$

He further states that, for $T<T_o$, the $2k_F^{o}$ distortion is static and a gap opens in the electronic spectrum. This softening of the $2k_F^{o}$ phonon is referred to as the Kohn anomaly. Other mechanisms for distorting the lattice will be discussed when we describe the use of the Hubbard model to deal with Coulomb interactions in reference to $MEM(TCNQ)_2$.

Frohlich (1954) has shown that, for a jellium model, the translational invariance of the positive background gives no preferred position for the distortion and allows it to propagate as a sliding charge density wave with only weak attenuation due to scattering from phonons. This situation also applies if the charge transfer does not result in the number of sites being an integral multiple of the number of electrons. The new unit cell brought about by the distortion will be infinite in length and there will be no preferred position for the distortion. The distortion and lattice are said to be incommensurate. In reality, the charge density wave, if not commensurate with the lattice, is susceptible to pinning by impurities, defects, or three-dimensional ordering. (Lee, Rice, and Anderson , 1974). The effect of such a pinned mode on the low frequency electrical properties of a material will be discussed below in relation to TTF-TCNQ.

1.2 $MEM(TCNQ)_2$ and the Effect of Interactions on TCNQ Stacks

1.2a $MEM(TCNQ)_2$

Methylethylmorpholinium Tetracyanoquinodimethane, $MEM(TCNQ)_2$, is an organic semi-conductor with a room temperature conductivity of about 10^{-3} $(\Omega\text{-cm})^{-1}$ and an activation energy of about 0.4eV. It has been a source of some interest lately because of its unambiguous charge transfer, its quasi-one-dimensional behaviour, and its two phase transitions involving dimerization and tetramerization of the TCNQ molecules along the stacking axis.

The MEM molecule is shown in Fig 2. It is a very good electron donor and hence is assumed to donate a full electron per MEM molecule to the TCNQ stack. The crystal structure consists, generally, of stacks of TCNQ molecules with MEM molecules separating planes containing the stacks.(Bosch and van Bodegom,1977). See Fig. 3 for the crystal structure at 93K.

There are two known phase transitions in $MEM(TCNQ)_2$. Below 19K, the TCNQ molecules are tetramerized along the stacking axis with one electron pair per tetramer. This is thought to be an example of a Spin Peierls transition which opens a gap at the Fermi wavevector. The ground state is then non-magnetic with elementary excitations which are spin-wave excitations. (Huizinga et al., 1979). Between 20K and 340K, X-ray results indicate that the TCNQ molecules form dimers with the intra-

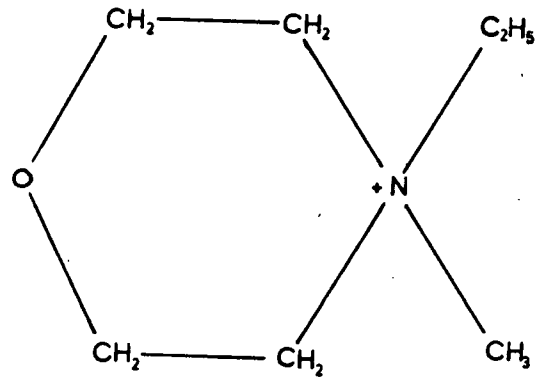

Figure 2. The organic donor molecule MEM.

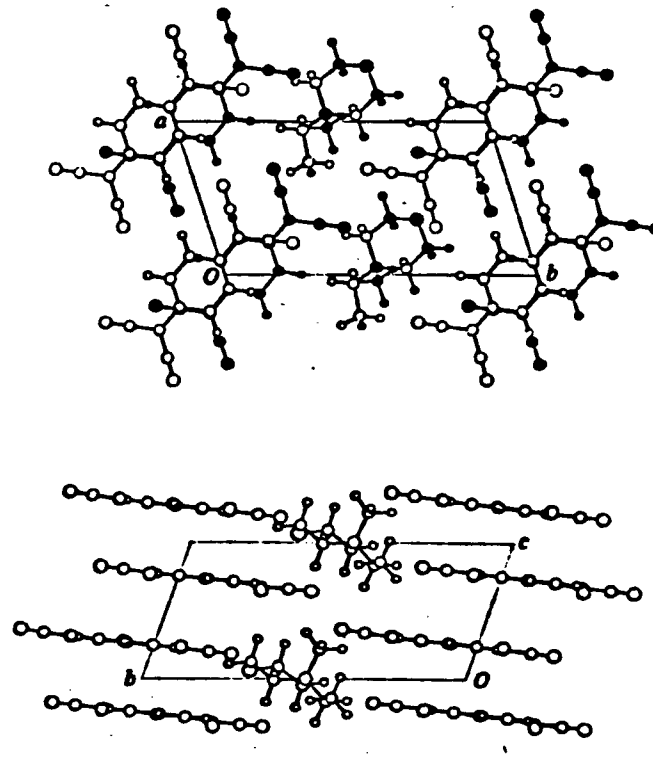

Figure 3. The crystal structure of MEM(TCNQ)$_2$ at 93 K. From Bosch and van Bodegom (1977)

dimer and inter-dimer overlaps being easily distinguishable. Fig. 4a shows the intra-dimer overlap of two TCNQ molecules and Fig. 4b shows the inter-dimer overlap. Fig. 5 shows the variation in the TCNQ-TCNQ separation perpendicular to the plane of the molecules. Here a=3.15A and b=3.27A.

In this phase, the crystal is a semiconductor with a gap of about 0.8 eV. (Morrow et al., 1979). It has been reported (Chaikin, 1979) that the thermopower is about -60 μV/K. Although the low temperature values vary, this value for the thermopower seems to be common among the 1:2 TCNQ salts including Quinolinium $(TCNQ)_2$ and Triethylammonium $(TCNQ)_2$. (Conwell,1978 and references therein). Much work has been done on trying to understand this value of the thermopower by using a one-dimensional Hubbard model to describe the TCNQ stacks. It is generally agreed that a value of -60 μV/K implies that, for a Hubbard model, the on-site repulsion U, which is the interaction for two electrons on a single TCNQ molecule, must be greater than kT.(Conwell,1978; Kwak and Beni,1976; Chaikin and Beni,1976). The use of the Hubbard model to describe TCNQ stacks will be discussed below.

At 340 K there is a violent first order transition to a phase in which the distinction between intra-dimer and inter-dimer overlap almost disappears. Fig. 6 shows these overlaps in the undimerized phase. In this phase the conductivity is between 15 and 30 $(\Omega\text{-cm})^{-1}$ and does not show an exponential

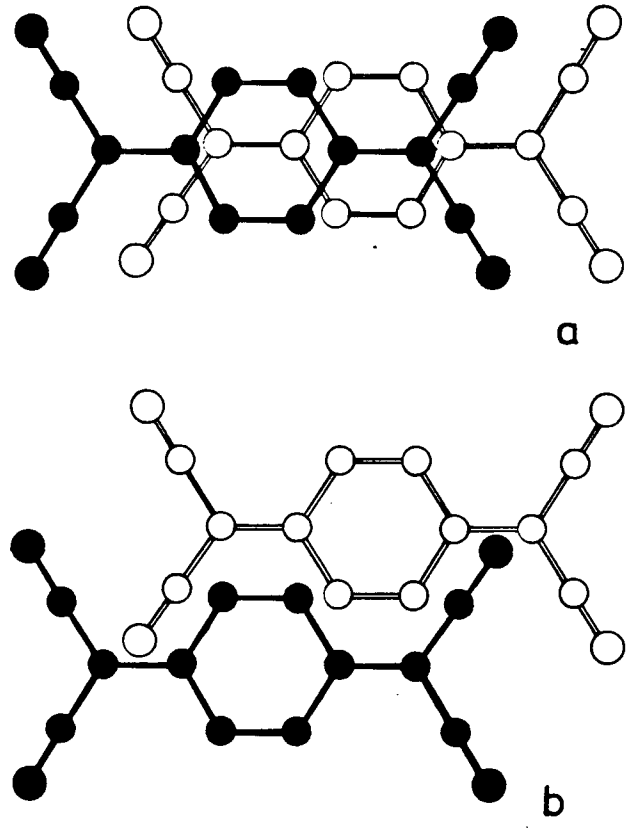

Figure 4a. The intra-dimer TCNQ-TCNQ overlap in the dimerized phase of MEM(TCNQ)$_2$.
Figure 4b. The inter-dimer overlap in the dimerized phase of MEM(TCNQ)$_2$.

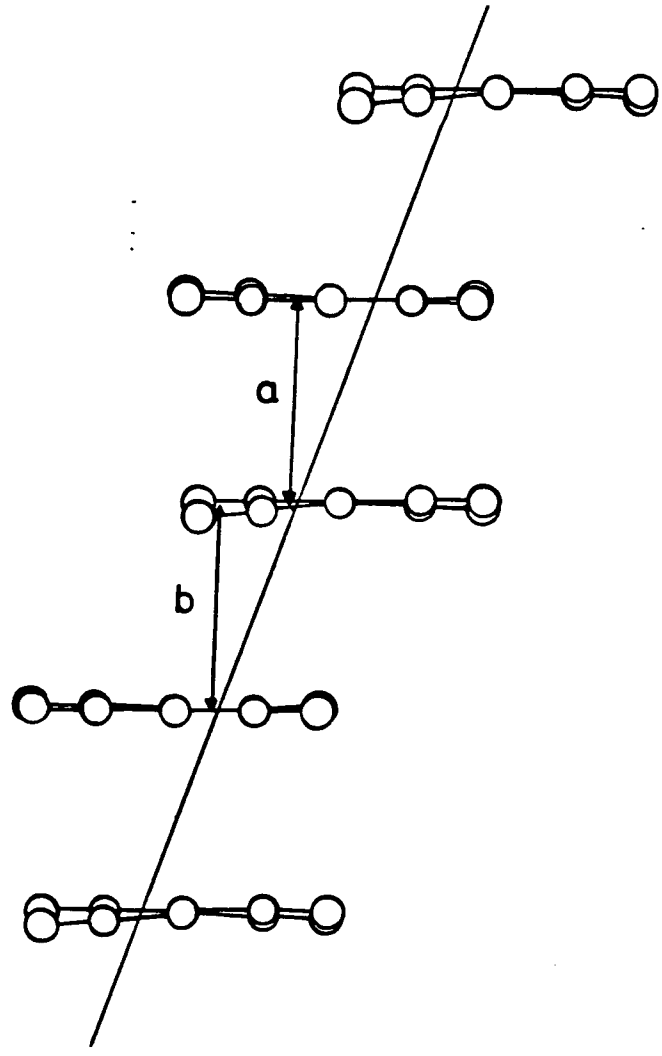

Figure 5. The TCNQ-TCNQ spacing perpendicular to the TCNQ planes in the dimerized phase of $MEM(TCNQ)_2$.

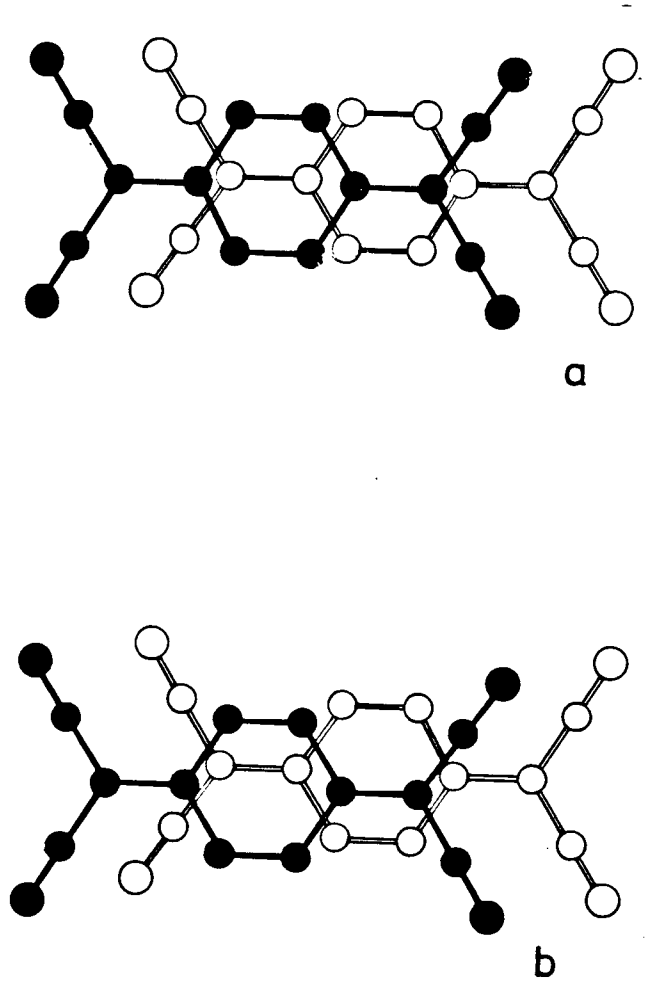

Figure 6. The two types of TCNQ-TCNQ overlap in the undimerized phase of $MEM(TCNQ)_2$.

temperature dependence. As stated above, the MEM molecule should lose one electron to the TCNQ chain. Defining ρ as N/N_o, where N is the number of electrons transferred and N_o is the number of TCNQ sites, this corresponds to $\rho=1/2$. Such a band filling would be expected to exhibit metallic conduction. The conduction in the high temperature phase, while still low, has a temperature dependence more like that of a metal than a semiconductor.

1.2b Use of the Hubbard Model to Describe TCNQ Stacks

Many workers have found it necessary to include the effects of Coulomb interactions and overlap in describing the properties of TCNQ stacks in various TCNQ charge transfer salts. These include the scattering of diffuse X-rays from TTF TCNQ at $q=4k_F^o$ (Torrance,1978) and the thermopowers of the 1:2 salts. These effects are usually included by treating the stacks using the Hubbard model or extensions of the Hubbard model to include the interaction between electrons on neighbouring TCNQ molecules. This model provides the simplest way to deal with correlations brought about by Coulomb repulsion and by overlap of adjacent sites. It is clear that these correlations can be a source of periodicity quite distinct from that associated with the usual Peierls distortion of wavevector $2k_F^o$.

Hubbard was interested in describing correlation effects in narrow d-electron bands of transition metals. For a narrow band, the Wannier functions, obtained by summing the Bloch functions over the Brillouin zone, were well localized on the lattice sites. This allowed him to neglect all Coulomb interactions except for on-site repulsion. This Hamiltonian then had the form,(Hubbard,1963),

$$H=-t\sum_i (c^+_{i,\sigma} c_{i+1,\sigma} + c^+_{i+1,\sigma} c_{i,\sigma}) + (U/2)\sum_{i\sigma} n_{i\sigma} n_{i,-\sigma} \qquad (1.3)$$

Here t is the overlap or hopping integral between adjacent

sites, $c_{i\sigma}^{+}$ and $c_{i\sigma}$ are creation and annihilation operators for an electron of spin σ on site i, and U is the Coulomb interaction for 2 electrons on the same site. The extended Hubbard Hamiltonian includes terms in V_i for the interaction of electrons separated by i lattice spacings (Hubbard,1978).

We will not be concerned with the general model for all values of U. Rather, we will look at the effects of having a very large U. Following Torrance(1977) we note that as U goes to infinity, the problem transforms exactly to the case for spinless fermions. This is because for very large U, double occupancy of a TCNQ molecule is not allowed and this is the situation for spinless fermions as well. This does not change the tight binding problem except that each state can now accomodate only one electron. The dispersion relation for the lowest band is then identical to that for the U=0 tight binding problem,

$$E(k) = -2t \cos(kb)$$

where b is the lattice constant. Now, however, for N_o lattice sites, the lower band contains only N_o states within the Brillouin zone instead of $2N_o$ states as for U = 0. As a result, the value of the wave vector for the highest filled level in the ground state is doubled to $k_F = \pi N/(bN_o)$ rather than $k_F^o = \pi N/(2bN_o)$ where k_F^o is the Fermi wavevector for U = 0. There is now a gap of U - 4t (Ovchinnikov,1970) above which double occupancy of TCNQ sites occurs.

With regard to this point, there is a misleading figure which appears in at least two references.(Chaikin et al., 1973; Epstein et al., 1972). It shows a gap of U - 4t with the minimum of the lower band and maximum of the upper band separated by U. This implies a band width of 2t in the upper and lower band and this is clearly in conflict with the result for the spinless fermion case. That U should, in fact, be the separation between the centres of the bands is suggested by two simple-minded arguments. The first is that, for t=0, we expect 2 levels separated by U. As we turn on the overlap, these levels will spread into bands just as a single level would and there will clearly be states separated by more than U. This is consistent with the result obtained by using the Hubbard model to describe the hydrogen molecule.(Ashcroft and Mermin, 1976). For this case the two electron levels are given by

(1.4) $$E = (1/2)U \pm \sqrt{4t^2+U^2/4} \quad .$$

For U>>4t the splitting is just U. As t is increased, the separation increases to something greater than U. This suggests some inconsistency in a Hubbard model calculation in which, for U>>4t, the maximum separation of any two levels is U.

We will now qualitatively consider the effect on a chain, described by the extended Hubbard model, of the dominance of specific terms in the Hamiltonian. We focus attention on the lower band. For large U there are N_o states in the Brillouin

zone. For $\rho<1$, the wavevector for the highest filled level in the ground state is less than π/b and we have a partially filled band which can behave like a one-dimensional metal. This filling of the band out to $k=\pm 2k_F^o$ will have a number of possible consequences. The electron-hole excitations might have zero energy at $q = 4k_F^o$.(Coll, 1974). Alternatively a gap might be opened in the band by a lattice distortion of wavevector $4k_F^o$. One way in which this might occur would be a Peierl's distortion arising because of the softening of the $4k_F^o$ phonon (Kohn anomaly). A gap might also arise because of a Wigner crystallization. For this simple model in which U is the only Coulomb interaction, Wigner crystallization can only come about for $\rho=1$.

If longer range Coulomb interactions are included, Wigner crystallization can result for $\rho<1$. Torrance attributes the $4k_F^o$ diffuse X-ray scattering from TTF TCNQ to such a crystallization.(Torrance, 1978, 1977; Torrance and Silverman, 1977; Klimenko et al., 1976). The simplest model dealing with this situation is then the Extended Hubbard model (Hubbard, 1978) for which the nearest neighbour Coulomb interaction, V_1, is included. For large V_1, Hubbard finds that for $\rho=1/n$ the electrons are separated by n spacings. For $1/(n+1)<\rho<1/n$,the electrons will be separated by n or n+1 spaces in some kind of periodic manner. This non-uniform spacing of electrons might be expected to lead to distortion in the lattice due to Coulomb

interactions with the lattice.

For the case of ρ=1/2, the large U and V_1 case would lead to electrons on every second site. This would not distort the lattice but the periodicity of the electrons would open a gap in the electronic spectrum. This can be seen easily because of the fact that, for the Wigner crystal ground state, any excitation will put two electrons on nearest neighbour sites and this state will be raised by V_1. If V_1 is larger than the bandwidth, a gap is formed. We cannot, however, immediately apply a large V_1 model to $MEM(TCNQ)_2$ without caution since Conwell (1978) notes that the results of Chaikin and Beni (1976) indicate that a thermopower of $-60\mu V/K$ is inconsistent with $V_1 >> kT$ for the Hubbard model.

We come, finally, to consider the role that overlap plays in determining the behaviour of a Hubbard chain. The size of the overlap will have no effect on the stability of a chain unless we allow the chain to distort in such a way that the increased overlap between some of the sites offsets the increased energy of the distorted lattice. If we consider the specific case of $MEM(TCNQ)_2$, with ρ=1/2, we find that in the presence of a small distortion which distinguishes between two overlaps, t_1 and t_2, the intra-dimer and inter-dimer overlaps respectively, the bandwidth changes from 4t to $2(t_1 + t_2)$ and a gap of $2|t_1 - t_2|$ opens in the middle. For a half filled band, such as for large U and ρ=1/2, this might be an important

mechanism for driving the system to dimerization. The tight-binding problem for a chain with alternating overlaps and separations is discussed in Appendix A.

1.2c Purpose of the Cavity Perturbation Measurements on $MEM(TCNQ)_2$

This part of the experiment was carried out to measure the electrical properties above and below the dimerization transition and, in particular, to confirm the d.c. measurements. The d.c. results were, in some sense, suspect due to the violent cracking experienced by the crystal on being heated through the transition. It was felt that the contactless microwave methods, for which the cracks would be capacitatively shorted, would circumvent some of the problems associated with the uncertainty in the current paths in a cracked anisotropic crystal.

Some of the preceeding discussion on the role of different interactions in determining the properties of a material described by the Hubbard model will be applied to $MEM(TCNQ)_2$ in Chapter III. There we will find that while the conductivity and dielectric constant do not help us to identify the valid regime in terms of relative magnitudes of interactions, they do confirm the d.c. results which, in turn, allow us to use the measured value for the gap to estimate some of the interactions for different assumptions about relative magnitudes of interactions.

1.3 TTF-TCNQ and the Pinned Charge Density Wave

1.3a TTF-TCNQ

There has been much written about the properties and structure of TTF TCNQ . A brief summary of some of the relevant points will be presented here.

This material, like most TCNQ charge transfer salts, involves stacks of TCNQ molecules. Unlike some donors, however, TTF is also planar and stacks as well. The TTF molecule is shown in Fig. 7. The crystal structure is shown in Fig. 8. The slipped geometry of the TCNQ molecules is found to maximize the overlap of the π orbitals on neighbouring molecules. (Berlinsky et al.,1974). The structure suggests highly anistotropic behaviour and this is confirmed by conductivity measurements (Tiedje,1975) and dielectric constant measurements (Khanna et al.,1974).

TTF-TCNQ is one of the most highly conducting of the one-dimensional organic conductors found to date. While the temperature dependence of the conductivity, T^{-2} rather than T^{-1} , is not exactly characteristic of a metal, it does exhibit some of the properties expected for a material with a one-dimensional, partly filled band such as the transition from high to low conductivity and the diffuse scattering of X-rays at $q=2k$. Friend et al. (1978) show that the constant volume temperature dependence, as opposed to the constant pressure results usually quoted, goes as T . The temperature dependence

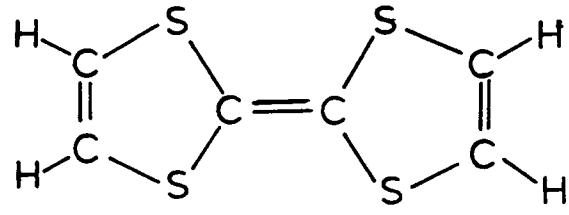

TTF

Figure 7. The organic donor molecule TTF.

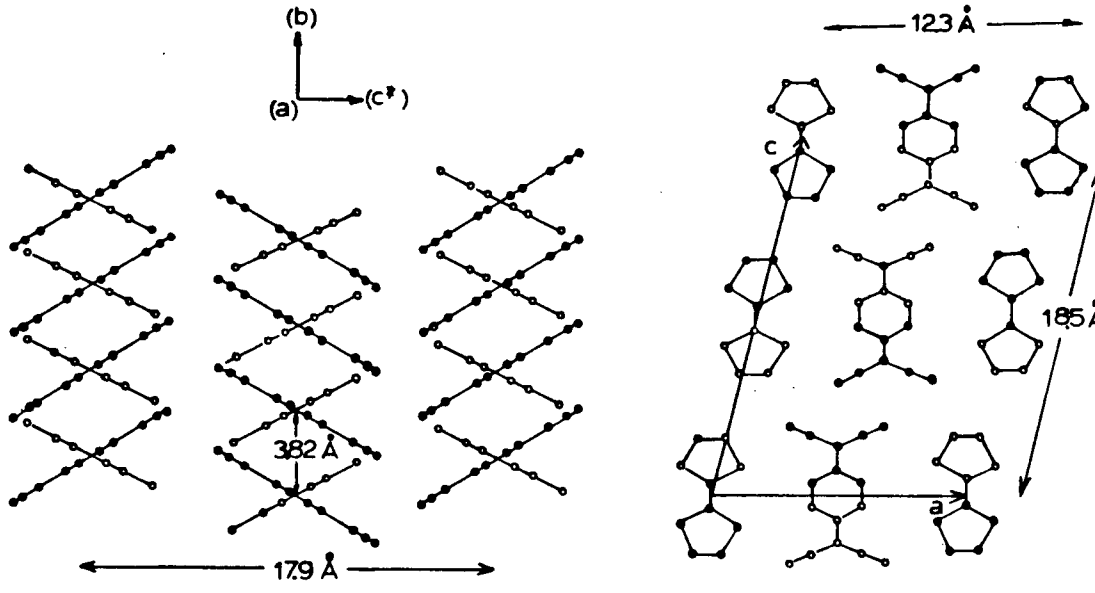

Figure 8. The crystal structure of TTF-TCNQ.

in excess of this is then due to the effect of thermal contraction on the conduction band.

As T approaches 54K, conductivity rises to a maximum. It has been suggested that this is due to a collective mechanism involving charge density waves. (Bardeen,1973; Heegar,1977; Andrieux et al., 1978). For the usual Peierls transition, these would have characteristic wavevector $2k_F^o$. Torrance (1977), however, has argued that on the basis of the $4k_F^o$ diffuse X-ray scattering present at all temperatures, TTF-TCNQ should be considered as a large U system. This leads to a characteristic wavevector, for the charge system, of $4k_F^o$. For antiferromagnetic coupling, the characteristic wavevector for the spin system is still $2k_F^o$. Torrance still, however, accepts the $2k_F^o$ distortion as being dominant at low temperature. The dominant mechanism for the high conductivity above 54K appears to remain unsettled.

Below 54K, the conductivity drops sharply. X-ray and neutron scattering show extra reciprocal lattice points which indicate the presence of a three-dimensional super-lattice. The periodicity of the extra spots in the stacking direction has been interpretted as being $2k_F^o$.(Comes, 1977; Heegar, 1977). The drop in conductivity is believed to indicate the opening of a gap in the electronic spectrum due to the $2k_F^o$ distortion. This distortion is incommensurate with the lattice and should thus, in the absence of pinning, have no preferred phase

relative to the lattice. In the apparent absence of a collective mode contribution to the d.c. conductivity, it is assumed that the charge density wave is pinned to the lattice by impurities or three-dimensional ordering effects.

A pinned collective mode would strongly enhance the low frequency dielectric constant. Such a mechanism has been advanced (Lee, Rice, and Anderson, 1974) to account for the high dielectric constant of about 3000 observed below 40 GHz.

1.3b Dielectric Constant for a Pinned Charge Density Wave

As has been discussed, a charge density wave which was incommensurate with the lattice could be expected to propagate without attenuation. Lee, Rice, and Anderson (1974) point out, however, that both three-dimensional ordering and impurities will pin the charge density waves on different chains to each other and to the crystal lattice. Three-dimensional ordering, they felt, should result in a sharp transtion to a low temperature insulating phase while impurity pinning should give rise to a more gradual transition. The way in which such a pinned mode could contribute to the low frequency dielectric constant is described below.

The distortion opens a gap of width γ_g at the fermi wavevector. Associated with transitions across this gap will be a polarizability and a contribution to the dielectric constant. These are labelled as the single particle contributions, α^{sp} and ϵ^{sp} respectively, to distinguish them from those due to the collective mode itself. With the collective mode we can associate an effective charge, e_ϵ, and a reduced mass, M. The equation of motion for the pinned wave in an a.c. field, $Ee^{i\omega t}$, is then, (Balkanski, 1972)

$$M\ddot{u} + M\Gamma\dot{u} + M\bar{\omega}^2 u = e_\epsilon E e^{i\omega t} \tag{1.5}$$

where Γ is a damping constant and will be the full width at half maximum of the resonance, and u is the coordinate describing the

motion of the charge density wave relative to the lattice. The solution to (1.5) is

$$u=(e_E E/M)\, e^{i\omega t}/(\bar{\omega}^2-\omega^2-i\Gamma\omega) \tag{1.6}$$

The associated dipole moment is then ue_E so that the polarizability is given by

$$\alpha=\alpha^{sp}+(e_E^2/M)/(\bar{\omega}^2-\omega^2-i\Gamma\omega) \tag{1.7}$$

where the single particle contribution has been included.

Ashcroft and Mermin (1976) show how the dielectric constant can be obtained from a polarizability of this form. Their result is obtained using the Clausius-Mossotti relation and is thus restricted to crystals with cubic symmetry in which the Lorentz local field is appropriate. TTF-TCNQ clearly does not present a situation of cubic symmetry. If we are interested in the dielectric constant for a principal axis, however, it will still be true that the macroscopic field, the polarization, and thus the local field are parallel. In light of this, we assume

$$\vec{E}^{local}(r)=K\,\vec{E}(r)$$

where K is some constant depending on $\epsilon(\omega)$. For cubic symmetry, $K=1+(\epsilon-1)/3$. Using the relationships (Ashcroft and Mermin, 1976)

$$\vec{P}(r) = ((\epsilon-1)/4\pi)\vec{E}(r)$$

and

$$\vec{P}(r) = (\alpha/v)\vec{E}^{local}(r)$$

where v is the volume appropriate to α, we get

$$(\epsilon-1)/K = 4\pi\alpha/v\ .$$

Replacing α using Eq. (1.7) gives

$$(1.8) \qquad \frac{\epsilon(\omega)-1}{K(\omega)} = \frac{4\pi}{v}\left(\alpha^{sp} + \frac{e_E^2/M}{\bar{\omega}^2-\omega^2-i\Gamma\omega}\right)$$

Here, $\epsilon(\omega)$ is the complex dielectric constant at frequency ω. eE, M, and v can be eliminated by defining the low frequency dielectric constant, $\epsilon(0)$, and the high frequency value, $\epsilon(\infty)$. $\epsilon(\infty)$ is the dielectric constant for ω much greater than $\bar{\omega}$ but smaller than $2\pi\nu_g$. We thus have

$$(1.9a) \qquad (\epsilon(0)-1)/K(0) = (4\pi/v)(\alpha^{sp}+e_E^2/(M\bar{\omega}^2))$$

$$(1.9b) \qquad (\epsilon(\infty)-1)/K(\infty) = 4\pi\alpha^{sp}/v$$

$\epsilon(\infty)$ correctly depends only on transitions across the gap and we will identify it with ϵ^{sp}.

If we can make the assumption that $K(\omega) = 1+(\epsilon(\omega)-1)/(B+1)$, then it can be shown that

$$(1.10) \qquad \epsilon(\omega) = \epsilon^{sp} + (\epsilon(0)-\epsilon^{sp})\,\omega_o^2/(\omega_o^2-\omega^2-i\Gamma\omega)$$

where $\omega_o^2=(\epsilon(\infty)+B)\,\bar{\omega}^2/(\epsilon(0)+B)$. This is the expression for $\epsilon(\omega)$ as used by Eldridge and Bates (1979). While it is not clear how we can connect ω_o^2 to the microscopic picture of a pinned charge density wave, this model does provide the basis for a phenomenological fit to $\epsilon(\omega)$.

In Eq. (1.10), for ω close to ω_o, the imaginary part of $\epsilon(\omega)$ is a Lorentzian of full width at half maximum given by Γ. ϵ^{sp} is given by Lee, Rice, and Anderson (1974) as

$$\epsilon^{sp}=1+2\nu_p^2/3\nu_g^2$$

This is the dielectric constant at frequencies where the pinned mode cannot respond and only transitions across the gap can contribute.

Eldridge fits his infra-red measurements to this model with $\epsilon^{sp}=1068$, $\epsilon(o)=3600$, the pinning frequency equal to 102 GHz, and $\frac{\Gamma}{2}=1.5\text{GHz}$.

1.3c Purpose of Dielectric Resonance Studies on TTF-TCNQ

The purpose of this series of experiments was to extend Barry's (1977) dielectric resonance measurements on TTF-TCNQ at low temperatures in an attempt to clarify the frequency dependence of the real and imaginary parts of the dielectric constant.

These are of particular interest in that the low frequency dielectric constant is important in fitting the infra-red bolometric measurements of Eldridge and Bates (1979) to equation(1.10) for the pinned mode dielectric constant. It is also interesting to consider the frequency dependence of the dielectric constant in light of this model. Unfortunately, the frequency range conveniently available is too small to give any conclusive indication of the validity of the model.

There have been two previous measurements of the dielectric constant parallel to the stacking axis, ϵ_b' . Khanna et al. (1974) obtained $\epsilon_b'=(3.2\pm0.6)\times10^3$ using cavity perturbation at 10.4 GHz. They also claimed to have measured a crystal with the long direction along the a axis and obtained $\epsilon_a'=6\pm2$. Barry (1977) attempted to measure ϵ_b' at higher frequencies using the dielectric resonator technique and obtained similar values. The same measurements, however, gave a value for ϵ_a' of about 2. This seemed too small for such a material. In addition to this, the shape of the mode plots, showing the resonant frequency squared

versus the inverse square length of the crystal, were not fully understood. One mode was identified as coaxial and thus expected to have a slope corresponding to propagation along the b axis at about the speed of light. The dielectric modes were expected to give a slope proportional to $1/\epsilon'_a$. In fact all modes gave straight lines with a slope intermediate between the two expected extremes. This was attributed to end effects but the lack of understanding of the slope did cast some doubts on the reliability of the extrapolation to the ordinate axis which was used to allow analysis in the infinite length limit.

The present work was carried out in the hope of extending the measurements to situations in which some of the paradoxes might be resolved.

CHAPTER II

The Measurement of Electrical Properties of $MEM(TCNQ)_2$ Above Room Temperature

2.1 Cavity Perturbation

The electrical properties of small crystals can be studied using cavity perturbation methods similar to those which have been described by a number of authors (Buravov and Schegolev,1971; Khanna et al. ,1975; Waldron, 1969). In this technique, the shift and change in width, due to insertion of a small solid sample, of the resonance of a cavity of known characteristics can be related to the real and imaginary parts of the dielectric constant of the sample if the fields in the sample are known.

The general formula for cavity perturbation is derived in Waldron: (M.K.S. units)

$$\frac{\delta f}{f} = \frac{\iiint_{V_0} \{(\bar{E}_1 \cdot \bar{D}_0 - \bar{E}_0 \cdot \bar{D}_1) - (\bar{H}_1 \cdot \bar{B}_0 - \bar{H}_0 \cdot \bar{B}_1)\}\, dV}{\iiint_{V_0} (\bar{E}_0 \cdot \bar{D}_0 - \bar{H}_0 \cdot \bar{B}_0)\, dV} \tag{2.1}$$

Here, $\bar{E}_0$ and $\bar{H}_0$ are the unperturbed electric and magnetic fields and $\bar{D}_0$ and $\bar{B}_0$ are the unperturbed electric and magnetic displacements. $\delta f/f$ is the fractional shift in the resonant frequency of the cavity due to the perturbation. The subscript 1 labels fields which are the difference between the fields with the sample present and the unperturbed fields. The integral is over the volume of the cavity. This equation neglects the

difference between $\bar{D}_o$ and $\bar{B}_o$ and the total $\bar{D}$ and $\bar{B}$, respectively, in the integral in the denominator. It is thus correct only for small perturbations.

The experiments were carried out with the needle-shaped crystals oriented parrallel to and at the maximum of the E field of the TM_{o1o} mode in the cylindrical cavity. For this mode

$$E_z = E_{oz} J_o(kr) e^{i\omega t}$$

$$H_\phi = -(j\omega/k) E_{oz} J_1(kr) e^{i\omega t} \qquad (2.2)$$

$$E_r = E_\phi = H_r = H_z = 0$$

where E_{oz} is the amplitude of E_z and, for a cavity of radius a,

$$k^2 a^2 = \chi_1^2$$

with χ_1 being the first zero of $J_o(\chi)$.

The denominator of Eq. (2.1) is then easily evaluated to give

$$\iiint_{V_o} (\bar{E}_o \cdot \bar{D}_o - \bar{H}_o \cdot \bar{B}_o)\, dV = 2V_o J_1^2(ka) E_{oz}^2 \qquad (2.3)$$

Using the fact that $\bar{H}=0$ along the cavity axis and that the fields with subscript 1 are assumed negligible outside of the sample, we can write Eq. (2.1) as

$$\frac{\delta f}{f} \approx \frac{\iiint_{V_1} (\bar{E}_1 \cdot \bar{D}_o - \bar{E}_o \cdot \bar{D}_1)\, dV}{2V_o J_1^2(ka) E_{oz}^2} \qquad (2.4)$$

where the integral is now over the volume of the sample. Following Buravov and Schegolev (1971) one can assume that for a sample with a dimension smaller than the skin depth and with depolarizing factor n and dielectric constant ϵ, the field

inside the sample in the presence of external field E_z is given by

(2.5) $$E_i = E_z/(1+n(\epsilon-1)).$$

n" is defined for a general ellipsoid of semi-major axis a" and semi-minor axes b" and c" as (Osborne, 1945)

(2.6) $$n=(b"c"/a"^2)(\ln(4a"/(b"+c"))-1),$$

We then have

(2.7a) $$E_1 =-E_z\, n(\epsilon-1)/(1+n(\epsilon-1))$$

(2.7b) $$D_1 =E_z((\epsilon-1)-n(\epsilon-1))/(1+n(\epsilon-1))$$

Taking E_z to be continuous across the sample and equal to the maximum value, E_{oz}, allows us to dispose of the integral giving

$$\delta f/f=-V_1(\epsilon-1)/(2V_o J_1^2(ka)(1+n(\epsilon-1)))$$

Following Waldron, we can include the losses in the sample by replacing ϵ by $\epsilon'-j\epsilon''$ where $\epsilon''=2\sigma/f$ and σ is the conductivity in sec.$^{-1}$. $\delta f/f$ is then replaced by $(\Delta f_o + j\Delta_o/2)$ where $\Delta f_o=\delta f/f$ and $\Delta_o/2$ is the change, due to the perturbation, in the full width at half maximum of the resonance, divided by the unperturbed frequency. $\Delta_o/2$ is given by $(1/Q_o-1/Q)/2$. Buravov and Schegolev define

(2.9) $$\propto =V_1 E_{oz}^2/2\int_{V_o}|E_z|^2\,dV$$

which, for our mode, becomes

$$V_1/2V_o J_1^2(ka) = 1.855V_1/V_o$$

so that we arrive at their formulae:

$$\Delta f_o = -\alpha \left[\frac{(\epsilon'-1)(1+n(\epsilon'-1)) + n\epsilon''^2}{(1+n(\epsilon'-1))^2 + n^2\epsilon''^2} \right] \tag{2.10}$$

and

$$\frac{\Delta_o}{2} = \frac{\alpha \epsilon''}{(1+n(\epsilon'-1))^2 + n^2\epsilon''^2} \tag{2.11}$$

These may then be inverted to give:

$$\epsilon'-1 = \frac{1}{n} \left[\frac{\Delta f_o \left(\frac{\alpha}{n} - \Delta f_o\right) - \left(\frac{\Delta_o}{2}\right)^2}{\left(\frac{\Delta_o}{2}\right)^2 + \left(\frac{\alpha}{n} - \Delta f_o\right)^2} \right] \tag{2.12}$$

and

$$\epsilon'' = \frac{2\sigma}{f} = \frac{\alpha}{n^2} \left[\frac{\frac{\Delta_o}{2}}{\left(\frac{\Delta_o}{2}\right)^2 + \left(\frac{\alpha}{n} - \Delta f_o\right)^2} \right] \tag{2.13}$$

These formulae will, in general, be applicable only for small conductivities and thin crystals for which the skin depth is large compared to the smallest dimension. The skin depth is given by

$$\delta_s = c_L / (2\pi\sigma\omega)^{\frac{1}{2}}$$

where c_L is the speed of light, σ is the conductivity in $sec.^{-1}$, and ω is the frequency in radians/sec. (1 $sec.^{-1}$ = $9X10^{11}$ $(\Omega\,cm)^{-1}$).

In the high conductivity regime, only the real part of the conductivity can be determined. If the minimum sample dimension perpendicular to the field is much larger than the skin depth,

as was the case for some of the crystals studied, one must use the expression of Cohen et al. (1975) for a prolate spheroid,

$$\sigma^{\frac{1}{2}} = \frac{9\pi^2}{2^5} \cdot \frac{(\Delta f_o)^2}{\alpha} \cdot \frac{f^{3/2} r}{C_L} \cdot \frac{1}{\Delta_o} \qquad (2.15)$$

where f is the operating frequency and r is the semi-minor axis. The derivation of this expression contains the assumption that $\Delta f_o \approx \alpha/n$ in the skin depth limited regime. α is proportional to the spheroid volume and enters the expression in a way which suggests that one may extend the formula to the case of a general ellipsoid by using Eq. (2.15) for a prolate spheroid of the same volume. In terms of the ellipsoid semi-axes, a">b">c", the expression becomes

$$\sigma^{\frac{1}{2}} = \frac{9\pi^2}{2^5} \cdot \frac{(\Delta f_o)^2}{\alpha} \cdot \frac{f^{3/2}\sqrt{b''c''}}{C_L} \cdot \frac{1}{\Delta_o} \qquad (2.16)$$

The question then arises as to what general ellipsoid should be used to approximate a rectangular crystal of length, width, and thickness, a>b$\gtrsim$c. The appearance, in α , of the sample volume, and, in n, of the ratio of the dimensions, suggests that the appropriate ellipsoid has the same volume and dimensional ratios. In terms of the crystal of length, width, and thickness, a>b$\gtrsim$c, the expression becomes

$$\sigma^{\frac{1}{2}} = \frac{9\pi^2}{2^5} \cdot \frac{(\Delta f_o)^2}{\alpha} \cdot \frac{f_o^{\frac{3}{2}} \left(\frac{3}{4\pi}\right)^{\frac{1}{3}} \sqrt{bc}}{C_L} \cdot \frac{1}{\Delta_o} \tag{2.17}$$

If the skin depth is not much larger than the sample thickness, then the assumption of uniform penetration is appropriate and one can use Eq. (2.13) to find ϵ'' and thus σ. As long as the skin depth is large, this is true even for the regime where one has $n\epsilon'' >> 1$ giving $\Delta f_o \approx \alpha/n$, and in which ϵ' cannot be determined (Cohen et al.,1975). In the regime where the skin depth has become small relative to the minimum sample dimensions, Eq. (2.13) is no longer valid and Eq. (2.17) must be used to calculate σ. A discussion as to which model is valid in particular cases appears in more detail in Chapter III.

2.2 The Apparatus

Measurements on four MEM(TCNQ)$_2$ crystals were carried out in a cylindrical copper cavity using the TM_{010} mode in which the E_z field has an antinode along the cavity axis. In this mode, the resonant frequency is proportional to the diameter of the cavity and independent of the height. (Hidy et al. ,1972). The resonance was studied by observing the transmission of the cavity which resonated empty at about 8.5 GHz. The cavity is shown schematically in Fig. 9.

The cavity was heated by means of a circulating water bath. Heat exchangers were placed on both faces between the cavity body and the incoming and outgoing brass waveguides. A thermocouple was clamped to the cavity body midway between the exchangers. This assembly was then placed in a close fitting styrofoam enclosure with walls of about 5 cm. thickness. Temperature equilibrium was monitored by altering the heat bath temperature and then observing the equilibration of the temperature by following the frequency of the resonance.

The crystal volume and shape were determined from the weight of the crystal, using the known crystallographic density of 1.261 g/cc, (Bosch and van Bodegom, 1977), together with microscopic photography.

Crystals were mounted on the end of a thin quartz fibre using epoxy so that the long axis was parallel to the E fields

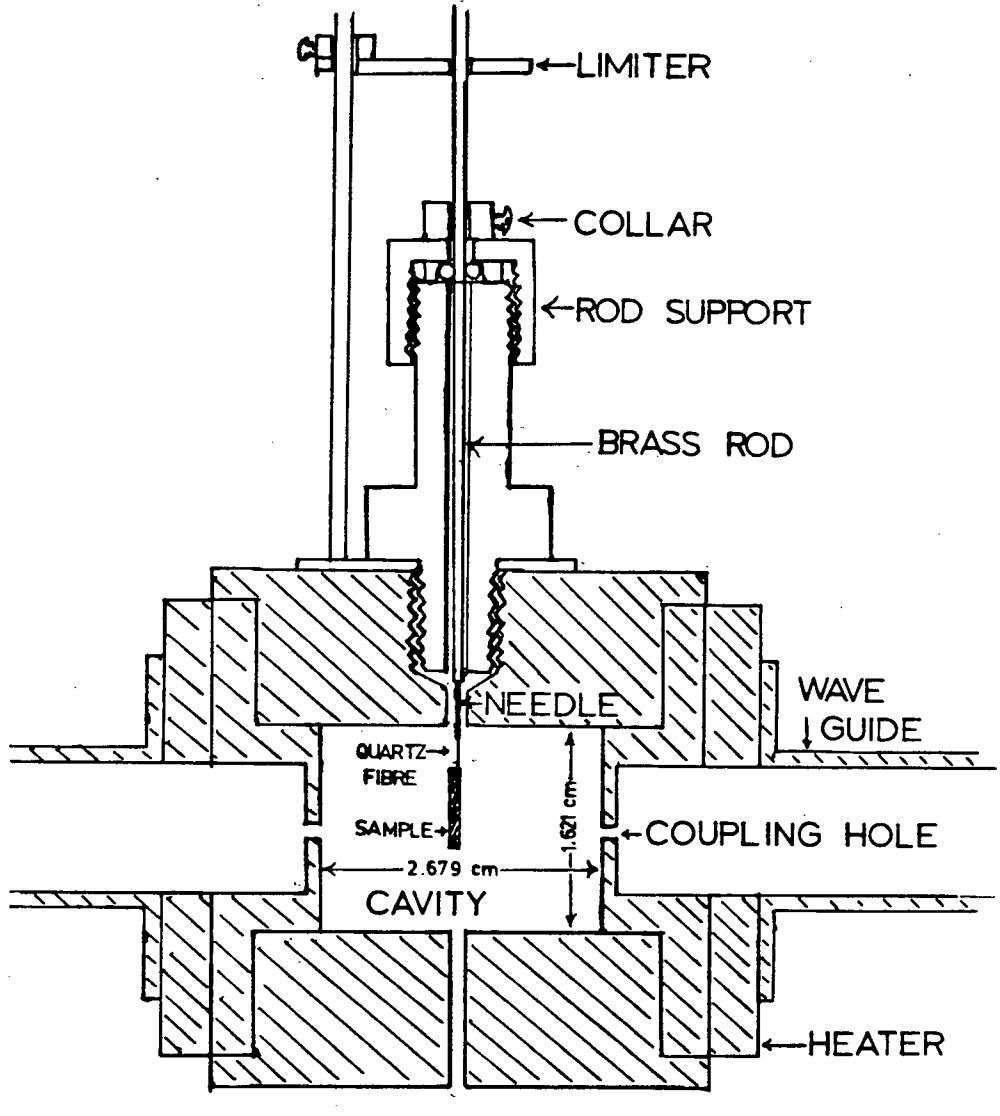

Figure 9. The 8.5 GHz resonant cavity

along the cavity axis. The basic experiment involved measuring the frequency shift and change in width of the cavity passband due to insertion of the crystal. It was thus necessary to use the frequency and width of the resonance, with the quartz fibre inserted, as the unperturbed values. For these measurements , a small drop of epoxy was placed on the end of the fibre so that the small additional amount required to suspend the crystal could be neglected. The frequency and width of the resonance with only the quartz fibre in place, was then measured as a function of temperature to allow for cavity expansion. Resonance data at a given temperature for that fibre was then obtained by interpolation. Sample handling techniques were such that the fibre could be accurately repositioned after mounting of the crystal.

The resonance was observed by frequency modulating the R.F. source at 5 KHz and demodulating the detected signal with a lock-in amplifier. The resulting signal could be used in two ways. It could be integrated and added to the 5KHz modulating signal to give an error signal which locked the R.F. source to the centre frequency of the resonance. This mode of operation was useful for monitoring of the resonance but inconvenient for absolute measurements of the centre frequency due to drift in the integrator. Alternatively, the output of the lock-in could be recorded on an X-Y recorder with the X input being driven, through a D/A converter, directly from a frequency counter

during a slow sweep. The width and centre frequency of the resonance could then be taken directly from the derivative trace. Fig. 10 shows the general arrangement of the apparatus.

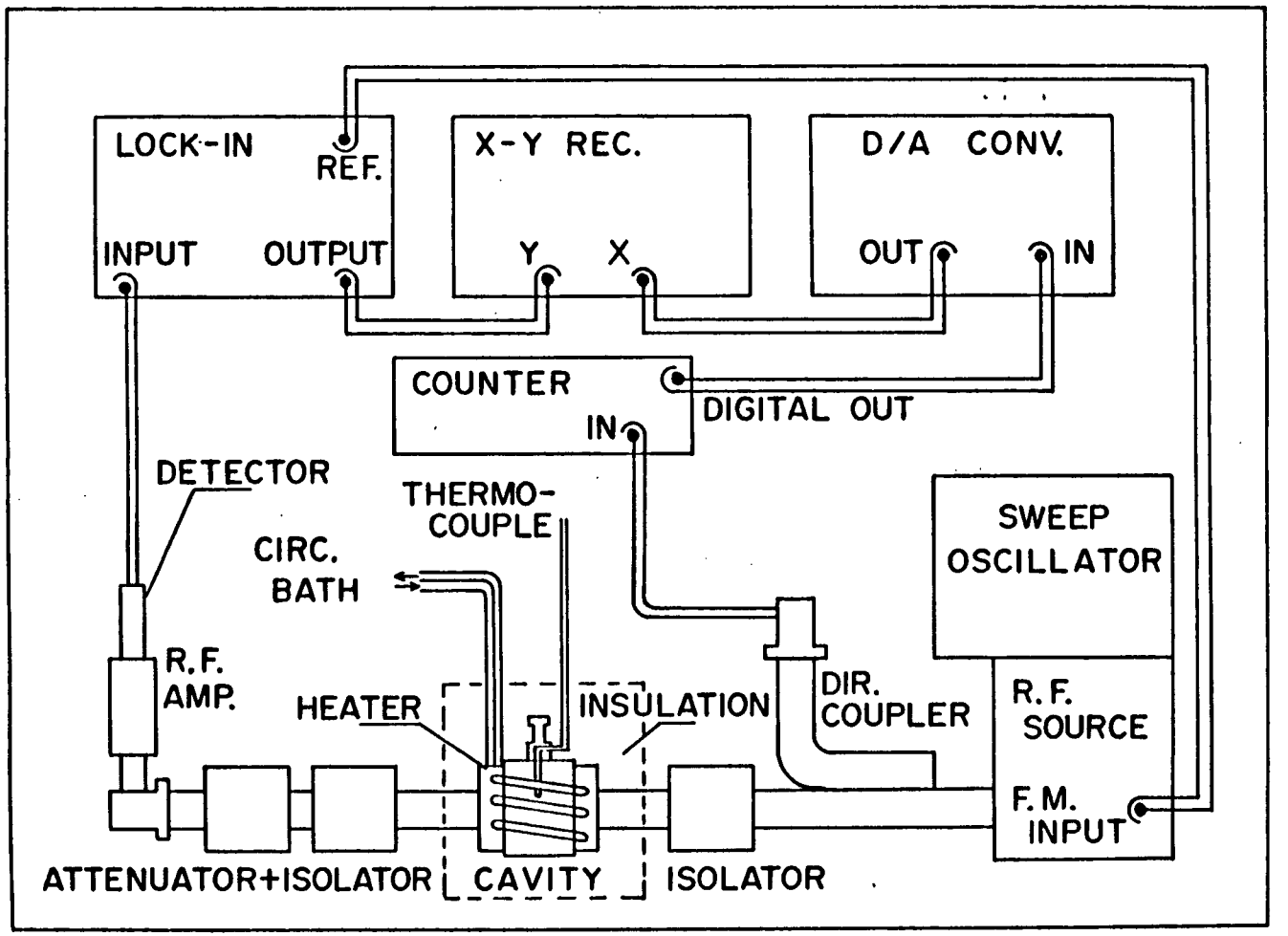

Figure 10. The cavity perturbation apparatus .

2.3 The Measurements

Four $MEM(TCNQ)_2$ crystals were studied in detail using cavity perturbation. The physical properties, including the depolarizing factors and the dimensions are summarized in Table 1.

It has been mentioned that the violence of the first order transition at 60°C provided some incentive for the use of contactless microwave measurements. Fig. 11 shows crystal 2 before and after having passed through the 60°C transition. The crystal has been broken off of the quartz fibre and thus appears shorter in B. The real effect of the transition is the appearance of flaking on the face which is being viewed obliquely. The crystal also appears slightly bent. The damage to the crystal will affect only the depolarizing factor since it is the only shape dependent parameter in the analysis. This effect has, however, been assumed negligible in comparison to the uncertainty in the depolarizing factors used to describe rectangular samples. It has been assumed that the depolarizing fields due to polarization charges at the surface of the cracks are not a serious problem. This assumption is valid if ϵ is not too large and the gap is small so that the capacitance of the crack is large relative to that of the whole crystal.

In spite of the damage, it was found that the crystal could be returned through the transition and that the low temperature

TABLE 1

Physical Data for $MEM(TCNQ)_2$ crystals used

Crystal	1	2	3	4
Source	U.B.C.	U.B.C.	U.B.C.	Groningen
Length a (cm)	0.259	0.519	0.465	0.690
Width b (cm)	0.028	0.038	0.037	0.062
Thickness c (cm)	0.0185	0.032	0.037	0.0267
$n=\frac{bc}{a^2}\left[\ln\left(\frac{4a}{b+c}\right)-1\right]$	0.0162	0.0108	0.0141	0.00843

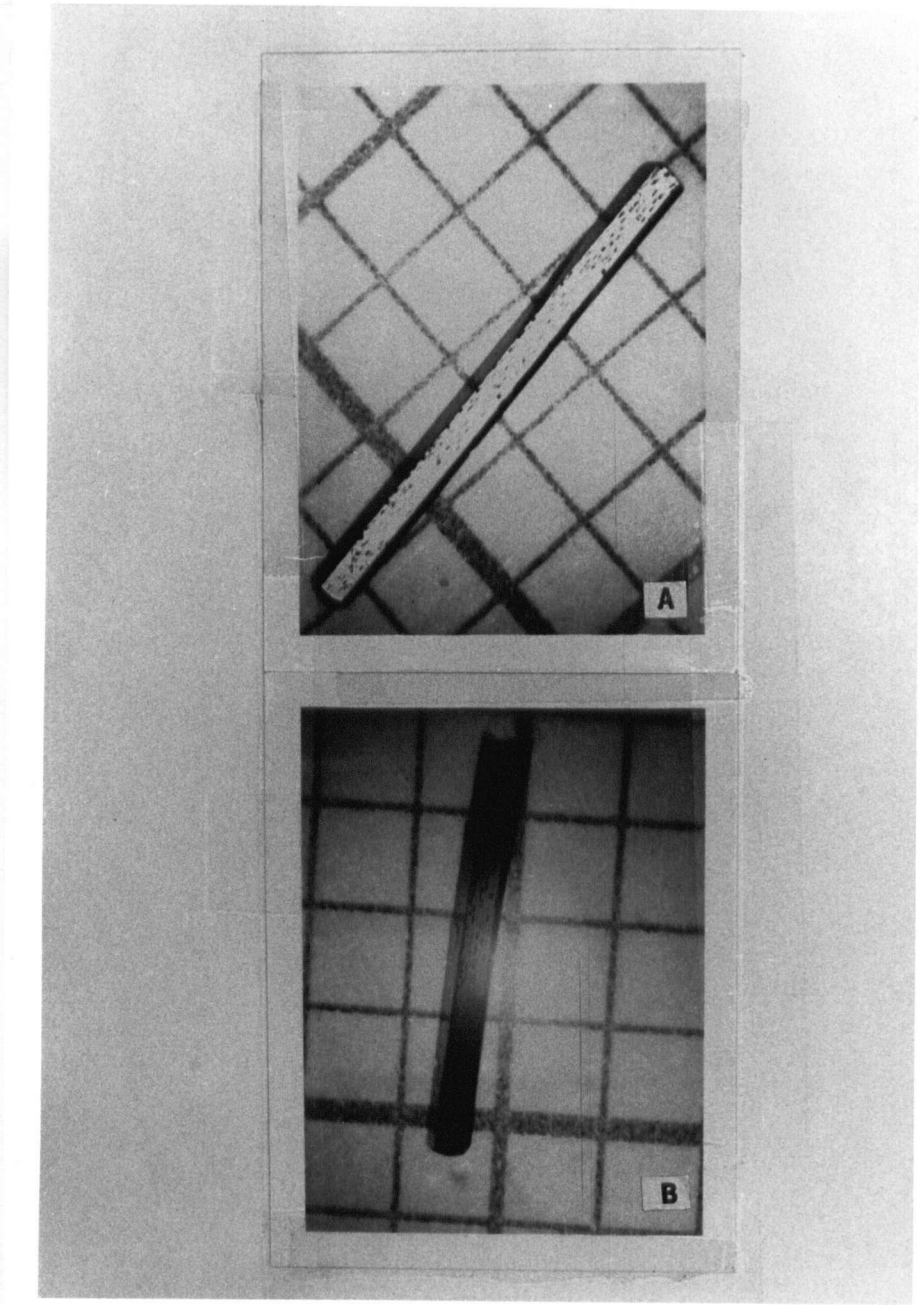

Figure 11. Photograph of MEM(TCNQ)$_2$ crystal before (A) and after (B) having passed through the transition.

frequency shift and width were reproduced. There was, however, considerable hysteresis in the transition, occurring typically, on heating, at about 65°C and, on cooling, at 60°C. This behaviour has also been observed in d.c. and similar a.c. measurements (Morrow et al. 1979). The hysteresis does not depend on the time taken to equilibrate the crystal at temperatures close to the transition temperature. It was found that the hysteresis was still present when the crystal was cycled through the transition for a second time. Graphs of the frequency and width of the perturbed resonance as a function of temperature, with crystal 4 inserted, appear in Fig. 12 and Fig. 13. This shows clearly the hysteresis in the transition temperature and the reproducibility of the low temperature properties after the transition. The downward and upward pointing arrows depict the transition on heating and on cooling respectively. Typical traces with just the quartz fibre and with the fibre and a crystal at about 61°C, on the heating cycle, appear in Fig. 14. The trace shown is the derivative of the power transmitted by the cavity. Each derivative trace was obtained with a 10MHz wide scan.

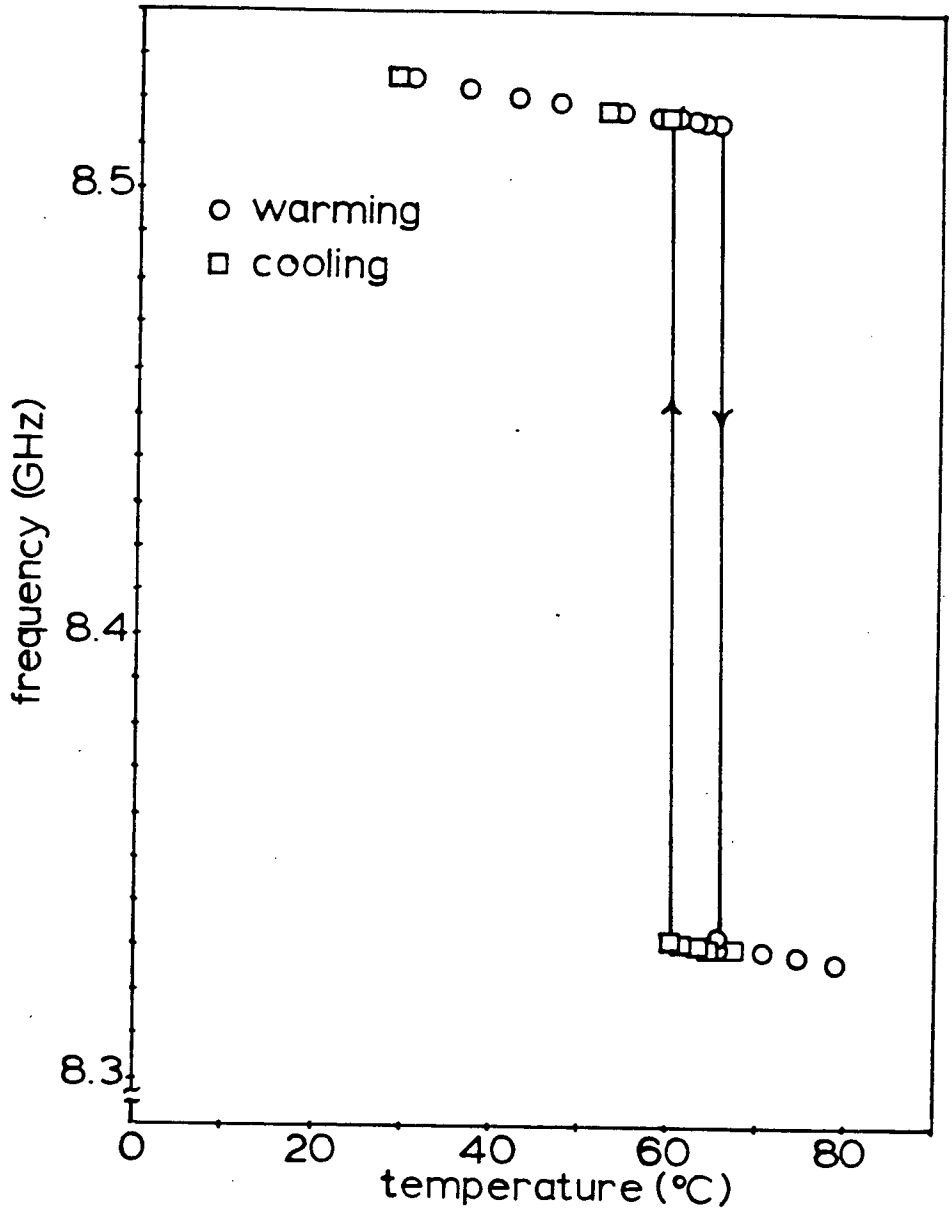

Figure 12. Typical cavity resonant frequency versus temperature with MEM(TCNQ)$_2$ crystal inserted.

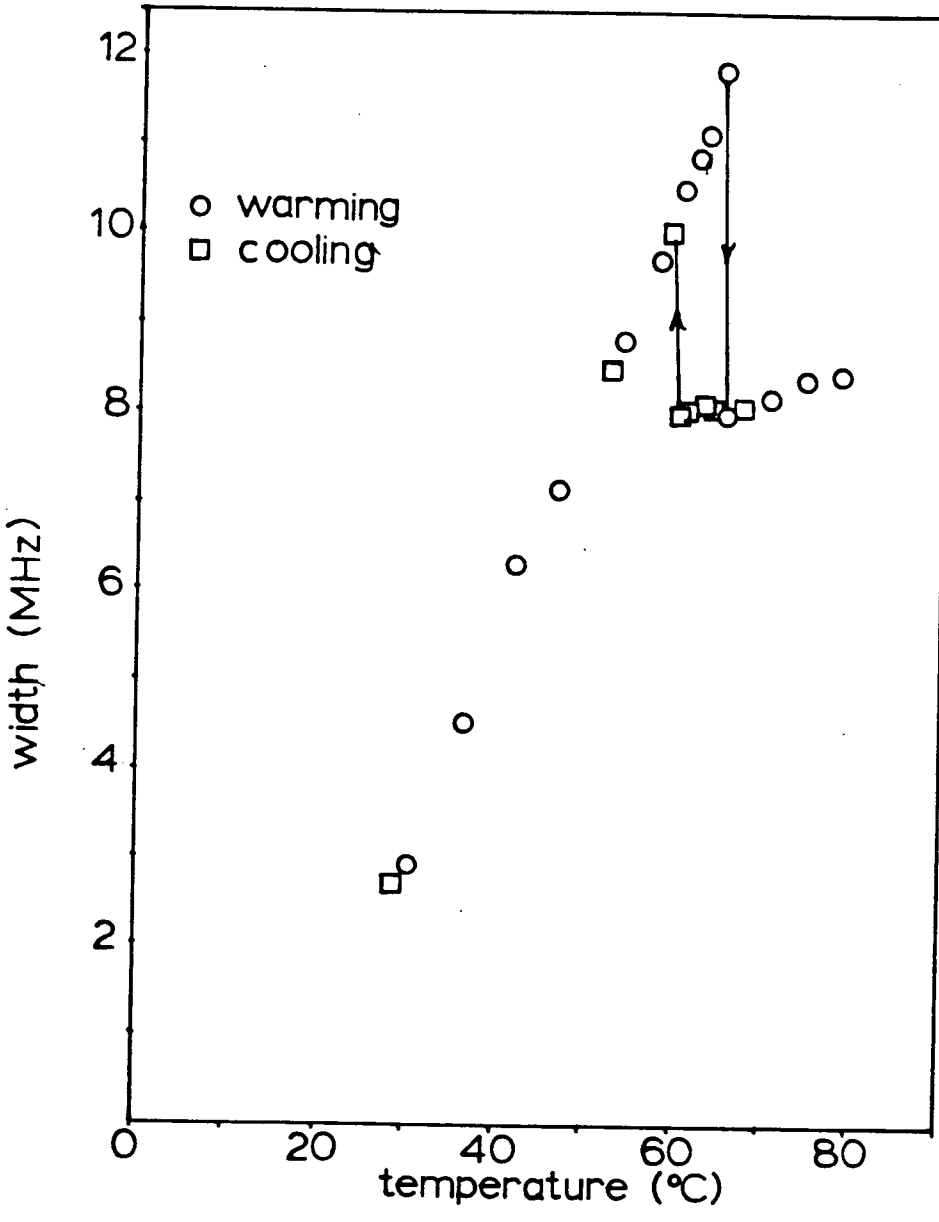

Figure 13. Typical width of cavity resonance versus temperature with MEM(TCNQ)$_2$ crystal inserted .

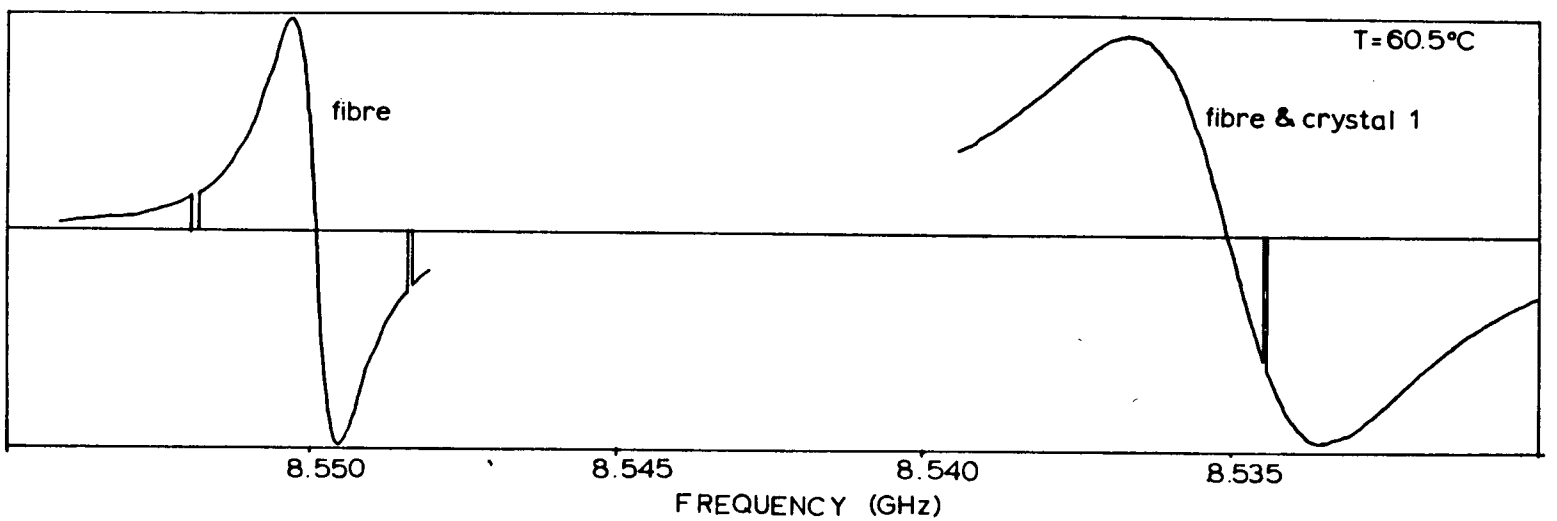

Figure 14. Typical traces of resonance derivative with and without crystal inserted.

CHAPTER III

Results

3.1 Regime of Validity of Perturbation Results

In order to interpret the frequency shift and change in width in terms of the dielectric constants, it is necessary to determine what assumptions can be made about the field penetration in the analysis. The possible situations are that 1) the fields are fully penetrating and $n\epsilon''$ is small so that both ϵ' and ϵ'' can be obtained from eqs. 2.12 and 2.13, 2) that the fields are not skin depth limited but $n\epsilon''$ is large so that only ϵ'' can be obtained and Eq. 2.13 is appropriate or 3) that the fields are skin depth limited and $n\epsilon''$ is large so that only σ or, equivalently, ϵ'' can be obtained from Eq. 2.17.

Eqs. 2.12 and 2.13 can be used to calculate ϵ' and ϵ'' as long as $n\epsilon''$ is small and δ_s is large. We see, in Table 2, that this is the case below the transition. Above the transition, however, the situation is somewhat more complicated. If we compare the measured value of Δf_o to α/n, where n is calculated for a "comparable" elipsoidal sample, the approximate equality suggests that this is the regime in which $n\epsilon''$ is large. In this regime, the observed perturbation is insensitive to ϵ'.

To investigate the effect of non-ellipsoidal shape, two copper pieces, of length 5 and 3 mm, and similar in shape to the $MEM(TCNQ)_2$ crystals, were studied. For these samples, $(\alpha/\Delta f_o)/n$

was found to be 1.033 and 1.027 where n was calculated from Eq. 2.6. These deviations from one are surprisingly small. The somewhat larger discrepances observed in the $MEM(TCNQ)_2$ crystals may be due to the effect of anisotropy on the transverse currents which flow in a non-ellipsoidal sample. These deviations from unity are, at any rate, sufficiently small that we can assume that, above the transition, the crystal is in the regime where the frequency shift is insensitive to ϵ'.

Having determined that $n\epsilon''$ is large above the transition, we are still faced with the decision as to whether σ should be calculated assuming skin depth limited penetration, and thus using Eq. 2.17, or assuming full penetration and thus using Eq. 2.13. Clearly one has to base this decision on whether or not the obtained σ gives a skin depth that is consistent with the size of skin depth assumed in the calculation of σ. We will generally take Eq. 2.17 to be valid for a skin depth smaller than 1/2 of the smallest dimension and use Eq. 2.13 otherwise.

If we analyse the results for crystals 2,3, and 4, assuming a small skin depth, and thus using Eq. 2.17, the values of σ obtained imply a skin depth that is slightly smaller than 1/2 of the smallest dimension. The assumptions implicit in Eq. 2.17 are thus approximately true.

In the analysis of the results for crystal 1, assuming a small skin depth and thus using Eq. 2.17, yields a value for σ

which is an order of magnitude smaller that that found for crystal 4 and hence a skin depth which is comparable to the smallest sample dimension. Since δ_s is larger than half of the thickness, it is thus inappropriate to use the assumption of skin depth limited penetration for Crystal 1.

If, on the other hand, we assume that the skin depth is large for crystal 1, we can use Eq. 2.11 to relate ϵ'' to $\Delta_o/2$. Because we are in the regime where $n\epsilon''$ is large $\Delta_o/2$ becomes independent of $(\epsilon'-1)$ and we can invert Eq. 2.11 directly to get

$$\epsilon'' = \alpha/(n^2(\Delta_o/2)). \tag{3.1}$$

Eq. 3.1 is, in fact, just Eq. 2.13 in which Δf_o has been set equal to α/n. The conductivity obtained for crystal 1 using Eq. 3.1 implies a skin depth which is only slightly smaller than the minimum crystal dimension. This justifies the assumption of penetrating fields made in the use of Eq. 3.1.

The relationship between the two ways of calculating σ in the high conductivity regime is illustrated in Fig. 15a. Assuming, for this regime, that ϵ' is unimportant and setting it arbitrarily to 1, and using the values of f, n, and α appropriate to crystals 1 and 4 just above the transition, we have plotted $\log_{10} \Delta f_o$ and $\log_{10} \Delta_o$ versus $\log_{10} \sigma$ using Eqs. 2.12 and 2.13. Using the same values of f, n, and α plus the value of Δf_o appropriate to each of the two crystals, we have also plotted $\log \Delta_o$ versus $\log \sigma$ using Eq. 2.17. Eq. 2.12 ceases to be useful for the determination of ϵ' in the region

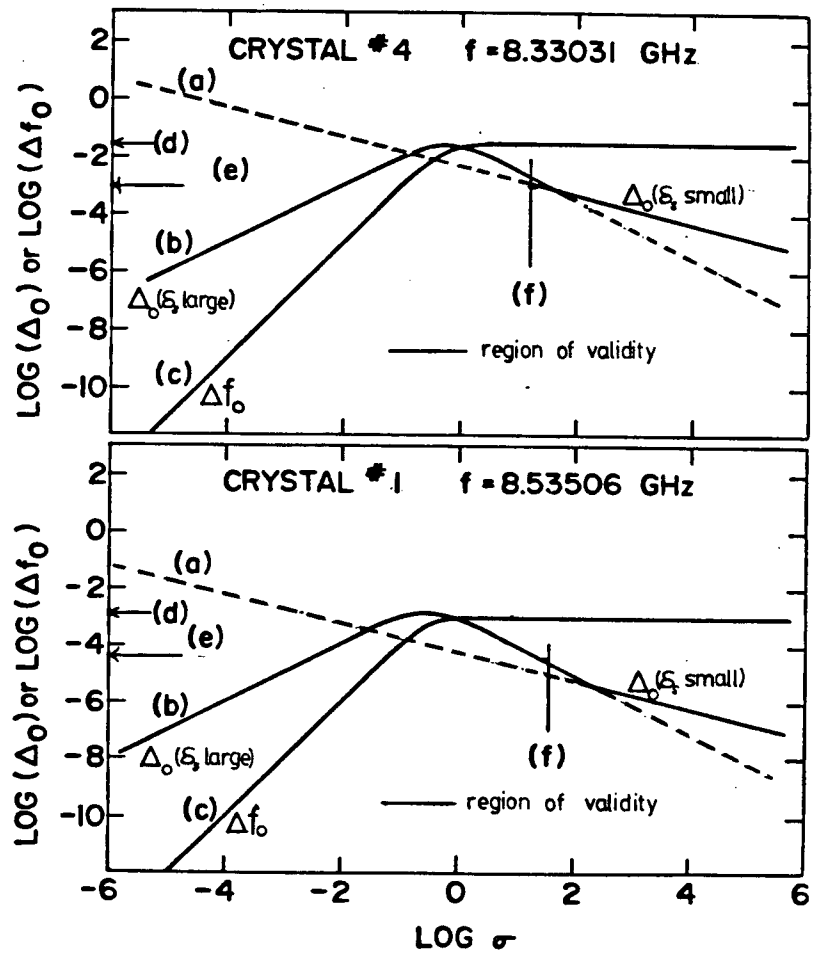

Figure 15. Showing the relation between width and σ using Eqs. 2.10 ,2.13, and 2.17 for experimental conditions as found for $MEM(TCNQ)_2$ crystals 1 and 4.
a) $\log_{10}(\Delta_o)$ versus $\log_{10}(\sigma)$ using Eq. 2.17
b) $\log_{10}(\Delta_o)$ versus $\log_{10}(\sigma)$ using Eq. 2.13
c) $\log_{10}(\Delta f_o)$ versus $\log_{10}(\sigma)$ using Eq. 2.10
d) observed $\log_{10}(\Delta f_o)$ just above transition
e) observed $\log_{10}(\Delta_o)$ just above transition
f) $\log_{10}(\sigma)$ corresponding δ_s =1/2 of the smallest dimension .

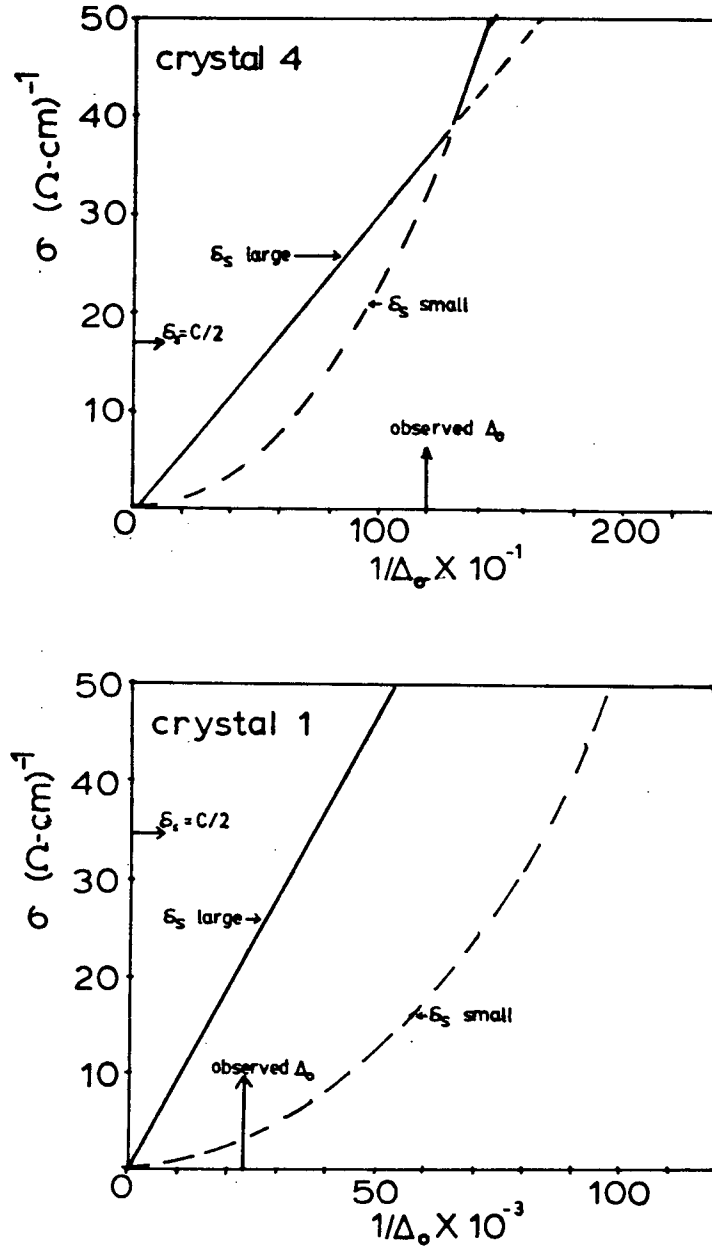

Figure 15b. σ versus $1/\Delta_o$ for assumption of large and small skin depth for crystals 1 and 4.

where $\log_{10} \Delta f_o$ is constant. Eq. 2.17 is taken to be valid to the right of that conductivity for which the skin depth is about half of the smallest dimension. In the intermediate region, Eq. 2.13 probably gives a better measure of σ than Eq. 2.17. The actual value of Δ_o observed is denoted by the arrow labelled (e). For crystal 4, we see that the observed change in width puts us onto the curves in a region where the two formulae give similar results. More importantly, this is a region where Eq. 2.17 is expected to be applicable since the skin-depth is less than half of the smallest dimension. For crystal 1, on the other hand, the observed loss is in a region where Eq. 2.17 implies a skin depth larger than the sample and is thus inconsistent. Eq. 2.13, however, does appear to be valid for crystal 1 in this regime.

In Fig. 15b, we have plotted σ versus $1/\Delta_o$ for these two crystals. For crystal 4, the observed Δ_o yields a similar σ for both of the assumptions about the skin depth. The skin depth limited calculation is preferred, in this case, as it avoids some of the uncertainty associated with the $((\alpha/n) - \Delta f_o)$ term in this regime. The true curve relating σ to Δ_o probably lies somewhat above the two curves in the region of the intersection. As a result, conductivities obtained close to the cross over between the skin depth limited and penetrating regimes are probably underestimated. For crystal 1, it is clear that skin depth limited penetration is inappropriate and Eq. 2.13 or 3.1

is to be preferred for the calculation of σ.

As a result of these considerations, the conductivities for crystal 1 above the transition were calculated using Eq. 2.13 with $\Delta f_o = \alpha/n$, and those for crystal 4 were calculated using Eq. 2.17. The other two crystals were intermediate cases and their conductivities were calculated using Eq. 2.17 above the transition.

We note here that there is some difficulty associated with the interchangeable use of α/n and Δf_o in the calculation of σ in the large $n\epsilon''$ regime. Equation 2.17 replaces α/n by Δf_o whereas in equation 3.1 it is effectively Δf_o that has been replaced by α/n. This problem represents an uncertainty that is intrinsic to these measurements in this regime.

3.2 Dielectric Constants and Conductivity

The microwave conductivities for the crystals measured appear in Fig. 16. The d.c. conductivity for one of the Groningen crystals appears along with the microwave conductivity for crystal 4, also from Groningen, in Fig. 17. The real parts of the dielectric constant below the transition temperature are shown in Fig. 18.

The $MEM(TCNQ)_2$ crystals were found to have a transition temperature of about 65°C on heating and 60°C on cooling. Although results obtained in another laboratory and reported in Morrow et al. (1979) have found these temperatures to be about 57.4°C and 51.5°C respectively there are also significant differences in the conductivity and the dielectric constant results below the transition which are not completely understood. The hysteresis of between 5 and 6 degrees is, however, common to both sets of results and is taken as evidence for the phase transition being discontinuous.

The real part of the dielectric constant, ϵ', could only be obtained below the phase transition as explained above, and was measured from just below the transition down to room temperature. An increase with temperature was observed with ϵ' going from between 10 and 12 at room temperature to between 12 and 16 at the transition temperature. As a check, the apparatus was used to measure the dielectric constant of a diamond sawed

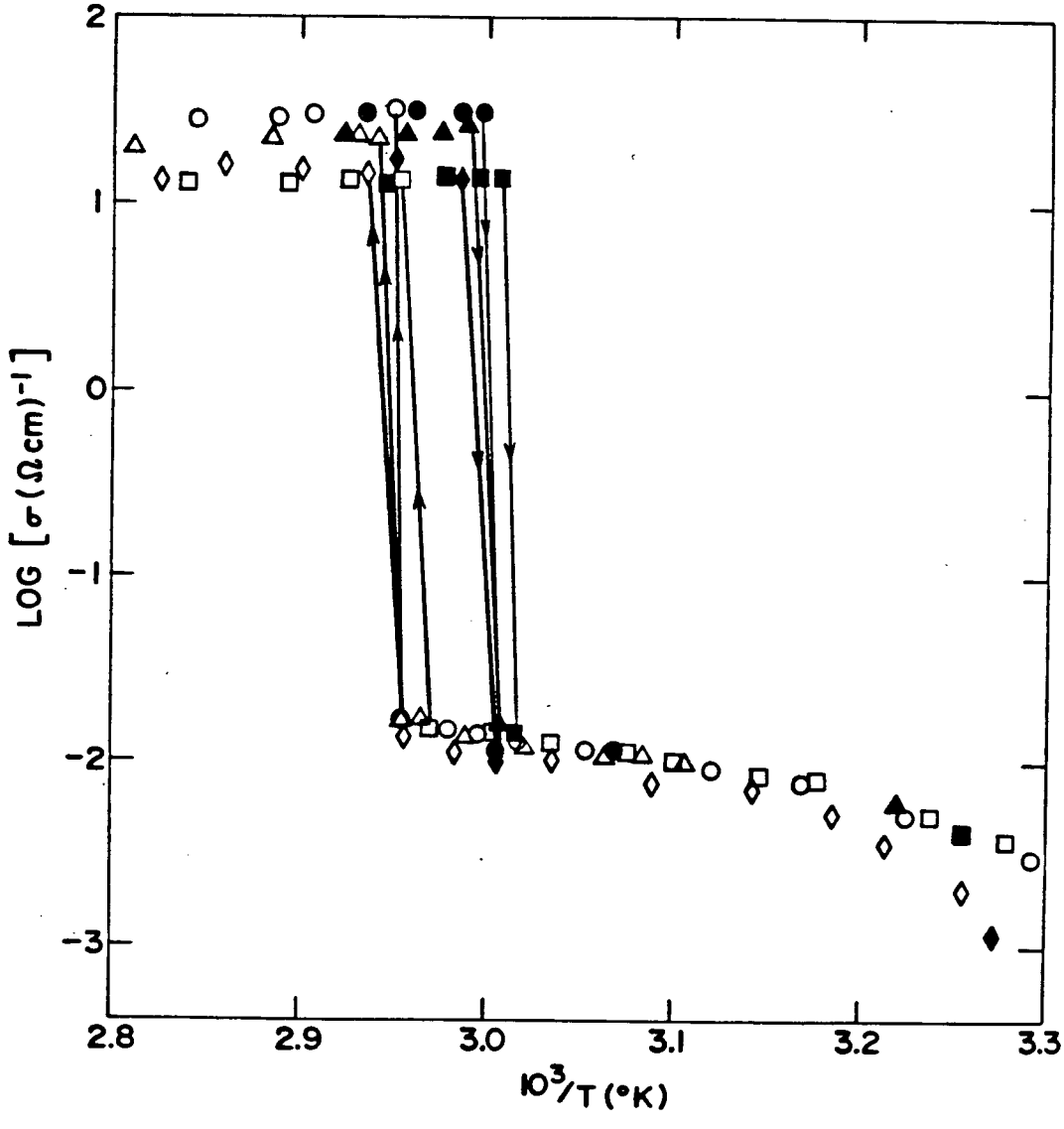

Figure 16. Microwave conductivities (8.5 GHz) for MEM(TCNQ)$_2$ crystals studied

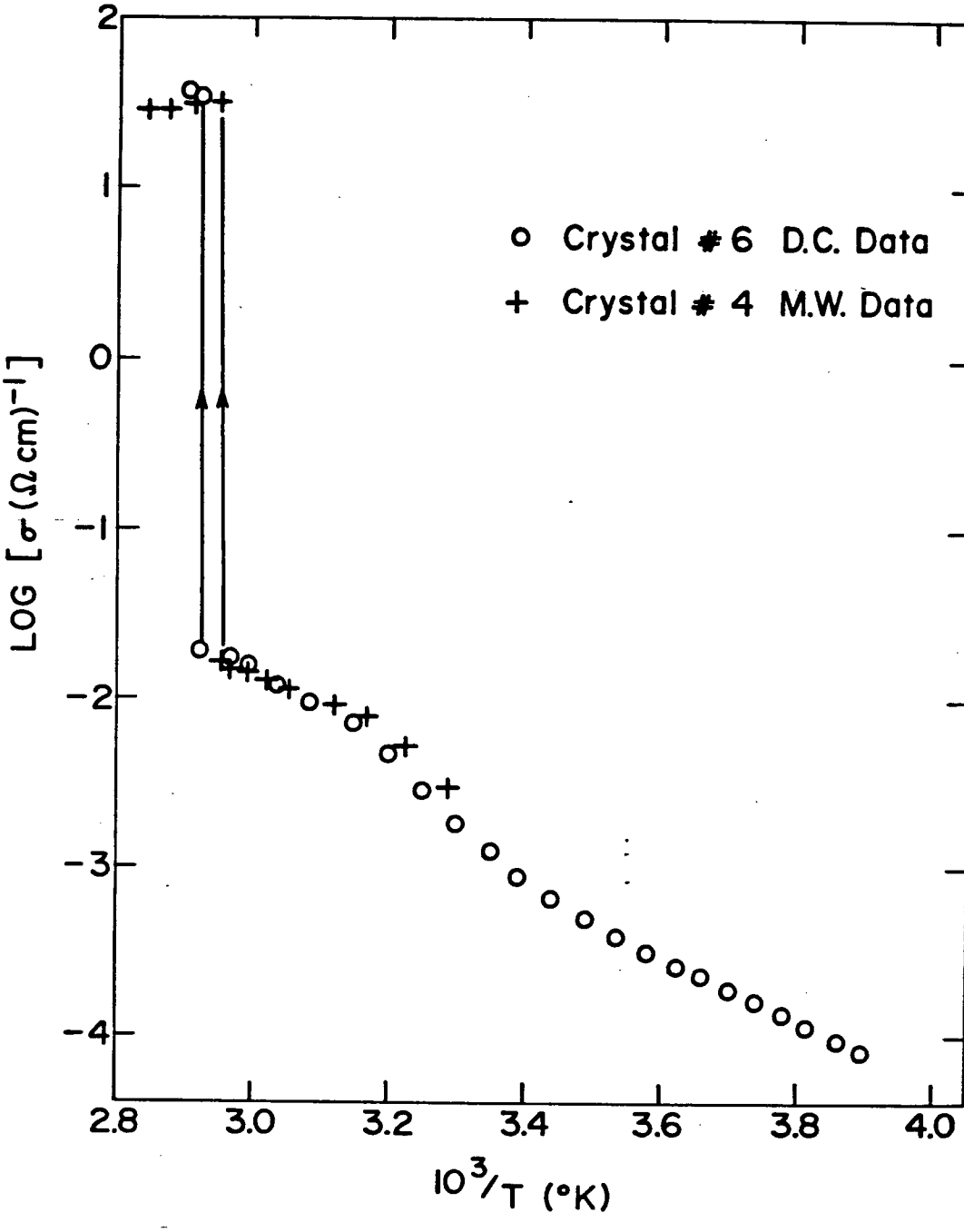

Figure 17. Comparison of microwave conductivity of crystal 4 and d.c. conductivity of a second MEM(TCNQ)$_2$ crystal plotted against 1/T.

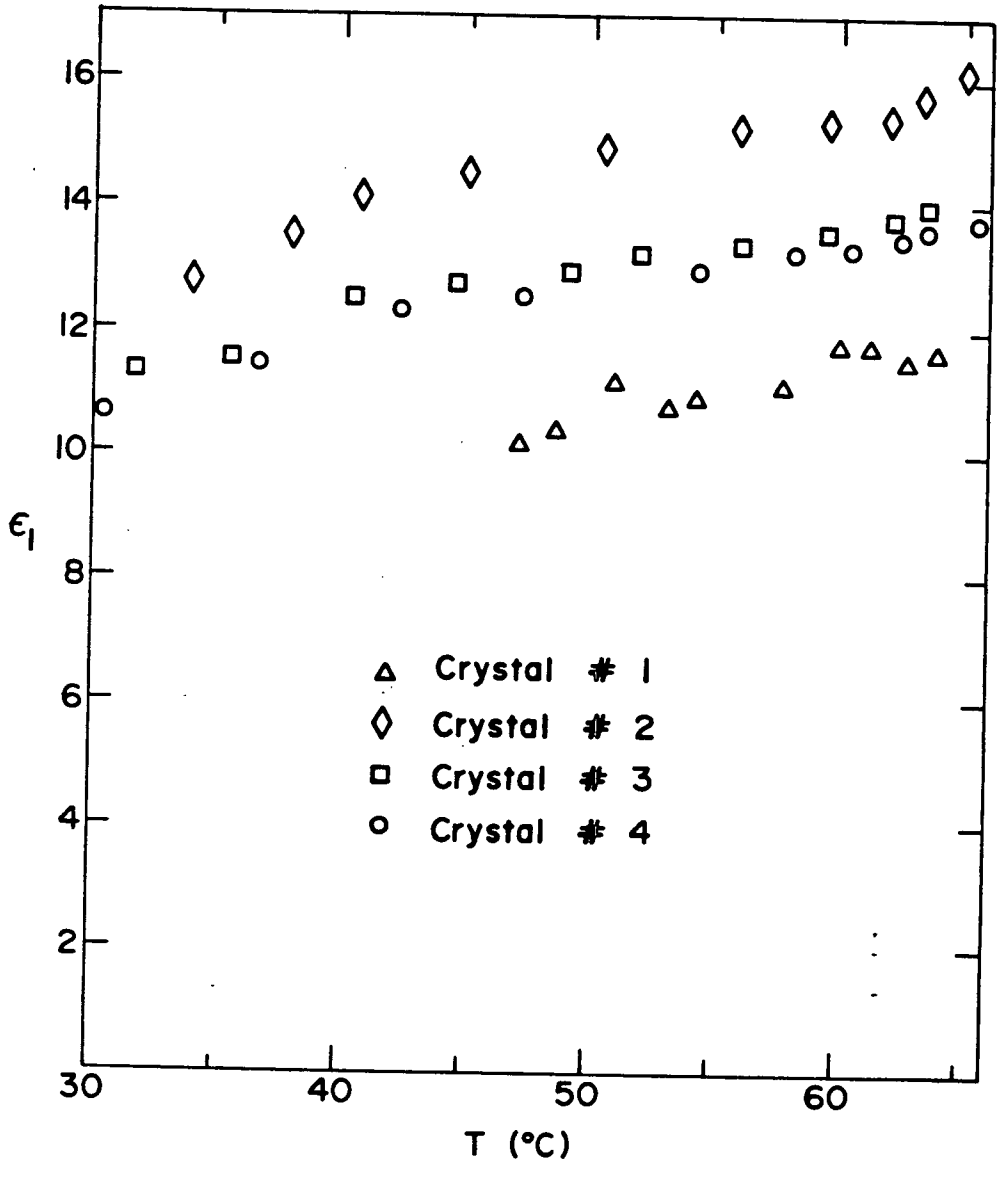

Figure 18. The real part of the dielectric constant versus temperature for some MEM(TCNQ)$_2$ crystals.

silicon chip of dimensions 0.820 cm by 0.099 cm by 0.065 cm. This chip, thicker than the $MEM(TCNQ)_2$ samples studied and not really optimally shaped for this technique, was found to have $\epsilon'=10.5$ as compared with the accepted value of 11.7.

The microwave conductivity in the low conductivity range was found to be between 0.014 and 0.017 $(\Omega\text{-cm})^{-1}$. The conductivity above the transition was found to be between 14 and 32 $(\Omega\text{-cm})^{-1}$. These results are included in the summary given in Table 2.

The conductivity below the transition can be analysed by assuming an activated behaviour so that

$$\sigma(T) = \sigma_0 \exp(-\Delta_g/2kT)$$

where Δ_g is the energy gap. In these measurements, Δ_g was found to be (0.7 ± 0.1)eV in the range from 310K to 335K. The d.c. measurements had previously given (Morrow et al., 1979) $\Delta_g=0.78$eV between 250K and 290K and 0.69eV between 310K and 335K. The microwave measurements covered only the upper range of temperatures but were generally found to confirm the d.c. results.

Errors were estimated for a typical point above and below the transition. Below the transition, the error in ϵ' was found to be about 30% and that in ϵ'' and σ to be about 35%. These were largely associated with the uncertainty in the crystal

TABLE 2

Calculated Results for MEM(TCNQ) Crystals Studied

Crystal	1	2	3	4
$\sigma_{\perp}$ $(\Omega\cdot cm)^{-1}$ (T<65°C)	0.0165	0.0142	0.0149	0.0161
$\sigma_{\parallel}$ $(\Omega\cdot cm)^{-1}$ (T>65°C)	22.292	14.53	13.62	31.39
$\sigma_{\parallel} / \sigma_{\perp}$	1351	1023	914	1950
ϵ' (T=50°C)	11	15	13	13
δ_s (cm) (T<65°C)	0.424	0.457	0.447	0.430
δ_s (cm) (T>65°C)	0.0115	0.0144	0.0148	0.0098
$(\alpha/\Delta f_o)/n$ (T>65°C)	1.249	1.267	1.264	1.142
$n\epsilon''$ (T<65°C)	0.0564	0.0324	0.0444	0.0287
$n\epsilon''$ (T>65°C)	76.425	33.42	40.81	57.18

dimensions and do not include the small systematic error in n due to the non-ellipsoidal shape. Above the transition, the experimental uncertainty in σ' is estimated to be about 20 %.

3.3 Discussion

$MEM(TCNQ)_2$ is found to be a semiconductor with a gap of about 0.8eV in the dimerized phase and a poor metal in the high temperature phase. There is some suggestion that the MEM ions play a role in stabilizing the dimer and that the transition is related to the loss of this stabilization with the increased motion of the MEM ions at higher temperature. (Sawatzky, 1979) For the purpose of this discussion, however, we will just consider the effect, on the extended Hubbard model for the $\rho=1/2$ TCNQ stack, of the three kinds of terms in the extended Hubbard Hamiltonian. We will be interested in the relationships between the overlap integrals and the on-site repulsion, U, and, in particular, on whether or not the results presented here can distinguish between the large U and small U cases.

It is clear, from the fact that the transition is not directly from the monomer to the tetramer phase, with characteristic wavevector $2k_F^o$, that Coulomb repulsion must be significant.

In the monomer phase, we can think of there being just one transfer integral, t. Then, for $U<<4t$, we will have a tight binding model with a quarter filled band of width 4t. For $U>>4t$, we will have the spinless fermion model with a gap of U-4t and a lower band of width 4t. Both of these will give a metal-like behaviour. If, however, the nearest neighbour

repulsion were large, then one would expect, for the $\rho=1/2$ and large U case, a Wigner crystal situation with a gap above the highest filled level since any excitation would involve occupancy of neighbouring TCNQ molecules. That the conductivity is not extremely high suggests that V_1 might be important. The conductivity does not, however, appear to be activated so this question remains unresolved. The high temperature behaviour, then, does not distinguish between any of the extreme regimes of the Hubbard model.

If we now look at the semi-conducting dimer phase, we can consider two possibilities in terms of t_1 being large or small. We already suspect that U is large because the tetramerization does not occur immediately. The ground state of the dimerized phase does not include double occupancy of TCNQ molecules.

We will first consider the situation where t_1 is the dominant interaction. If we ignore the Coulomb repulsion for the moment, we can consider the problem to be a tight binding problem in a lattice of cell dimension c with a basis b. We will take the overlap of sites separated by b to be $-t_1$ and those separated by c-b to be $-t_2$. The Brillouin zone then extends to $\pm\pi/c$. We find the dispersion relation to be (Appendix A)

$$\epsilon_k = \pm\sqrt{t_1^2 + t_2^2 + 2t_1 t_2 \cos(kc)} \quad . \tag{3.3}$$

This expression describes a band with limits at $\pm(t_1+t_2)$ with a gap between $\pm|t_1-t_2|$.

We can now study the effect of including the on-site repulsion. We assume that t_1 is much larger than t_2. This leaves three cases to consider. These are $t_1>>t_2>>U$, $t_1>>U>>t_2$, and $U>>t_1>>t_2$.

For the first case, we expect the result to be similar to that discussed above so that we have a lower band of width $2t_2$. Double occupancy of the dimers is allowed so this lower band would be half-filled and thus metallic. This is inconsistent with the conductivity measurements and with the fact that the magnetic susceptibility measurements (Huizinga et al., 1979) indicate that MEM$(TCNQ)_2$ is a chain of localized spins with antiferromagnetic coupling rather than a metallic chain for which the much smaller Pauli susceptibility would be appropriate.

For the second case, $t_1>>U>>t_2$, the half filled lower band is split by the Coulomb energy associated with double occupancy of a dimer. This will be U/2 since the probability of double occupation of a given TCNQ molecule in a doubly occupied dimer is 1/4. The gap is thus $U/2-2t_2$ below which is a filled band of width $2t_2$.

In the third case,U dominates the problem and we can handle this by recognizing that, as in the case for a single type of overlap, this is just the U=0 case for spinless fermions. The

result is then two bands of width $2t_2$ with a gap of $2(t_1-t_2)$. Now, however, the lower band is filled.

We see, then, that both of these last two models give a semi-conducting phase and, as for the metallic state, we cannot distinguish between U dominating and t_1 dominating on the basis of conductivity measurements. For both cases, nearest neighbour repulsion, V_1, would also contribute to the gap if it was non-negliglible.

We thus find that, for both $U>>t_1$ and $U<<t_1$, we would expect to find a gap for conductivity and a gap of about 9000 degrees is observed. The thermopower evidence of Chaikin (1979) suggests that U is in fact large and this is consistent with the conclusions drawn by Huizinga et al. (1979). If the gap is taken to be $2t_1-2t_2$, as for the large U case, the implication is that t_1 is of the order of 0.4 eV. Based on Hubbard's (1978) estimate for a TCNQ chain of of U=4.5 eV for the unscreened case and 2.4 eV if the interaction is screened by conduction on neighbouring chains and polarization of neighbouring molecules, this is indeed small compared to U.

CHAPTER IV

Dielectric Resonator Studies of TTF-TCNQ

The second part of this work involved the study of the complex dielectric constant of TTF-TCNQ for the direction parallel to the conducting axis by observing dielectric resonances of the crystals. This axis is labelled b in what follows.

4.1 Dielectric Resonator Apparatus

The apparatus used for this part of the work was essentially the same as that used by Barry for the original dielectric resonance studies of TTF-TCNQ (Barry, 1977).

The nature of the experiment required that it be possible to suspend the crystal in the wave guide at low temperature and manipulate it from room temperature. It was also necessary that it be possible to extract the crystal for cutting while leaving the wave guide at liquid helium temperatures.

This was accomplished by suspending the crystal from a quartz fibre on the end of a long stainless steel rod which could be manipulated from the top of the cryostat. A detailed diagram of the crystal handling rod and rod holder appears in Fig. 19. The crystal, with its long axis parallel to the rod assembly, was butted against the end of the quartz fibre and held with a type of fast-setting epoxy (5 min.) manufactured by

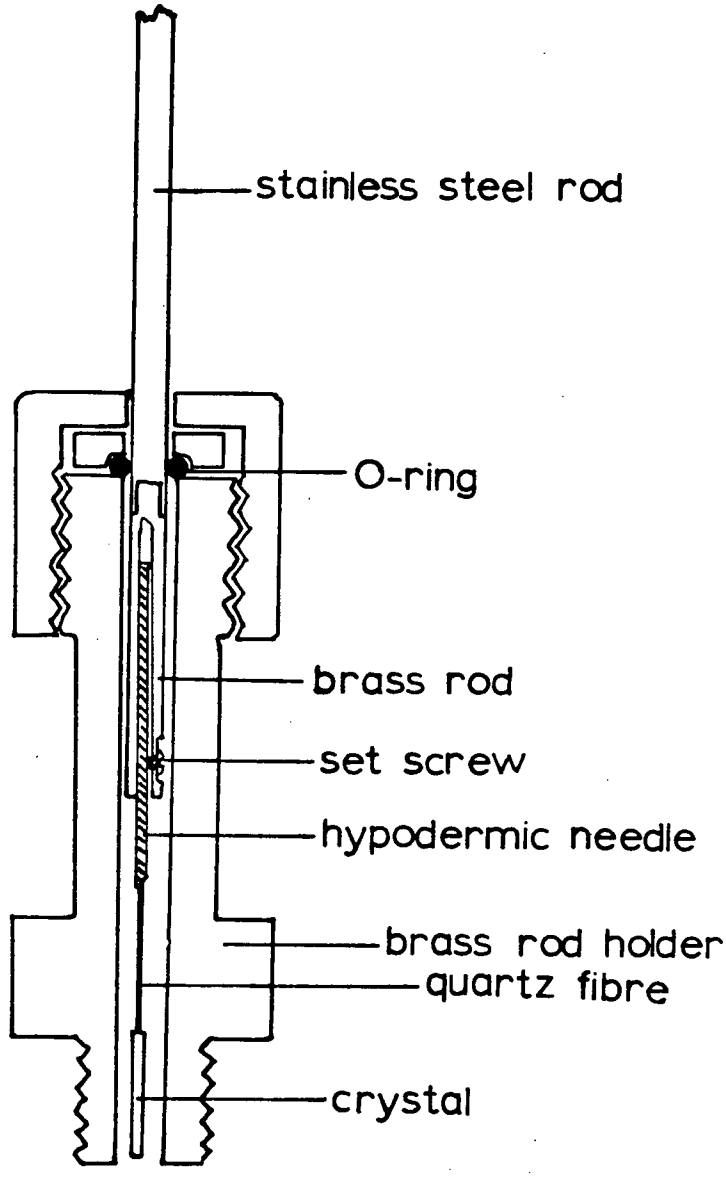

Figure 19. Crystal manipulating rod and rod holder for the dielectric resonance experiment.

Devcon. This quartz fibre was glued into a 26 gauge hypodermic needle with approximately half an inch of quartz fibre projecting from the needle. The needle, in turn, was fitted into a concentric hole in a brass tip of the same diameter as, and fitted into the end of, the stainless steel rod. This stainless steel rod, of length 62 cm, was inserted into a brass holder with an O-ring seal to secure the rod. The brass holder was threaded so that it could be attached to the cryostat flange. A spring was captured between the brass cap of the O-ring seal and a cap on the stainless steel rod.

The crystal could be withdrawn into the brass holder, after mounting, to allow it to be moved to the cryostat. The brass holder could then be screwed into a threaded hole on the top cryostat flange. A stainless steel tube was used to guide the rod and crystal down to and through a copper block and into the wave guide. The crystal was oriented with the long axis perpendicular to the E field in the rectangular wave guide. The copper block, in which was inserted a 390Ω carbon resistor thermometer, supported a 120Ω resistance wire heater and also formed a short at the end of the wave guide. The wave guide formed a "U" shape with one arm shorted by the copper block and the other extending through the top flange of the cryostat. A polyethylene window was used to seal the wave guide outside of the dewar. There was a hole drilled in the waveguide just above the operating liquid Helium level to allow He gas to enter and

cool the crystal. Two wave guide assemblies, to cover 18 to 26.5 GHz and 26.5 to 40 GHz ranges, could be interchanged.

Since a given crystal had to be used for a number of measurements, in order to construct a mode plot, it was desirable to minimize the opportunities for breakage. One of the most likely times for the crystal to fracture was during the insertion after a liquid He transfer. To minimize the number of transfers necessary to collect data from a given crystal, as well as to conserve He, the relatively heavy stainless steel skirt of Barry's apparatus was replaced by a flange supporting three thin-walled tubes. The smallest tube contained the thermometer and heater wires as well as the tube in which the crystal manipulating rod was guided. The largest tube contained the wave guide assembly and the remaining tube guided the transfer siphon to the dewar. These tubes passed through O-ring seals on the top of a second flange which was sealed to the dewar. The tubes and upper flanges supporting the waveguide and crystal handling assemblies were fixed in place while the dewar could be raised and lowered on the tubes by means of a simple elevator mechanism. The dewar assembly is shown in Fig. 20.

It was found that the vibrations associated with the He transfer were often enough to break the crystal so that the crystal had to be inserted after the transfer. This required careful use of techniques to insure that there was no condensation of ice in the dewar and particularly in the crystal

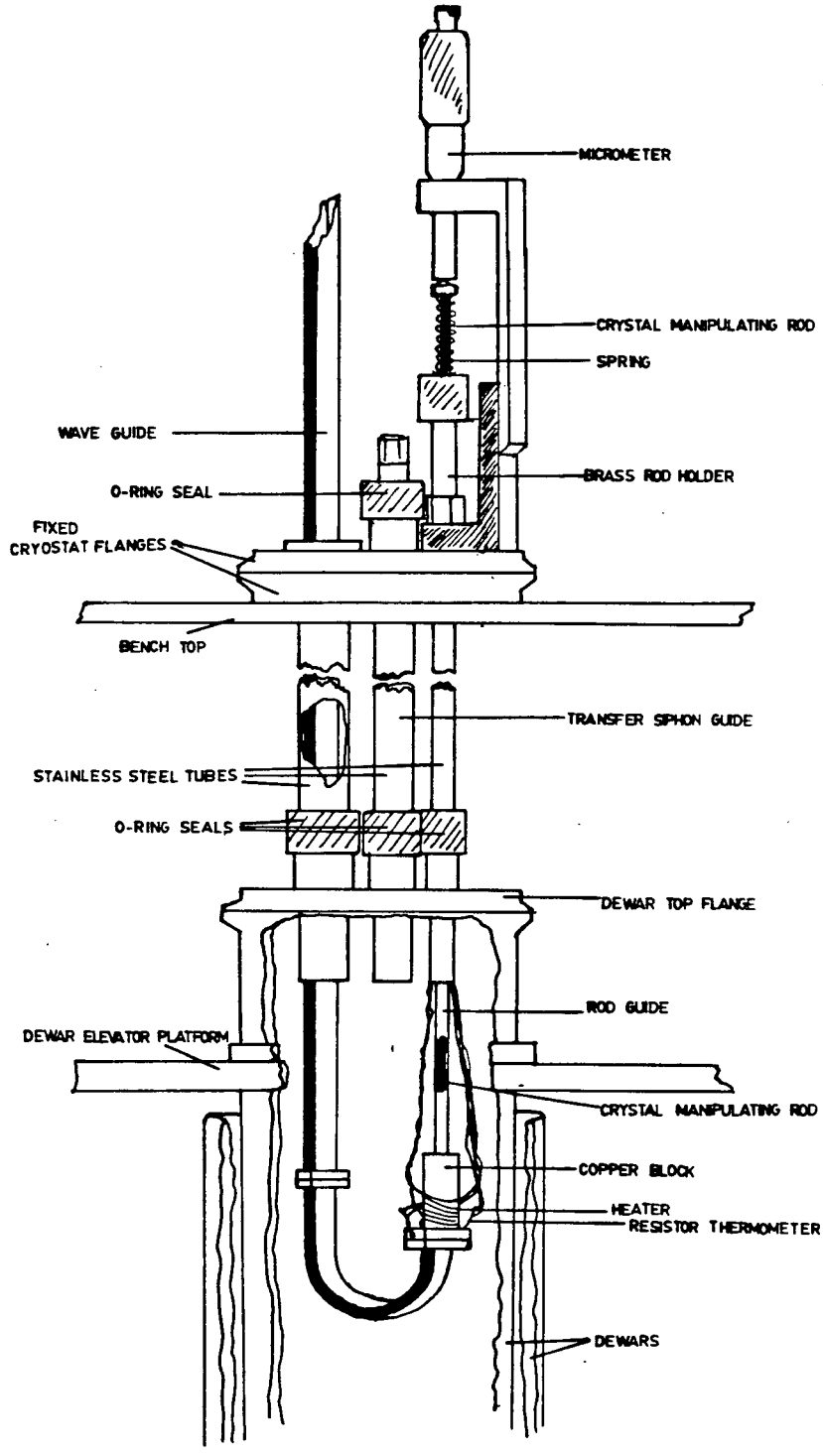

Figure 20. The dewar assembly for the dielectric resonance studies of TTF-TCNQ.

insertion tube. While the failure rate was still high, it was found that some success could be achieved by leaving a dummy rod in the crystal insertion tube during transfers along with maintaining a He overpressure at all times. The dummy rod prevented the blockage of the tube by condensable vapours during transfers and could be used to clear blockages from the tube prior to insertion.

4.2 The Spectrometer

The microwave sweep oscillator employed in these measurements was a Weinschel 221 with 18 to 26 GHz and 26 to 40 GHz plug-ins. The microwave power was sampled at the plug-in with a 10 dB directional coupler. It passed through a wave meter and a variable attenuator to a Hewlett Packard model 11517A harmonic mixer which could be used for phase-locking purposes as described below. The wave meter was used to convert the external sweep voltage to frequency. The power level was detected, at a second directional coupler, by an HP model R422A crystal detector and used to level the backward wave oscillator output. After passing through an isolator, it was sent to the microwave assembly through a third directional coupler. The power reflected from the short, less any absorbed by the crystal resonance, returned up the wave guide assembly and through the directional coupler, a variable attenuator, and an isolator, to a second HP harmonic mixer used as a simple detector. The output was amplified in two stages by inverting operational amplifiers before being fed to the computer through a digital to analog converter. The data handling from this point will be described in section 4.6. Fig. 21 illustrates the microwave assembly schematically.

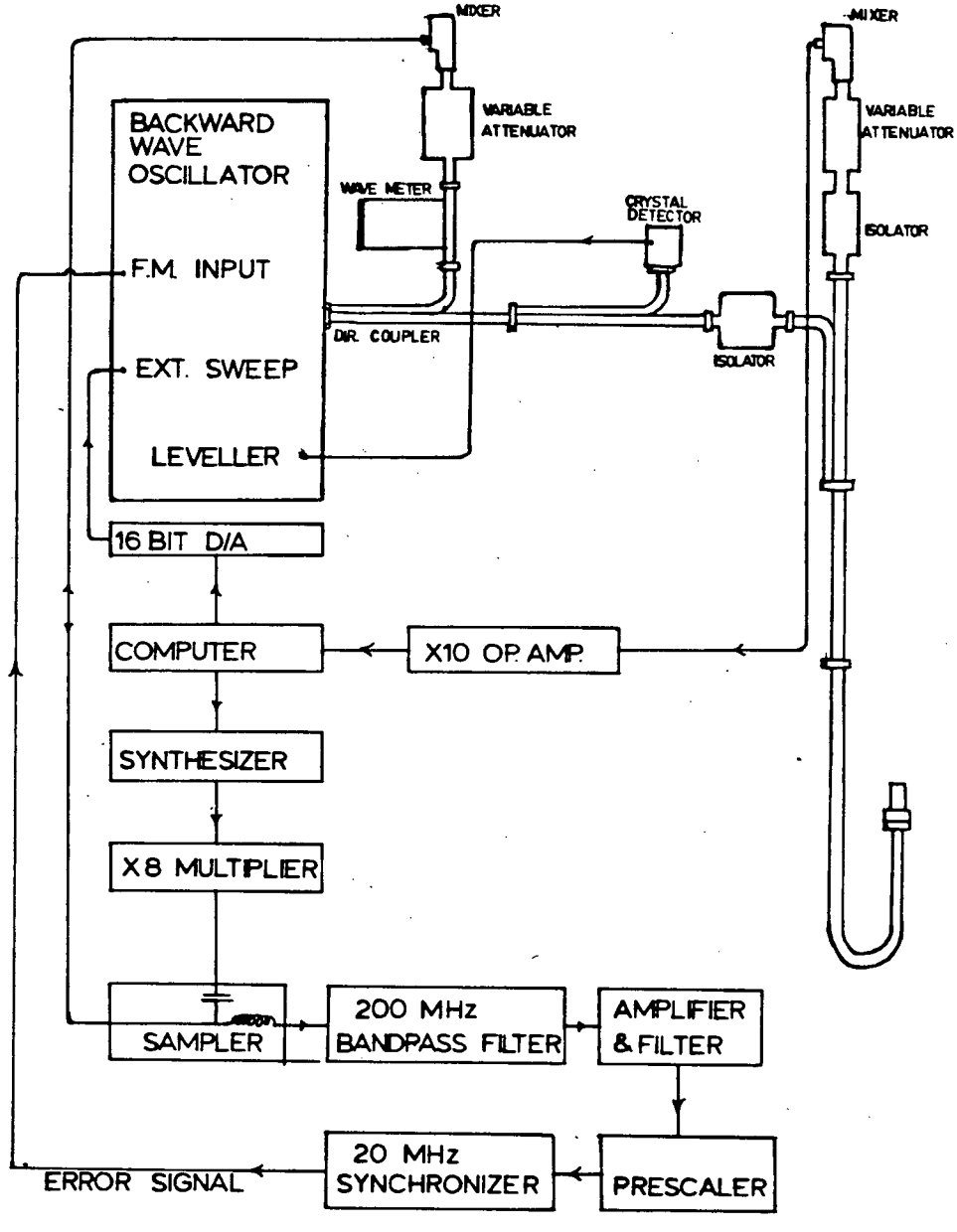

Figure 21. Schematic drawing of the microwave apparatus used for dielectric resonance measurements.

4.3 Crystal Cutting

It was felt that in order to better understand the dielectric resonance mode plots, it would be necessary to have a means of trimming small lengths from the crystal quickly and with a minimal risk of crystal breakage. To this end an assembly was constructed which could be used to mount the crystal under a microscope and could then allow the crystal to be manipulated in two dimensions and cut while under observation. The apparatus used is shown in Fig. 22 as it appears on the microscope mount. The mount assembly (A) attaches to the microscope arm using dovetail B. The rest of the assembly is supported by rails which are inserted through block C. This block can be translated perpendicular to the direction of the rails by means of an adjusting knob. The rod on which the crystal is mounted can be translated parallel to the rails by means of the four assemblies D, E, F, and G. Support D contains a threaded hole into which the brass crystal support can be screwed. Support E, with the cap in place, steadies the crystal mount rod and provides a base for the spring which remains on the rod at all times. Collar F can be placed around the rod and clamped to it. The spring presses against it to provide the force to return the crystal to the block. Part G contains a fork through which the rod is passed and which presses on collar F to move the crystal toward the

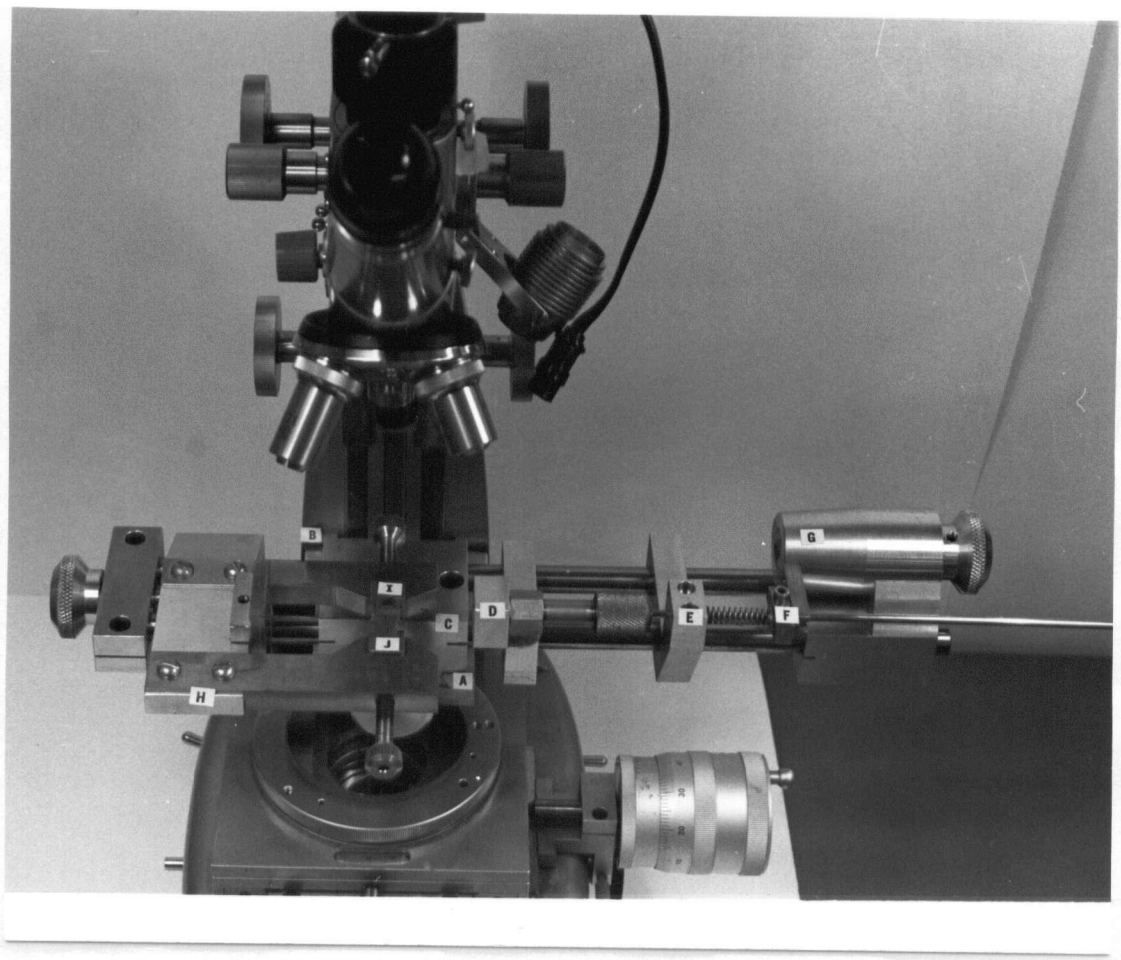

Figure 22. The crystal cutting apparatus mounted below microscope. For a description, see text.

centre of the apparatus. At the other end of the rails is the cutter assembly (H) which can be translated along the rails to position the blade below the microscope. The actual cutter consists of an anvil (I) to support the crystal and a blade (J) to cut it. Both are moved by differential screws mounted in removable brass arms. A piece of razor blade steel epoxied to the anvil forms the cutting table. This table must be hard so that grooves, into which the crystal can be pushed, are not formed. The blade was a section of razor blade. Best cutting results were obtained when the blade was changed for each crystal. It was found that, in the cutting process, it was possible for the blade to exert a force on the crystal that was parallel to the crystal's long axis. Since the crystals are extremely weak in compression, this force had to be compensated for. This was done by backing off the fork on part G once the blade had pinned the crystal to the anvil. This allowed the cut to proceed with a slight tension, supplied by the spring, applied to the crystal. Photographs showing the cutting operation and the end of the crystal appear in Fig. 23. While the cutting operation is not a cleaving of the crystal, it was found that reasonably clean cuts could be made with no apparent degradation of the dielectric resonance.

The major purpose for the cutter was to allow the crystal length to be changed by very small amounts. It was found that as little as about 0.3 mm could be trimmed from the crystal

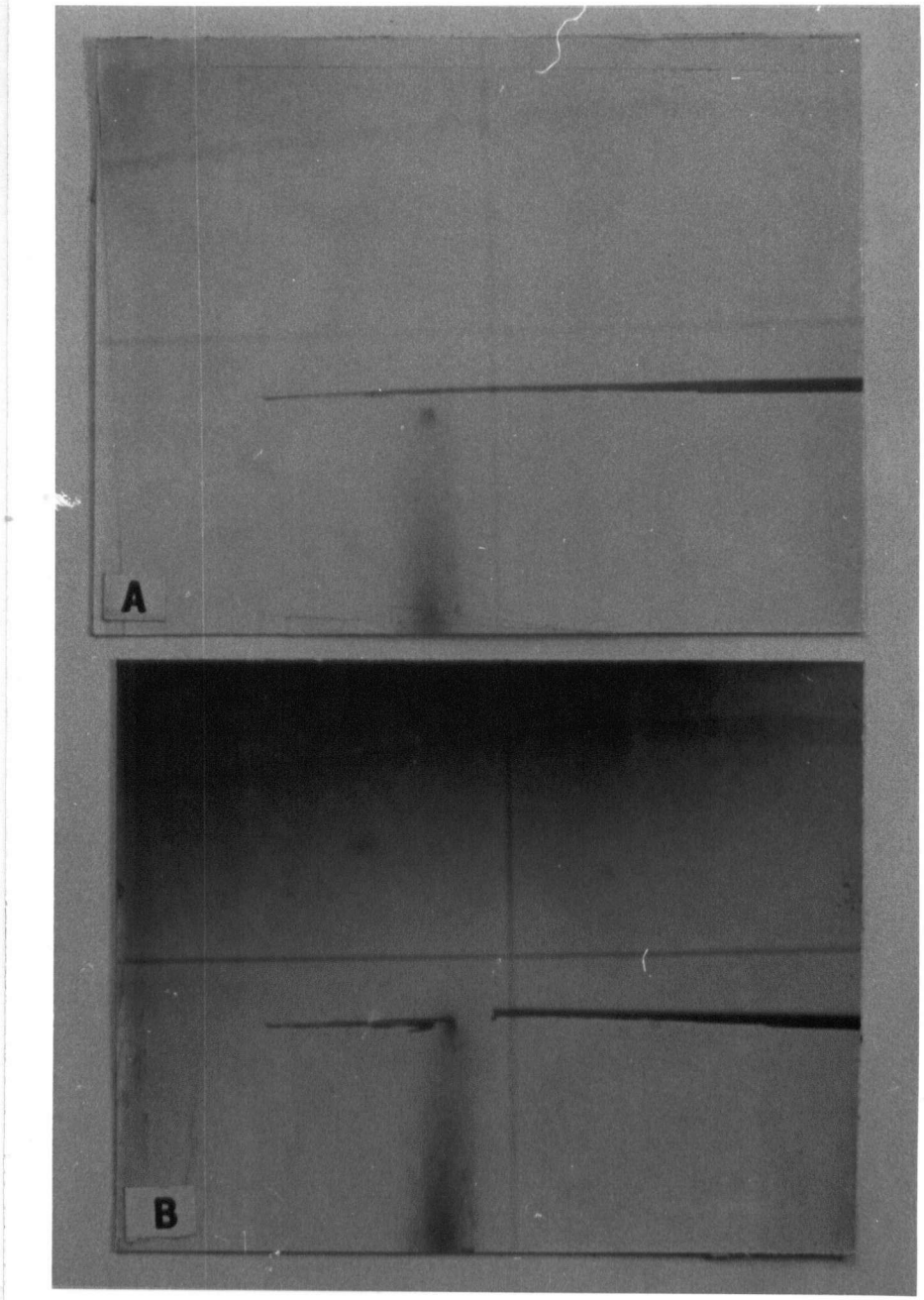

Figure 23. Crystal and blade before and after cutting operation. Anvil has been withdrawn for clarity.

quite easily. For cuts of less than 0.1 mm, there was some difficulty with the blade crushing the end of the crystal resulting in a slightly ragged cut.

4.4 Mounting

This same assembly was also used to mount the crystal. For this operation, it was mounted vertically on a stand as shown in Fig. 24. The blade and anvil were retracted to allow the mount rod to pass between them. The rod, with the needle and quartz fibre mounted in the end as described earlier, was held in the assembly in the same way as for the cutting operation. The crystal was stood upright in a small hole drilled in the brass block (K). The block rested on a table fixed to the cutting assembly as shown (L). The rod was then lowered against the spring using the fork and collar arrangement. With a drop of epoxy on the quartz fibre, the crystal and fibre were butted together and then raised slightly. The brass block was positioned so as to hold the crystal straight while the epoxy hardened. The rod and crystal were then withdrawn into the barrel of the brass crystal support in preparation for transfer to the dewar.

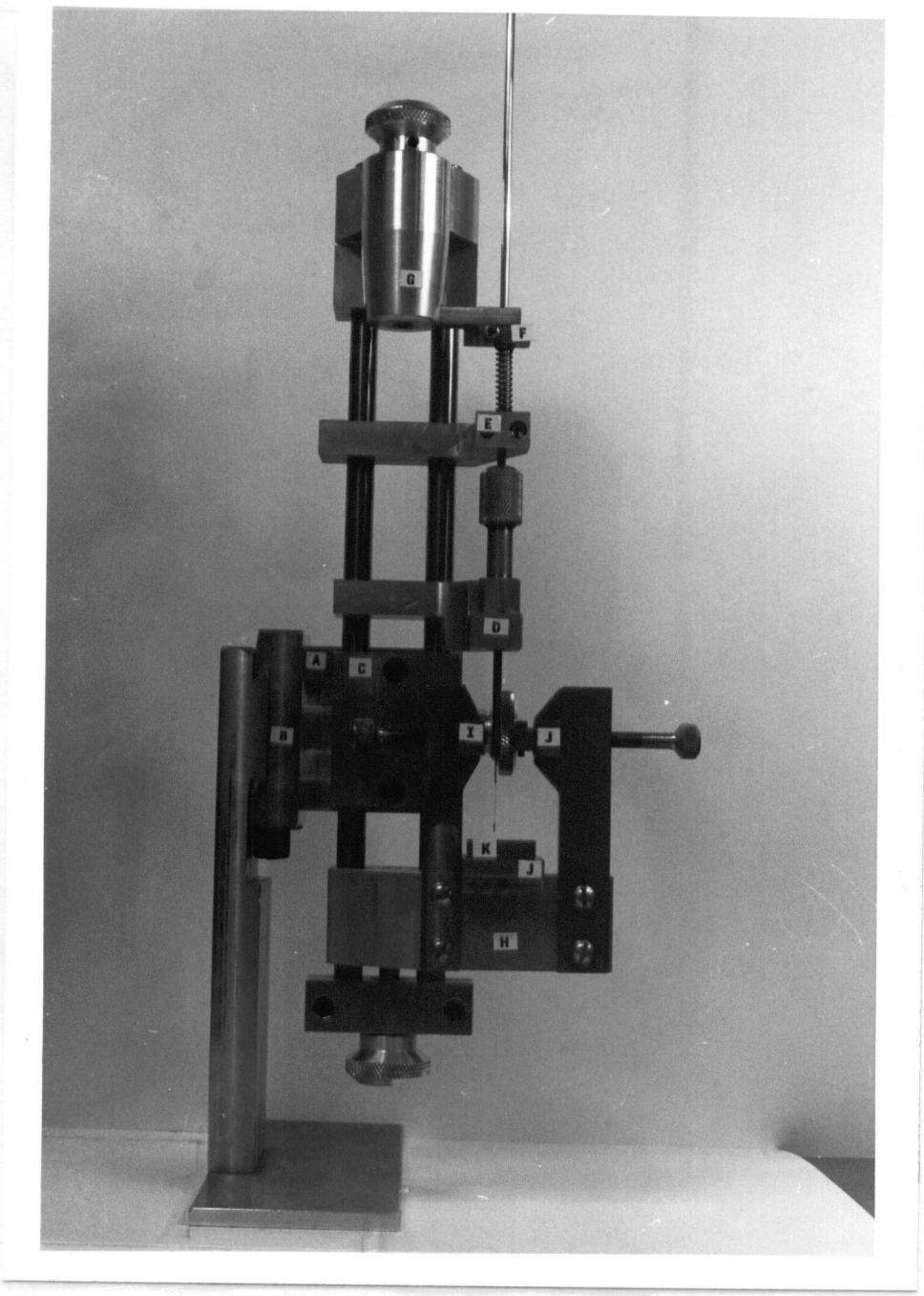

Figure 24. Crystal mounting apparatus. see text for description.

4.5 Measuring of the Crystal

The crystal could be measured from photographs taken through the microscope. This method was accurate to about 0.01 mm. Later crystals were measured by attaching the crystal holder to a stage which could be translated in two dimensions using micrometers. These measurements are thought to be accurate to 0.005 mm or less.

4.6 Computer Control

The microwave source was controlled by a Nova 2 minicomputer as described by Statt (1979). Its use in the context of this experiment will be described briefly.

Any operation involving sweeping of the backward wave oscillator (BWO) under computer control required that a suitable voltage ramp be fed to the external sweep input of the BWO. The first step in generating this ramp involved calibration. This was done using the BASIC program, "CALIBRATION." A digital ramp was output to the 16 bit D/A converter. A wavemeter (TRG K551 for 18 to 26.5 GHz and TRG A551 for 26.5 to 40 GHz) could be used to identify preselected frequency points in the sweep. The computer was signalled manually at each preselected point and the digital output giving rise to the appropriate voltage recorded on disk.

In order to collect data, the program "SWCONTROL" was used. Two modes of sweeping were used for this experiment. Because of the presence of strong standing waves between the short and the polyethylene vacuum seal, it was usually necessary to ratio spectra taken with the crystal in and out in order to locate all but the most strongly coupled resonances. This initial search for each resonance was performed using the "FASTSWEEP" routine with a real time ratio option. In this mode of operation, the computer used the frequency calibration previously obtained to

calculate a digital ramp covering the frequency range requested with the number of points requested. This ramp was then output to the 16 bit D/A at a selected rate. At the same time reflected power was being sampled and ratioed, point by point, with the previously stored background. Each ratioed point was displayed on a scope monitor before the next point was taken. This routine was typically used for repetitive scanning of 1001 points over about 2 GHz at a rate of 100μsec. per point. For both this routine and the synthesizer phase locking routine, the spectra could be retaken with only the storage locations altered by using the response "R". This allowed quick recording of background and crystal spectra without re-entering all of the sweep parameters. Features in the ratioed spectrum could be identified as crystal resonances by moving the crystal, and thus changing the coupling, while observing the ratioed spectrum in real time. The gain of the displayed ratio could be increased by up to a factor of 16. Using this option, resonances coupled by less than 5% could be located. The coupling was usually adjusted to a maximum so that for strongly coupled resonances there was no question as to whether the resonance was over-coupled or under-coupled.

The data was normally collected with the source phase-locked to the Rhode and Schwarz 0.01 to 500 MHz frequency synthesizer. These could both be controlled by the "SYNSWEEP" routine in "SWCONTROL". These scans typically covered 0.5 GHz

with 1001 points at 100 msec./point. Again a 1001 point digital ramp would be calculated and fed, point by point, to the BWO. At the same time, the computer would output a signal to set the synthesizer to a frequency such that a chosen harmonic of 8 times the synthesizer frequency would be 200 MHz greater than the desired BWO frequency. (the synthesizer output is fed through a times 8 multiplier chain before entering the HP harmonic mixer which was also sampling the BWO output.)

The result of mixing the BWO output and the chosen harmonic (between 6 at 18 GHz and 11 at 40 GHz) of the multiplied synthesizer output would include a signal close to 200 MHz. After being picked out by a bandpass filter and divided by 10, the signal was fed to a 20 MHz synchronizer. This generated an error voltage which was then fed to the F.M. input of the BWO to correct its output frequency. The power reflected was sampled at each frequency step and the result stored. The contents of the buffer containing the spectrum were displayed on the monitor scope after each point was collected. The usual procedure was to store the spectrum with the crystal inserted and then to record a background signal. The ratio was then calculated and stored on disk using the "ANALYSIS" program. This program was also used to plot the spectra on an X-Y recorder. Before being stored on disk by an assembly language subroutine, the ratioed spectra were multiplied by a large number in order to reduce the digital noise associated with floating point to fixed point

conversion of small numbers. Consideration of the monitor scope range led to the choice of 2^{14} as a convenient multiplier.

4.7 Fitting of the Spectra

The resonance was analysed by assuming a Lorentzian oscillator line shape for the absorption due to the dielectric resonance. Ideal ratioed spectra are assumed to have the form of 1 minus a Lorentzian curve. The spectra can be fitted to such a line shape using the "AFIT" or "MFIT" programs. These programs can be called from the "ANALYSIS" program by responding to the prompt with "Z". Both request a directory in which they may find requested files. They can perform disk operations and scope monitor plots by responding to the prompt "%" with the letters "D" or "P" respectively. These commands are used in the same way as in "SWCONTROL" (Statt, 1979). The response "L" results in the computer requesting information on the spectrum to be fitted and then carrying out the fit. The first query requests the baseline factor, as described above, to be entered. Next information is requested about the spectrum to be fit including the initial frequency, the frequency interval, the number of points, and the location, in the BASIC buffer, of the first point. It then asks for a guess as to the centre frequency and width of a Lorentzian with the same height as well as the first location into which to store this Lorentzian.

In the manual program, "MFIT" , this Lorentzian is calculated and stored. The response "C" brings a request for the locations and lengths of two blocks of buffer space

containing the original and calculated spectra and then plots them simultaneously for visual inspection of the fit. "CV" will do this as well but will respond to the escape key by summing the square of the differences of the two spectra. The computer will then respond to "LI" by requesting a new set of parameters for the Lorentzian but retaining the original spectrum. "CI" will plot the contents of the blocks specified in the most recent "C" command and, as is also true for "CV", will not work unless a "C" command has been used previously. In manual fitting, then, one would simply vary the Lorentzian parameters until the sum of the squared differences was minimized.

In "AFIT", the requested centre frequency of the required Lorentzian , is a dummy variable. The program locates the lowest point in the spectrum, corresponding to the centre for an ideal Lorentzian absorption, and calculates the Lorentzian absorption with that height and centre frequency and with the width supplied. The sum of the squared differences is then calculated. The width is then changed by twice the frequency interval supplied and the procedure repeated. The width will change in the appropriate direction until the fit parameter is minimized at which point the procedure will be repeated for the centre frequency. The parameters of the Lorentzian giving the best fit, plus the per-cent coupling of the resonance, will then be output. The fit can be checked manually by using the "C" command as described above. Fig. 25 shows observed spectra and

the best fit Lorentzian for typical cases of a well fit resonance and for a poorly fit resonance.

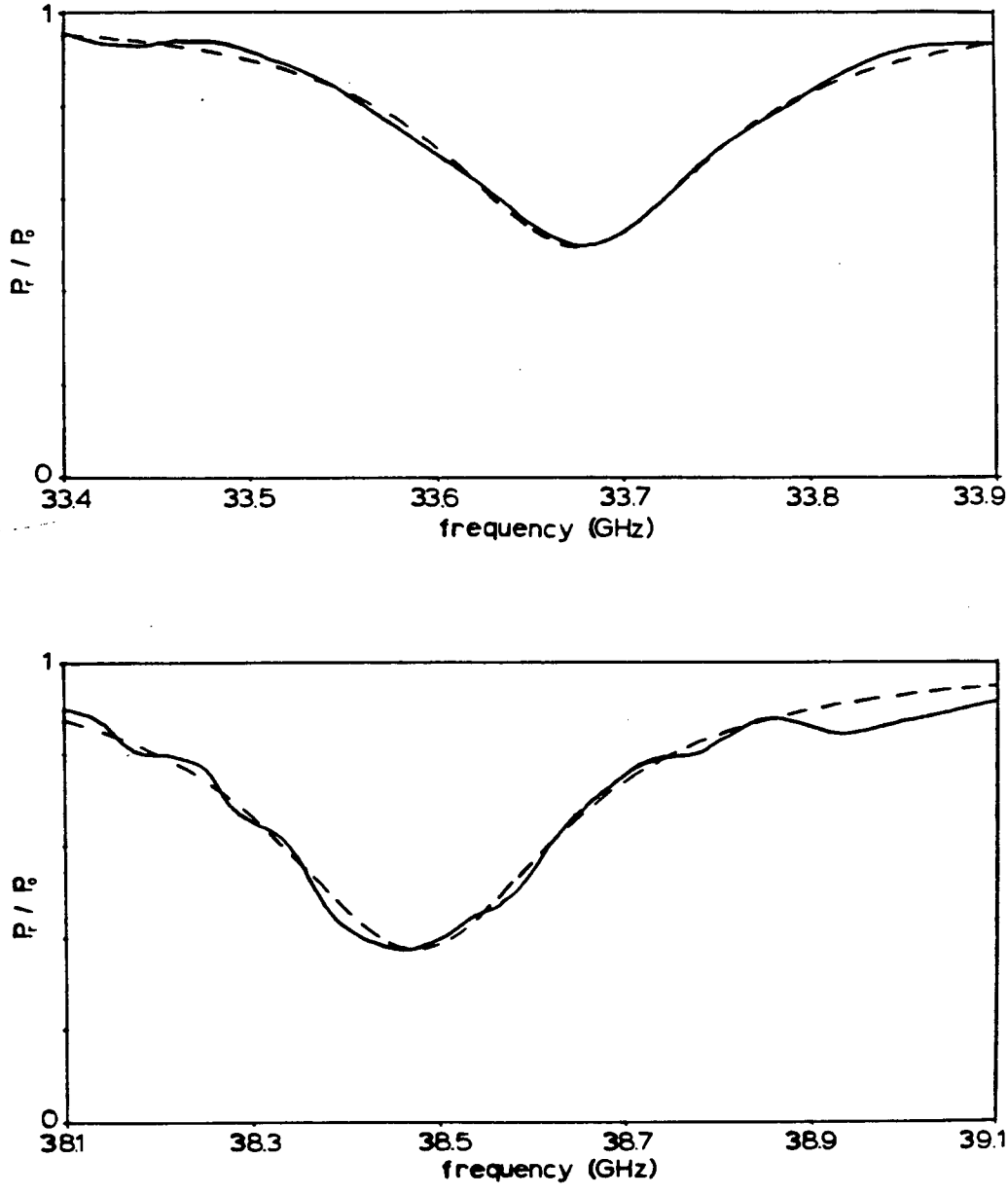

Figure 25. Examples of observed resonances (solid lines) and best fit obtained using "AFIT" program (dashed line).

CHAPTER V

Theory of Anisotropic Dielectric Resonators

5.1 Introduction

Because of the possibility of total internal reflection at the surface of a dielectric and vacuum, a dielectric solid can be made to act as a microwave cavity. This was first considered by Richtmeyer (1939) and applied by Okaya and Barash (1962) who used a resonator made of rutile. Dielectric resonators have since been used both in engineering applications and as a technique for measuring dielectric properties of small crystals. Dielectric resonance has been applied to studies of $K_2Pt(CN)_4 Br_{0.3} 3H_2O$ (Jakelic and Saillant, 1974) and TTF-TCNQ (Khanna et al.,1975; Barry, 1977).

Most of the useful theory regarding anisotropic dielectric resonators has been dealt with by Barry. We will review some of it here and then describe some attempts to account for the observed length dependence of the frequency for a finite resonator using specialized and somewhat unphysical boundary conditions. We will then describe solutions for infinite dielectric wave guides with and without an outer conductor for the case of no azimuthal dependence and for a cosine azimuthal dependence of the fields. We will find that the field patterns for these models bear some relation to those for the two lowest observed modes in the dielectric resonance experiment. The mode

plots for the wave guide solutions do not provide an explanation for the observed similarity of the mode plots for the lowest coaxial and dielectric modes in the TTF-TCNQ crystals.

5.2 Open Circuit Boundary Conditions

The problem of the dielectric resonator is more complicated than that of a cavity with perfectly conducting walls because of the presence of evanescent fields outside of the dielectric resonator. The simplest way to deal with this problem is to ignore the fields outside. This treatment is justified by recognizing that the component of the electric displacement perpendicular to a boundary, $D_{\perp}$, must be continuous across that boundary. The ratio of the perpendicular electric fields inside and outside is then inversely proportional to the ratio of the dielectric constant. If the sample dielectric constant is large, the perpendicular component of E outside of the boundary will be small. This situation is summarized by the so-called magnetic wall boundary conditions

$$\vec{n} \times \vec{H} = \vec{0} \tag{5.1}$$

$$\vec{n} \cdot \vec{E} = 0 \tag{5.2}$$

which limit the fields at a boundary to $\vec{E}$ fields parallel to the boundary and $\vec{H}$ fields perpendicular to the boundary. As Jaworski (1978) has pointed out, however, such boundary condition are really only appropriate for higher modes for which the exact behaviour at the boundary is of less importance. Unfortunately, we shall see that for anisotropic rectangular

crystals, open circuit boundary conditions provide the only simple means of dealing with crystals of finite length.

Before applying the boundary conditions, we must find a solution for the fields in a crystal. Maxwell's equations for a magnetically isotropic dielectric,

(5.3) $$\vec{\nabla} \times \vec{E} = (i\omega\mu/c)\vec{H}$$

(5.4) $$\vec{\nabla} \times \vec{H} = -(i\omega/c)\underline{\underline{\epsilon}}\,\vec{E}$$

(5.5) $$\vec{\nabla} \cdot \underline{\underline{\epsilon}}\,\vec{E} = 0$$

(5.6) $$\vec{\nabla} \cdot \vec{H} = 0$$

can be combined to give a wave equation in $\vec{E}$,

(5.7) $$\nabla^2\vec{E} - \vec{\nabla}(\vec{\nabla} \cdot \vec{E}) + (\omega^2\mu/c^2)\,\underline{\underline{\epsilon}}\,\vec{E} = \vec{0}$$

We take our origin to be the centre of the crystal and recognize that we will be dealing with crystals in which the X dimension, c^*, will be very small so that we want a solution without a nodal plane perpendicular to X in E_y and E_z. A convenient solution to this wave equation is then

$$E_x = A_x \sin(k_x X)\sin(k_y Y)\sin(k_z Z)$$

(5.8a)
$$E_y = A_y \cos(k_x X)\cos(k_y Y)\sin(k_z Z)$$

$$E_z = A_z \cos(k_x X)\sin(k_y Y)\cos(k_z Z)$$

The corresponding magnetic field components are,

$$H_x = (-i/k_o)(A_z k_y - A_y k_z)\cos(k_x X)\cos(k_y Y)\cos(k_z Z)$$

(5.8b)
$$H_y = (-i/k_o)(A_x k_z + A_z k_x)\sin(k_x X)\sin(k_y Y)\cos(k_z Z)$$

$$H_z = (i/k_o)(A_y k_x + A_x k_y)\sin(k_x X)\cos(k_y Y)\sin(k_z Z)$$

where $k_o^2 = \omega^2/c^2$ and we have taken $\mu = 1$. We have chosen the solution for which E_z is an odd function of Y in anticipation of this being the symmetry of the lowest mode.

The open circuit boundary (OCB) conditions require that, for a resonator of X, Y, and Z dimensions given by c, a, and b, we have (see Fig. 26)

$$k_x = l\pi/c \qquad k_y = m\pi/a \qquad k_z = n\pi/b$$

where l is an even integer, and m and n are odd integers. Substituting for $\vec{E}$ in the wave equation, (5.7), gives rise to

three homogeneous equations for A_x, A_y, and A_z. For the case of a tetragonal dielectric tensor, with ϵ_z and $\epsilon_x = \epsilon_y = \epsilon_\perp$, there are non-trivial solutions for

$$\omega^2/c^2 = ((k_x^2+k_y^2)/\epsilon_z) + (k_z^2/\epsilon_\perp) \tag{5.9}$$

and

$$\omega^2/c^2 = (k_x^2+k_y^2+k_z^2)/\epsilon_\perp \tag{5.10}$$

If we use Eq. (5.9) to solve for A_x and A_y we find

$$\begin{aligned} A_x/A_z &= \epsilon_z k_z k_x/(k_x^2+k_y^2)\epsilon_\perp \\ A_y/A_z &= -\epsilon_z k_z k_y/(k_x^2+k_y^2)\epsilon_\perp \end{aligned} \tag{5.11}$$

so that $A_x k_y + A_y k_x = 0$ and $H_z = 0$. We will refer to this as the transverse magnetic (TM) mode. For this solution, k_z and k_y must be non-zero since E_y contains $\sin k_z Z$ and E_z contains $\sin k_y Y$. k_x may be 0.

If we use Eq. 5.10, we find that we can solve for A_z and obtain

$$A_z(k_x^2+k_y^2+k_z^2)((\epsilon_z/\epsilon_\perp)-1) = 0 \tag{5.12}$$

so that if $\epsilon_z \neq \epsilon_\perp$, we must have $E_z=0$. This will be referred to

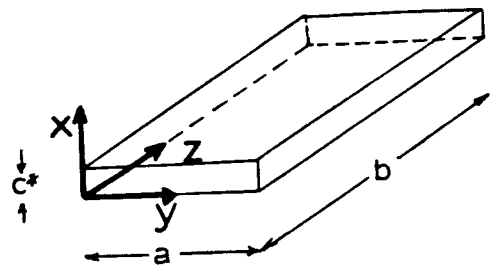

Figure 26. The labelling of the dimensions of TTF-TCNQ crystals.

as TE. For non-trivial solutions for this type of mode, we must have $k_x \neq 0$. Since c^* is very small, in cases of interest to us, the smallest non-zero k_x will be very large. It is thus unnecessary to consider this solution further.

We note, at this point, that for an isotropic resonator (i.e. $\epsilon_\perp = \epsilon_z$), Eqs. 5.9 and 5.10 would be equivalent. We would then be free to choose an axis along which to set the electric or magnetic fields to zero. In the present case, however, the anisotropy has split the T.E. and T.M. modes and we are not free to choose any axis . The anisotropy of the problem has defined the Z axis as the one to which the labels T.E. and T.M. are referred.

From Eq. 5.9, the frequencies for the magnetic wall solution are given by

$$f^2 = \frac{c^2}{4}\left\{\left[(l/c)^2 + (m/a)^2\right]/\epsilon_z + (n/b)^2/\epsilon_\perp\right\} \tag{5.13}$$

where l can be zero. The analysis for the even modes is identical so that Eq. 5.13 is appropriate for all integer values of m and n. Field lines for some of the lower lying modes appear in Fig. 27. In a model with more realistic boundary conditions, as we shall discuss below, the separation into T.E. and T.M. modes becomes less distinct. Barry (1977) used the notation $E^z_{\ell m}$ to denote dielectric resonances which, in the limit of large aspect ratio ($b>>a>>c^*$) would have electric fields

primarily along the Z axis. We will use this notation in a similar way with l and m giving the number of electric field minima in the Y and Z directions respectively. Each mode in Fig. 27, then, is labelled by the $E^{z}_{\ell m}$ mode which would reduce to that mode in the limit of magnetic wall boundary conditions.

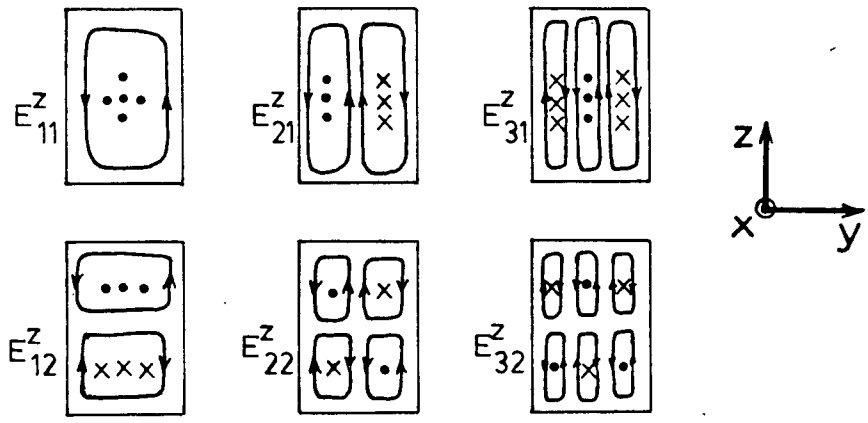

Figure 27. The field lines for some of the low lying dielectric resonances.

5.3 A Review of Results for Infinite Dielectric Resonators

Following Barry (1977), we go on to consider models in which the sample is infinite in the Z direction ($b=\infty, k_z = \pi/b=0$) and for which we can take some account of fields outside of the crystal.

Inside of the crystal, we will again use the plane wave solutions of Eqs. 5.8a and 5.8b. Because of the infinite length k_z is zero and the only spatial dependence will be in the X and Y directions. We will take this Y dependence to be $e^{ik_y y}$ for now and thus include both even and odd solutions. For these assumptions we obtain, for the fields,

$$E_x = E_y = H_z = 0$$

$$H_x = -k_y E_z / k_o \tag{5.14}$$

$$H_y = (-i/k_o)(\partial E_z / \partial x)$$

where E_z satisfies the wave equation

$$\nabla^2 E_z + k_o^2 \epsilon_z E_z = 0$$

and $k_o^2 = \omega^2/c^2$. The lowest mode will then have

$$E_z = A_{zi}\cos(k_{xi}X)\,e^{ik_yY}$$

(5.16)
$$H_x = (-k_y/k_o)A_{zi}\cos(k_{xi}X)\,e^{ik_yY}$$

$$H_y = (i/k_o)A_{zi}k_{xi}\sin(k_{xi}X)\,e^{ik_yY}$$

with Eq. 5.9 giving $(k_{xi}^2 + k_y^2)/\epsilon_z = k_o^2$.

We can then go on to deal with the fields outside of the crystal. We first consider the boundary perpendicular to X since c^* is the smallest dimension and OCB conditions are most deficient in describing the fields at this boundary. The fields outside of the X face boundary are assumed to decay exponentially giving,

$$E_z = A_{zo}e^{-k_{xo}(|X| - c^*/2)}\,e^{ik_yY}$$

(5.18)
$$H_x = -(k_y/k_o)A_{zo}e^{-k_{xo}(|X| - c^*/2)}\,e^{ik_yY}$$

$$H_y = (ik_{xo}/k_o)A_{zo}e^{-k_{xo}(|X| - c^*/2)}\,e^{ik_yY}$$

The wave equation applied outside of the crystal gives

(5.19)
$$k_o^2 = k_y^2 - k_{xo}^2$$

Boundary conditions at $|X| = c/2$ require the continuity of

all three fields. Eliminating A_{zo} and A_{zi} from the continuity equations leaves

(5.20) $$k_{xo} = k_{xi} \tan(k_{xi} c^*/2)$$

We now consider the Y dependence. If we just take $k_y = m\pi/a$, we have applied magnetic wall boundaries at Y= a/2. This is equivalent to an anisotropic slab for which the Y dimension is infinite and a wave length of 2a in the Y direction has been imposed.

Barry (1977) discusses this solution in detail. He shows that for $\epsilon_z >> 1$, so that k_o^2 is small relative to k_{xi}^2 and k_{yi}^2, one obtains

$$k_y^2 \approx k_{xi}^2 \tan((k_{xi} c^*)/2)$$

which, for $k_{xi} c^* << 1$, becomes

$$k_y \approx k_{xi}^2 c^*/2$$

Inserting this into Eq. 5.9 gives an explicit expression for the resonant frequency.

(5.24) $$\omega^2 = \frac{c^2}{\epsilon_z}\{k_y^2 + 2k_y/c^*\}$$

or putting $k_y = m\pi/a$,

$$f^2 = \frac{c^2}{4\epsilon_z}\{(m/a)^2 + 2m/ac^*\} \tag{5.24a}$$

Alternatively, one could apply exact boundary conditions on the face perpendicular to Y. In doing so, one is failing to satisfy the boundary conditions for the surfaces of the regions bounded by $|X|>c^*/2$, $|Y|>a/2$ as illustrated in Fig. 28.

We discuss such a model below. We note here that the solution to be discussed below is the one which has been used to analyse the dielectric resonance modeplots obtained experimentally.

We must also remember that we now have both even and odd dependence of the fields on Y. For even modes we have

$$E_{zi} = A_{zi}\cos(k_{xi}X)\cos(k_{yi}Y) \tag{5.25a}$$

inside the resonator and

$$E_z = A_{yo}\cos(k_{xi}X)e^{-k_{yo}(|Y| - a/2)} \tag{5.25b}$$

in the region bounded by $|Y|>a/2$; $|X|<c/2$. The wave equation outside the crystal gives

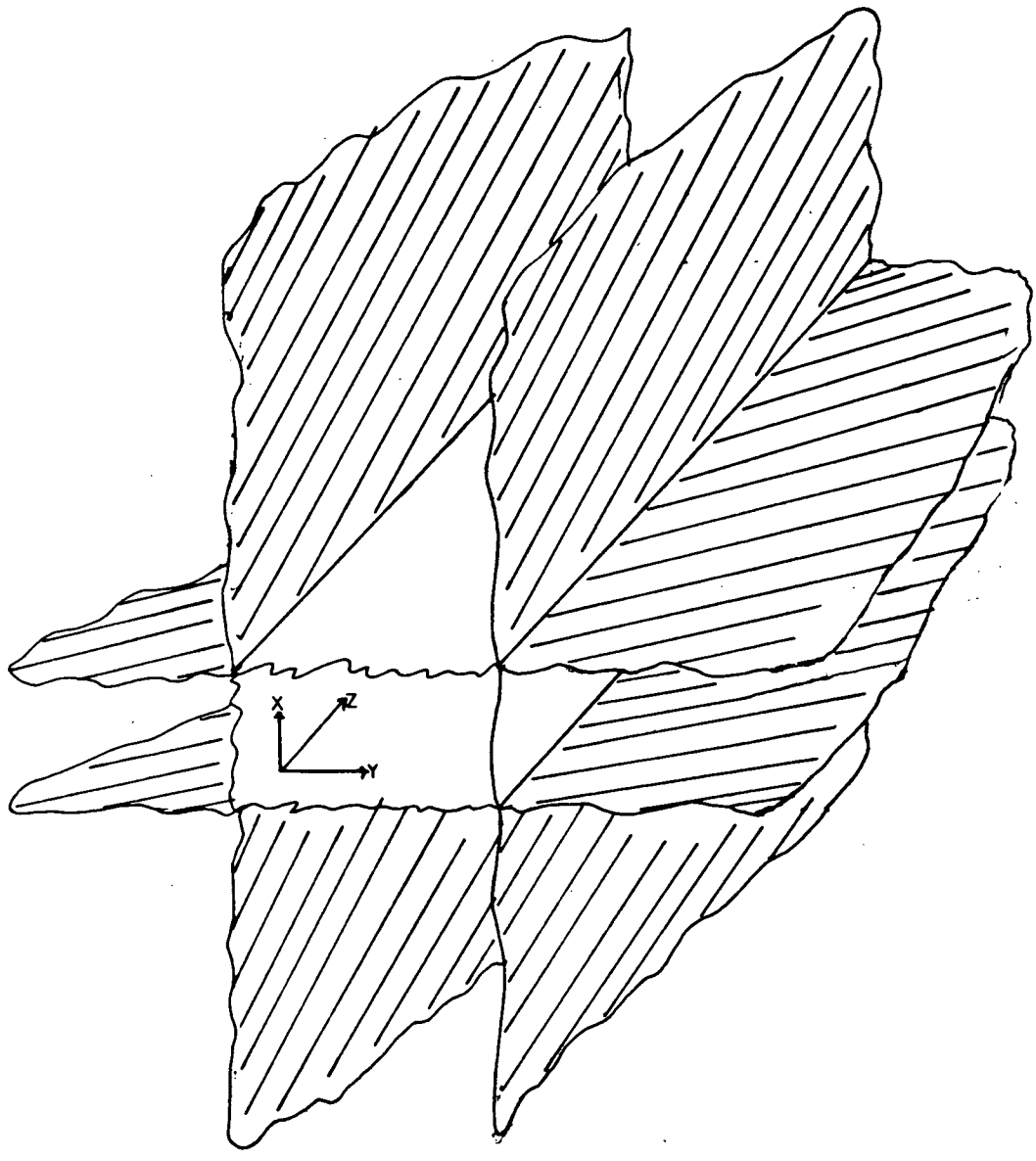

Figure 28. Surfaces on which boundary conditions are not satisfied in theory used for analysis of dielectric resonance data.

(5.26) $$k_o^2 = k_{yi}^2 - k_{yo}^2$$

and matching fields at $|Y| = a/2$ gives

(5.27) $$k_{yo} = k_{yi} \tan(k_{yi} a/2)$$

One can then use Eqs. 5.26 and 5.19 to eliminate k_{yo} and k_{xo} giving

(5.28a) $$k_{yi}^2 - k_o^2 = k_{xi}^2 \tan^2(k_{xi} c/2)$$

(5.28b) $$k_{xi}^2 - k_o^2 = k_{yi}^2 \tan^2(k_{yi} a/2)$$

For the odd dependence on Y we obtain

(5.29) $$E_z = A_{zi} \cos(k_{xi} X) \sin(k_{yi} Y)$$

inside and

(5.30) $$E_z = A_{yo} \cos(k_{xi} X) e^{-k_{yo}(|Y| - a/2)}$$

in the region bounded by $|Y| > a/2$; $|X| < c/2$. These lead to Eq. 5.28b being replaced by

(5.28c) $$k_{xi}^2 - k_o^2 = -k_{yi}^2 \cot(k_{yi} a/2).$$

In the analysis of the experimental dielectric resonance data, k_{xi} and k_{yi} have been obtained numerically from the crystal dimensions using the appropriate pair of Eqs. 5.28a and 5.28b or 5.28c. These values have then been used, with the observed resonant frequency contained in k_o^2, in

(5.17) $$\epsilon_z = (k_{xi}^2 + k_{yi}^2)/k_o^2$$

to yield a value for ϵ_z.

5.4 Other Models of Finite Resonators

As mentioned, the only model presented so far which was capable of dealing with finite resonators was the magnetic wall or OCB model. For this model, the length dependence of the squared frequency entered as $k_z^2/\epsilon_\perp$ where $k_z=n\pi/b$. The slopes of Barry's mode plots, however, gave a value for $\epsilon_\perp$ of about 2. This was considered to be too small. In addition, it was found that the dielectric modes had mode plot slopes almost identical to those of the lowest (coaxial) mode. The models to be discussed below were studied in the hope of accounting for these anomalies.

We will begin by considering, in section 5.4a, a model in which magnetic walls are applied to the X axis and extended beyond the crystal boundaries. In section 5.4b, we will consider a similar model with the "magnetic tube" parallel to the Z axis. In section 5.4c, we leave only the magnetic walls perpendicular to the X axis.

5.4a "Magnetic Tube" Parallel to X

Because of the finite length of the crystal, the Y component of the E field might be important in the region $|Z|>b/2$ and might be thought to be sampling a dielectric constant of 1 rather than $\epsilon_\perp$ thus leading to an increase in the slope of the mode plot (towards that of the coaxial mode). The departure of the slope from the expected slope for a coaxial mode might then be understood in terms of the finite size as well.

The first step in investigating finite resonator models was to attempt to extend the OCB model to include matching of fields on some boundaries in order to see if this resulted in a departure from the $1/\epsilon_\perp$ slope.

Jaworski (1978) suggested that it might be possible to apply a model originally proposed by Yee (1965) for circular cylindrical resonators. This model involves magnetic walls in the form of a cylindrical tube concentric with, and of the same radius as, the resonator. The modified model had magnetic wall boundaries on the faces perpendicular to Y and Z. These walls continued into the region $|X|>c^*/2$ as shown in Fig. 29. On the face perpendicular to the X axis, the fields inside are matched to exponentially decaying fields outside. The X dependence outside of the face perpendicular to the X axis goes as

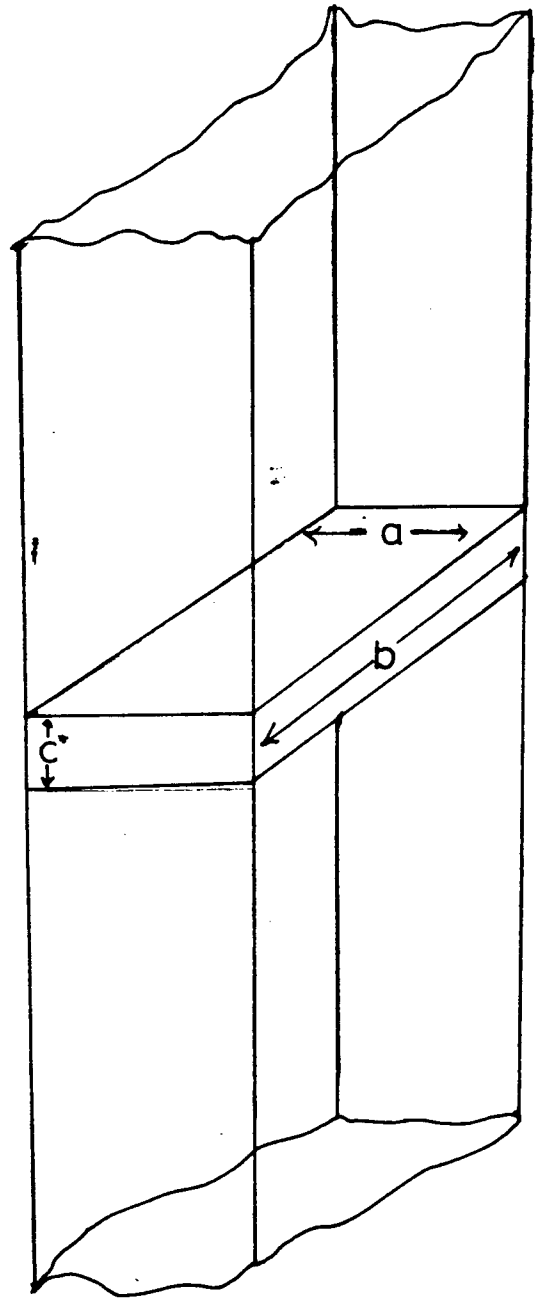

Figure 29. Magnetic walls as applied in adaptation of Yee's theory to rectangular crystals.

$$e^{-k_{xo}(|X|-c^*/2)} .$$

Application of Yee's result for an isotropic dielectric yields

(5.29a) $$k_{xo} = k_x \tan(k_x c/2)$$

with

(5.29b) $$k_o^2 = k_z^2 + k_y^2 - k_{xo}^2$$

In fact, as we shall see, this result is not appropriate for anisotropic dielectrics. We now analyse the problem in detail.

We begin by writing the fields inside and outside. Inside, we have,

$$E_{xi} = A_{xi} \sin(k_{xi} X)\sin(k_y Y)\sin(k_z Z)$$

(5.30) $$E_{yi} = A_{yi} \cos(k_{xi} X)\cos(k_y Y)\sin(k_z Z)$$

$$E_{zi} = A_{zi} \cos(k_{xi} X)\sin(k_y Y)\cos(k_z Z)$$

and

$$H_{xi} = (-i/k_o)\,(A_{zi}\, k_y - A_{yi}\, k_z)\cos(k_{xi}X)\cos(k_y Y)\cos(k_z Z)$$

(5.31) $$H_{yi}=(-i/k_o)(A_{xi}k_z+A_{zi}k_x)\sin(k_{xi}X)\sin(k_yY)\cos(k_zZ)$$

$$H_{zi}=(i/k_o)(A_{yi}k_x+A_{xi}k_y)\sin(k_{xi}X)\cos(k_yY)\sin(k_zZ)$$

which are the usual plane wave solutions. As before, the condition for a non-trivial solution with $H_z=0$ is Eq. 5.9.

Before going on to consider the fields outside the crystal, it is important to ask whether, for our choice of the TM mode, one can have a situation in which E_x can be zero and k_x be non-zero. In fact, if one chooses $A_{xi}=0$, one can obtain, from the wave equation, three equations in A_{yi} and A_{zi}.

$$A_{yi}k_yk_x+A_{zi}k_xk_z=0$$

(5.32) $$A_{yi}((\omega^2/c^2)\epsilon_\perp-k_x^2-k_z^2)+A_{zi}k_zk_y=0$$

$$A_{yi}k_yk_z+A_{zi}((\omega^2/c^2)\epsilon_z-k_x^2-k_y^2)=0$$

The condition for a non-trivial solution for A_{yi} and A_{zi} is found to be $k_{xi}=0$ or $\epsilon_\perp=\epsilon_z$. The second condition can be understood since, if $\epsilon_\perp=\epsilon_z$, our separation into TE and TM modes becomes arbitrary and one has the usual case for a metallic cavity in which one can assign a TE or TM mode. Since we are interested in $\epsilon_\perp\neq\epsilon_z$, we are forced to deal with a case in which E_x cannot be zero unless $k_x=0$. Since we are interested in the

spatial dependence along the X axis, we must accept E_x as being non-zero.

We can now write down the fields for $|X|>c/2$. They are given by,

$$E_{xo} = A_{xo}\, e^{-k_{xo}(|X| - c^*/2)} \sin(k_y Y)\sin(k_z Z)$$

$$E_{yo} = A_{yo}\, e^{-k_{xo}(|X| - c^*/2)} \cos(k_y Y)\sin(k_z Z) \qquad (5.33)$$

$$E_{zo} = A_{zo}\, e^{-k_{xo}(|X| - c^*/2)} \sin(k_y Y)\cos(k_z Z)$$

and

$$H_{xo} = (-i/k_o)\,(A_{zo} k_y - A_{yo} k_z)\, e^{-k_{xo}(|X| - c^*/2)} \cos(k_y Y)\cos(k_z Z)$$

$$H_{yo} = (-i/k_o)\,(A_{xo} k_z + A_{zo} k_{xo})\, e^{-k_{xo}(|X| - c^*/2)} \sin(k_y Y)\cos(k_z Z) \qquad (5.34)$$

$$H_{zo} = (i/k_o)\,(A_{yo} k_{xo} + A_{xo} k_y)\, e^{-k_{xo}(|X| - c^*/2)} \cos(k_y Y)\sin(k_z Z)$$

We now have 6 conditions at the crystal boundary $|X| = c^*/2$. These are

$$E_{yi} = E_{yo}\ ; \quad E_{zi} = E_{zo}\ ; \quad \epsilon_\perp E_{xi} = E_{xo}$$

and

$$H_{xi} = H_{xo}\ ; \quad H_{yi} = H_{yo}\ ; \quad H_{zi} = 0$$

giving

$$A_{yi}\cos(k_{xi}\,c^{*}/2)=A_{yo}$$

$$A_{zi}\cos(k_{xi}\,c^{*}/2)=A_{zo}$$

$$\epsilon_{\perp}A_{xi}\sin(k_{xi}\,c^{*}/2)=A_{xo}$$

(5.35)

$$(A_{zi}k_{y}-A_{y}k_{zi})\cos(k_{xi}\,c^{*}/2)=A_{zo}k_{y}-A_{yo}k_{z}$$

$$(A_{xi}k_{z}+A_{z}k_{xi})\sin(k_{xi}\,c^{*}/2)=(A_{xo}k_{z}+A_{zo}k_{xo})$$

$$(A_{yo}k_{xo}+A_{xo}k_{y})=0$$

Because of the relations between A_{xi} and A_{yi} and A_{zi}, as given by Eq. 5.11, some of these conditions are not independent. One ultimately arrives at two expressions for k_{xo}.

(5.36) $$k_{xo}=((k_{o}^{2}-k_{z}^{2})/(\epsilon_{\perp}k_{o}^{2}-k_{z}^{2}))\epsilon_{\perp}k_{xi}\tan(k_{xi}\,c^{*}/2)$$

(5.37) $$k_{xo}=\epsilon_{\perp}k_{xi}\tan(k_{xi}\,c^{*}/2)$$

These are obviously incompatible unless $\epsilon_{\perp}=1$, which is not an interesting solution, or $k_{xi}=k_{xo}=0$, or $\tan(k_{xi}\,c^{*}/2)=0$ which returns us to OCB conditions. We thus find that trying to apply

more realistic boundary conditions to the face perpendicular to the X axis cannot be done for the anisotropic situation. It can be easily shown that for the isotropic case, where A_{xi} can be zero while k_{xi} is non-zero, that Yee's result is obtained.

5.4b "Magnetic Tube" Parallel to Z

The situation is slightly different if we consider matching to decaying fields on the faces perpendicular to the Z and Y axes. The simplest way to proceed is to apply magnetic walls to all but the faces perpendicular to the Z axis. Outside of this face, we will consider the fields to decay as $e^{-k_{zo}(|z|-b/2)}$. We can anticipate the behaviour of such a model. The frequency will still be given by Eq. 5.9 and k_x and k_y will still be defined by the OCB conditions at the appropriate faces. By allowing the fields to extend into the region $|Z|>b/2$, we can only obtain a k_z that is smaller than its OCB value of $n\pi/b$. This, then, would be the kind of end effect which would give rise to an effective value for $\epsilon_\perp$ that was too large. When the boundary conditions are applied, k_{zo} is found to be given by

$$k_{zo}=(k_{zi}/\epsilon_\perp)\tan(k_{zi}b/2) \tag{5.38}$$

The characteristic equation outside of the crystal is

$$k_{xo}^2=k_{yi}^2+k_{xi}^2-k_o^2 \tag{5.39}$$

Using it to eliminate k_o^2 from Eq. 5.9 gives a second equation in k_{zo} and k_{zi}

(5.40) $$(k_x^2 + k_y^2)(\epsilon_z - 1)/\epsilon_z = k_{zo}^2 + k_{zi}^2/\epsilon_\perp$$

For a typical crystal, k_y^2 will be much larger than $k_{zi}^2/\epsilon_\perp$ with the result that k_{zo} will be large and k_{zi} will be slightly smaller than π/b. If one thinks of the end effect as an effective length, $b_{eff} = b + \Delta b$, then for $k_x = 0$ and $k_y = \pi/a$, numerical solutions using this model for a crystal of dimension a=0.05 cm, give Δb ranging from 0.05 cm, for b=1cm, to 0.06 cm for b=0.2cm. A small constant Δb would appear in the observed $\epsilon_\perp$ as

$$\epsilon_{\perp obs} = \epsilon_\perp (1 + (\Delta b/b)) .$$

5.4c Magnetic Walls Perpendicular to X

One can extend this model to one in which the magnetic walls are placed only on faces perpendicular to the X axis. When we assume exponential decay beyond both the Z and Y faces, we obtain, as for the previous model, Eq. 5.38 for the relation between k_{zo} and k_z as well as a similar condition

(5.41) $$k_{yo} = (k_{yi}/\epsilon_z)\tan(k_{yi}a/2)$$

The characteristic equations outside of the crystal are Eq. 5.39 and

(5.42) $$k_{yo}^2 = k_z^2 + k_x^2 - k_o^2$$

Eliminating k_o, k_{yo}, and k_{zo}, and taking $k_x = 0$, leads to two equations in k_{zi} and k_{yi}.

(5.43) $$(k_{zi}/k_{yi})^2 \epsilon_z^2((\epsilon_\perp - 1)/\epsilon_\perp) - \epsilon_z = \tan^2(k_{yi}a/2)$$

(5.44) $$(k_{yi}/k_{zi})^2 \epsilon_\perp^2((\epsilon_z - 1)/\epsilon_z) - \epsilon_\perp = \tan^2(k_{zi}b/2)$$

This model, unfortunately, just gives an effect similar to that found previously. For a crystal with a=0.05 cm and taking ϵ_z=3000 and $\epsilon_\perp$=5, this model would yield a mode plot from which

an inverse slope of about 5.14 would be obtained. This is greater than $\epsilon_\perp$.

It was generally found, then, that using simple models, which try to match plane wave solutions inside the crystal to decaying fields at the faces without matching the fields in the corner regions, to analyse mode plot slopes would give values of $\epsilon_\perp$ which were lower than the inverse slope. They are thus unable to account for the low observed values of the inverse slope.

5.5 Infinite Waveguides With and Without Outer Conductor

The observed similarity of coaxial and dielectric mode plot slopes suggests that one should consider the effect of an outer conductor, i.e. the wave guide, on the dielectric resonances. In this section we compare dielectric wave guides with and without a metallic outer conductor for the two lowest azimuthal dependences of the modes.

5.5a n=0 Azimuthal Dependence

Barry (1977) disscusses the case for an infinite cylindrical rod of radius R_1 in a circular metallic waveguide of radius R_2 for $\epsilon_x = \epsilon_y = \epsilon_\perp$. His solutions are reviewed in Appendix 2. The solutions can be classified by the azimuthal dependence of the fields where this is given by $e^{in\phi}$. Barry has calculated the solutions for the n=0 cases. Some examples of calculated n=0 mode plots appear in Figs. 30 and 31. In Fig. 30a, we have shown, for a wave guide with and without an outer conductor, the solution for $\epsilon_\perp=5$, $\epsilon_z=3000$ and an R_1 giving a cross-sectional area typical of the crystals studied. In Fig. 30b, we have shown the mode for an inner core identical to the wave guide of Fig. 30a and an outer conductor with a cross-sectional area similar to that of wave guides used in the experiments. Also shown are the lines along which $k_1^2=0$ and $k_2^2=0$. For $k_2^2<0$, which is the region to the right of the $k_2^2=0$ line, the fields die off outside of the dielectric. The solutions are seen to be similar for both the dielectric waveguide with and without an outer conductor. In Fig. 30b, the section of the lowest mode labelled 1a to 1b is one in which much of the field is outside of the dielectric. As we go to higher frequencies, the fields are increasingly contained inside the dielectric. At 1b, where $k_2^2=0$, there is a node in E_z at the surface of the dielectric. The variation of the amplitude of E_z

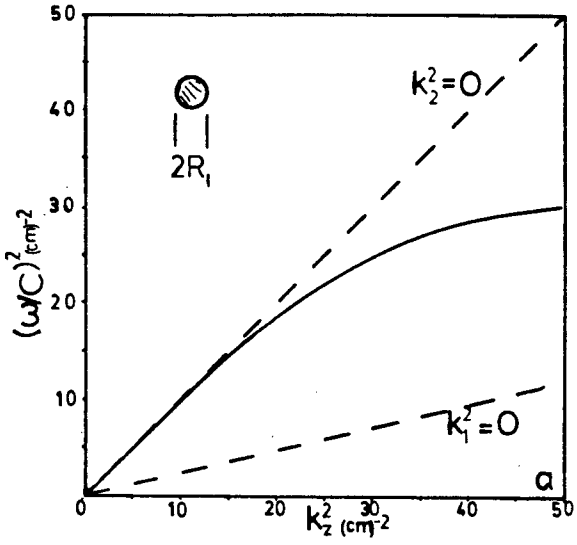

Figure 30a. n=0 dielectric wave guide mode plot for R_1=0.015 cm, $\epsilon_\perp$=5, ϵ_z=3000. (no outer conductor)

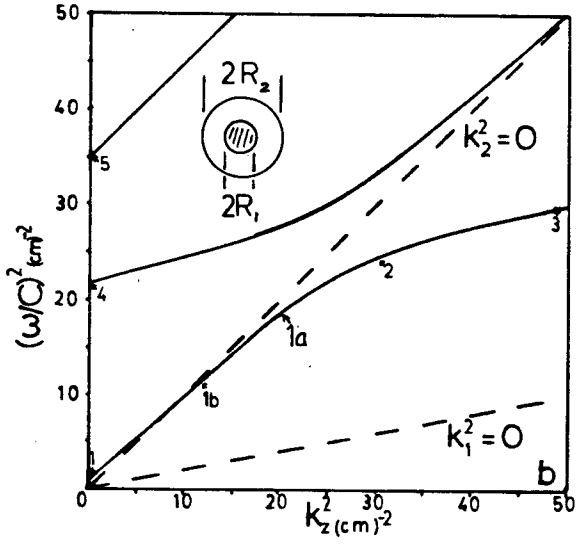

Figure 30b. n=0 dielectric wave guide mode plot for R_1=0.015 cm, R_2=0.500 cm, $\epsilon_\perp$=5, ϵ_z=3000. (outer conductor present)

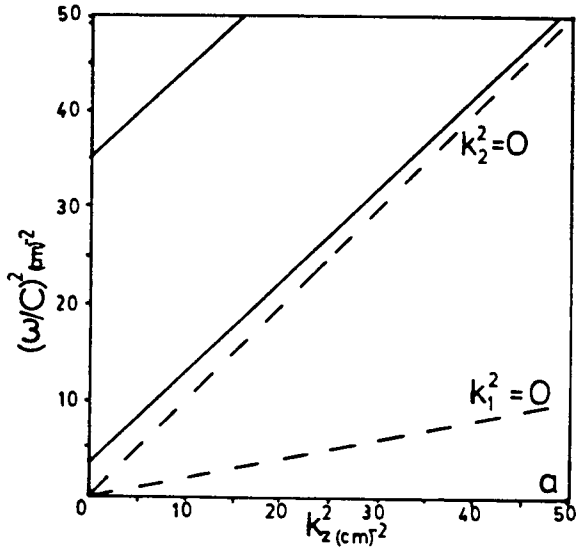

Figure 31a. n=0 dielectric wave guide mode plot for R_1=0.015 cm, R_2=0.5 cm, $\epsilon_\perp$=5, ϵ_z=600. (outer conductor present)

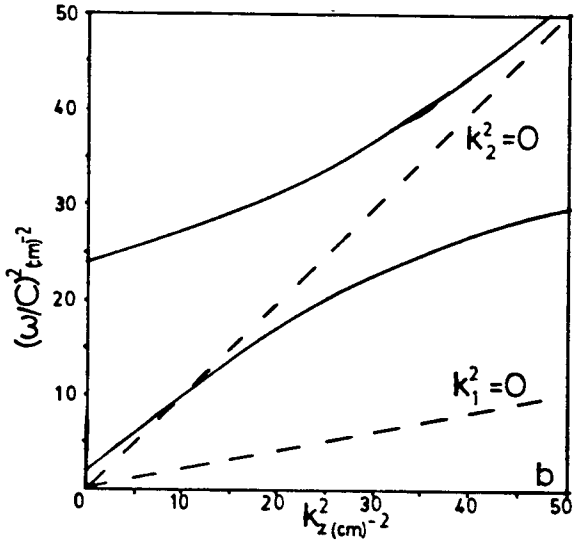

Figure 31b. n=0 dielectric wave guide mode plot for R_1=0.015 cm, R_2=0.05 cm, $\epsilon_\perp$=5, ϵ_z=3000. (outer conductor present)

across a diameter, for each of the labelled points, is shown qualitatively in Fig. 32. At 2, the fields have drawn into the dielectric so that there is a cylindrical nodal surface at $r \approx 0.01$ cm. k_1^2 is approximately constant along 4, 2, 3 and the mode plot has a slope of about $1/\epsilon_\perp$. This is predominantly a dielectric mode but is not of experimental interest because the small c^* dimension would push modes with cylindrical nodal surfaces to very high frequency. A pure coaxial mode with a metallic centre conductor would follow the $k_2^2=0$ line and have a propagation velocity of c. The 1,1b,1a part of the lowest mode is predominantly coaxial but does depend on the properties of the dielectic core as discussed by Barry and illustrated below. Fig. 31a shows the result for $\epsilon_z=600$. The intercept of the lowest mode has risen although not by a factor of 5 as would be expected for a purely dielectric mode. The slope has increased to 0.95.

The effect of decreasing R_2/R_1 is shown in Fig. 31b which illustrates the case for $R_2=0.05$ cm. The separation of the dielectric and coaxial modes is now less distinct.

The section of the lowest mode, 1a to 1b, in Fig. 30b, is analogous to the A mode observed by Barry. This implies that for long crystals, the coaxial A mode plot should have a slope of about 90% of that expected for a purely coaxial mode.

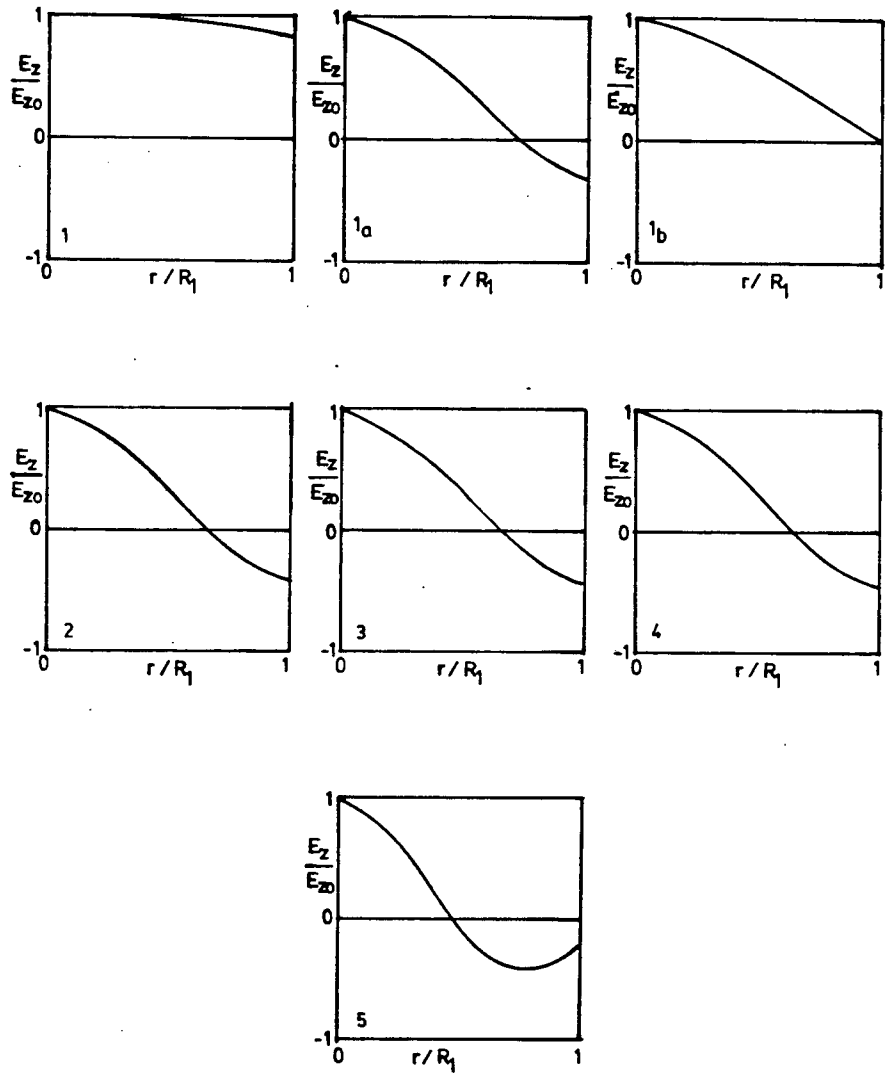

Figure 32. Qualitative depiction of the variation of E_z across the dielectric rod diameter for selected points on mode plot of Figure 30b.

5.5b n=1 Azimuthal Dependence

To check the effect of the outer conductor on a dielectric mode, such as the B mode, mode plots were calculated for the n=1 wave guide with and without an outer conductor. The problem without the outer conductor has also been dealt with by Jaworski (1978). Here there is a nodal plane across which E_z changes sign so that, for its lowest radial dependence, this mode is analogous to the B mode. The higher radial modes are not of interest since they are again pushed to very high frequency for a flat crystal such as was used.

The derivation of the characteristic equation for the n=1 case appears in Appendix 2. The calculated mode plots for the n=1 dielectric wave guide with and without an outer conductor with the same parameters as in Fig. 30a and Fig. 30b appear in Figs. 33a and 33b.

We again see that the regions $k_2^2<0$ are similar. In the case with an outer conductor, we find modes with constant k_1^2 and modes with constant k_1^2. The modes with constant k_2^2 can be identified as the lowest wave guide modes in a cylindrical metal tube of radius R_2. The modes with constant k_1^2 have a slope close to $1/\epsilon_\perp$ and are identified as dielectric modes. Fig. 34 shows the radial dependence of E_z across a diameter for the point 1 on the mode plot of Fig. 33b. This is roughly analogous

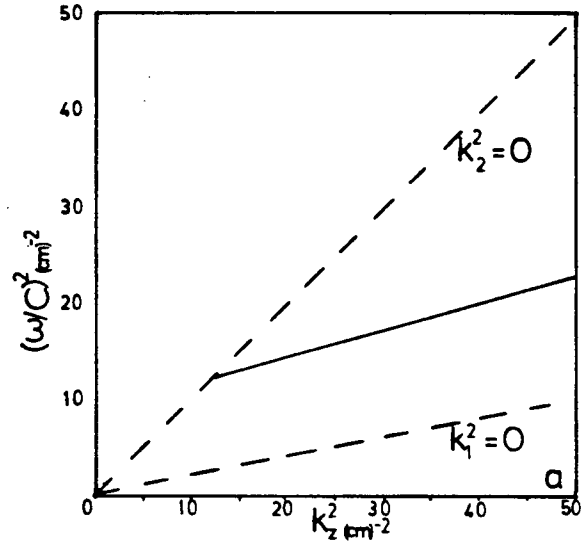

Figure 33a. n=1 dielectric wave guide mode plot for R_1=0.015 cm, $\epsilon_\perp$=5, ϵ_z=3000 (no outer conductor)

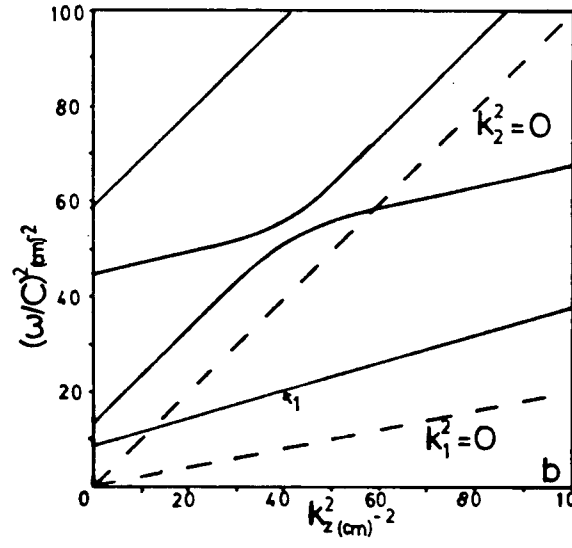

Figure 33b. n=1 dielectric wave guide mode plot for R_1=0.015 cm, R_2=0.500 cm, $\epsilon_\perp$=5, ϵ_z=3000. (outer conductor present)

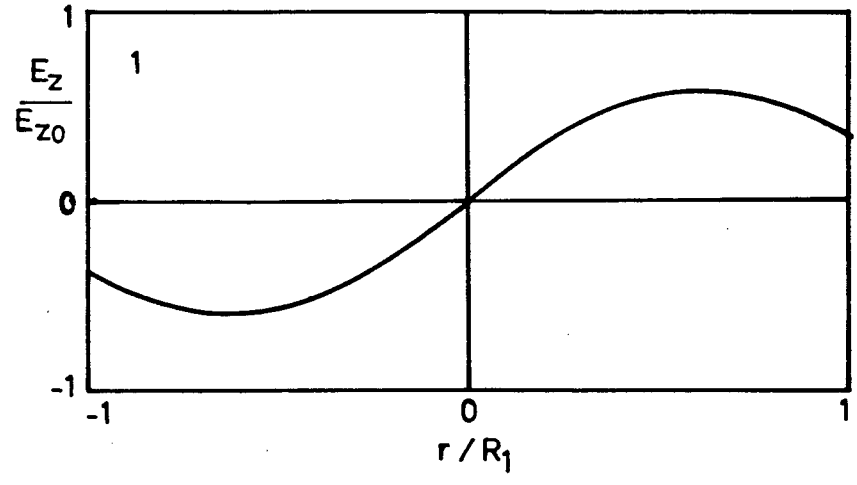

Figure 34. Qualitative depiction of the variation in magnitude of E_z across the diameter of the dielectric rod for point 1 on Fig. 33b.

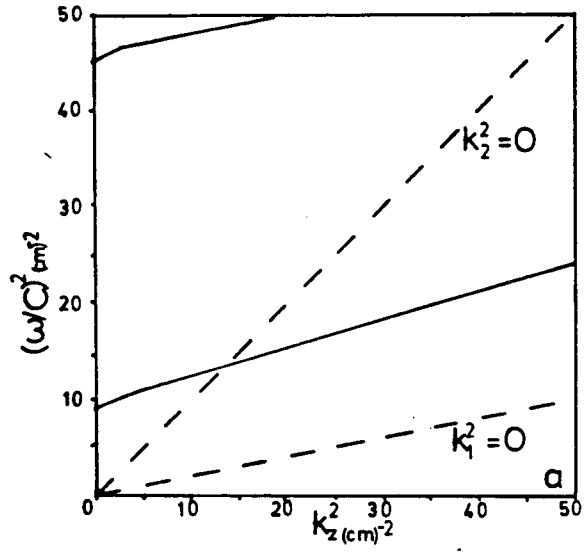

Figure 35a. n=1 dielectric wave guide mode plot for R_1 =0.015 cm, R_2=0.05 cm, $\epsilon_\perp$=5, ϵ_z=3000. (outer conductor present)

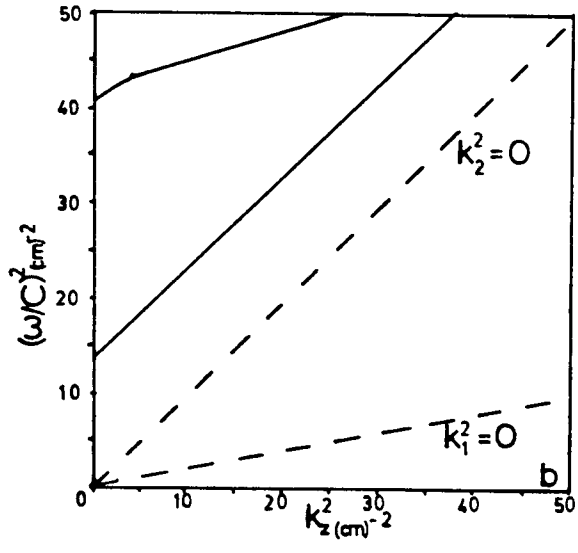

Figure 35b. n=1 dielectric wave guide mode plot for R_1=0.015 cm, R_2=0.500 cm, $\epsilon_\perp$=5, ϵ_z=600. (outer conductor present)

to the B mode. The dielectric and waveguide modes repel each other but the are otherwise independent. This is illustrated in Figs. 35a and 35b. In Fig. 35a, R_2 has been decreased by a factor of 10. The waveguide modes have risen out of the range shown, but the dielectric modes are unaffected. In Fig. 35b, ϵ_z has been decreased by a factor of 5 and the intercept of the lowest dielectric mode has risen by this amount leaving the wave guide mode unaffected. The implication is that, other than for a crossing of the wave guide mode, the dielectric mode, in the absence of end effects, should not be strongly affected by the presence of the outer conductor.

The fact that the coaxial and dielectric modeplots are parallel in Barry's work cannot be attributed just to the effect of the outer conductor on the dielectric modes. It is also apparent that the slope of the A mode cannot be entirely attributed to the fact that the core of the coaxial resonator is a dielectric. We expect that these anomalies have to be attributed to end effects of some sort and have tested this by trying to measure dielectric resonances in long crystals for which end effects are of less importance. The results are discussed in the next chapter.

CHAPTER VI

Results and Discussion of Dielectric Measurements on TTF-TCNQ

6.1 The Mode Plots

As has been discussed, the real parts of the dielectric constant for the b direction can be obtained from a plot of the squares of the resonance frequencies versus the inverse squared lengths of the crystal as it is cut. For a hypothetical crystal obeying the open circuit boundary conditions, this would correspond to plotting f^2 versus k_z^2 for the lowest set of modes. Extrapolating to the ordinate axis should then give, using the characteristic equation, 5.9,

$$f_{\parallel}^2 = (k_x^2+k_y^2)(c^2/4\pi^2)/\epsilon_b'$$

The most useful model for extracting ϵ_b' is the infinite resonator with the boundary conditions satisfied on the four faces but not in the edge regions. This model uses Eqs. 5.28a, 5.28b, or 5.28c to yield k_{xi}^2 and k_{yi}^2. The slope is normally dealt with by assuming $k_z = (m\pi/b)$ so that the slope becomes $(c^2/m^2\epsilon_q')$.

Barry (1977) dealt with four modes in detail. The B, C, and D modes were the three lowest dielectric modes with 0, 1,

and 2 electric field nodal planes perpendicular to the Y axis. In the E^z_{lm} notation, these are referred to as E^z_{11}, E^z_{12}, and E^z_{13} respectively. In the present work, crystals approaching 1 cm in length have been used to observe modes with $l=1$; $1 \leqslant m \leqslant 5$, $l=2$; $1 \leqslant m \leqslant 3$, and $l=3$; $m=1$. As will be described below, the importance of end effects appears to diminish for the higher modes.

It has also been found that the identity of the coaxial mode can be confirmed by comparing the A mode in long crystals with the coaxial mode observed using copper replicas of these crystals.

We will first consider some of the results concerning the A mode.

6.1a The A Mode

Seven crystals were analysed in detail. Some of the mode plots appear in Appendix 3. It can be seen that the A mode for crystals 4, 9, 10, and 12 does not yield a straight line. The A mode plot, for crystal 4 particularly, deviates toward the origin for large b. This suggests that the coaxial dielectric transmission line solution might be appropriate in the long crystal limit.

In order to study the effect of the finite crystal length, copper replicas of some of the crystals were made and mode plots for purely coaxial modes obtained. The dimensions of the copper replicas appear in Table 3. The mode plots appear in Fig. 36. Replica C5 was mounted with the quartz fibre perpendicular to the replica and attached at the centre of the replica in order to study the coaxial resonance in the absence of glue at the ends. Unfortunately, the positioning of replica C5 was imprecise using this mount, and the significance of the results obtained was uncertain. The effect of the mounting epoxy on the resonances will be discussed below.

Also shown in Fig. 36 is the A mode for crystal 4. It can be seen that the A mode has a length dependence similar to the coaxial modes and that, for large b, both types approach the line given by $f^2=c^2/(4b^2)$. On the basis of the dielectric transmission line calculations, one would expect the limiting

TABLE 3

Dimensions of copper replicas used for coaxial mode studies

Replica	a (cm)	c (cm)
C1	0.049	0.0035
C2	0.042	0.007
C3	0.040	0.007
C4	diameter = 0.019 cm	

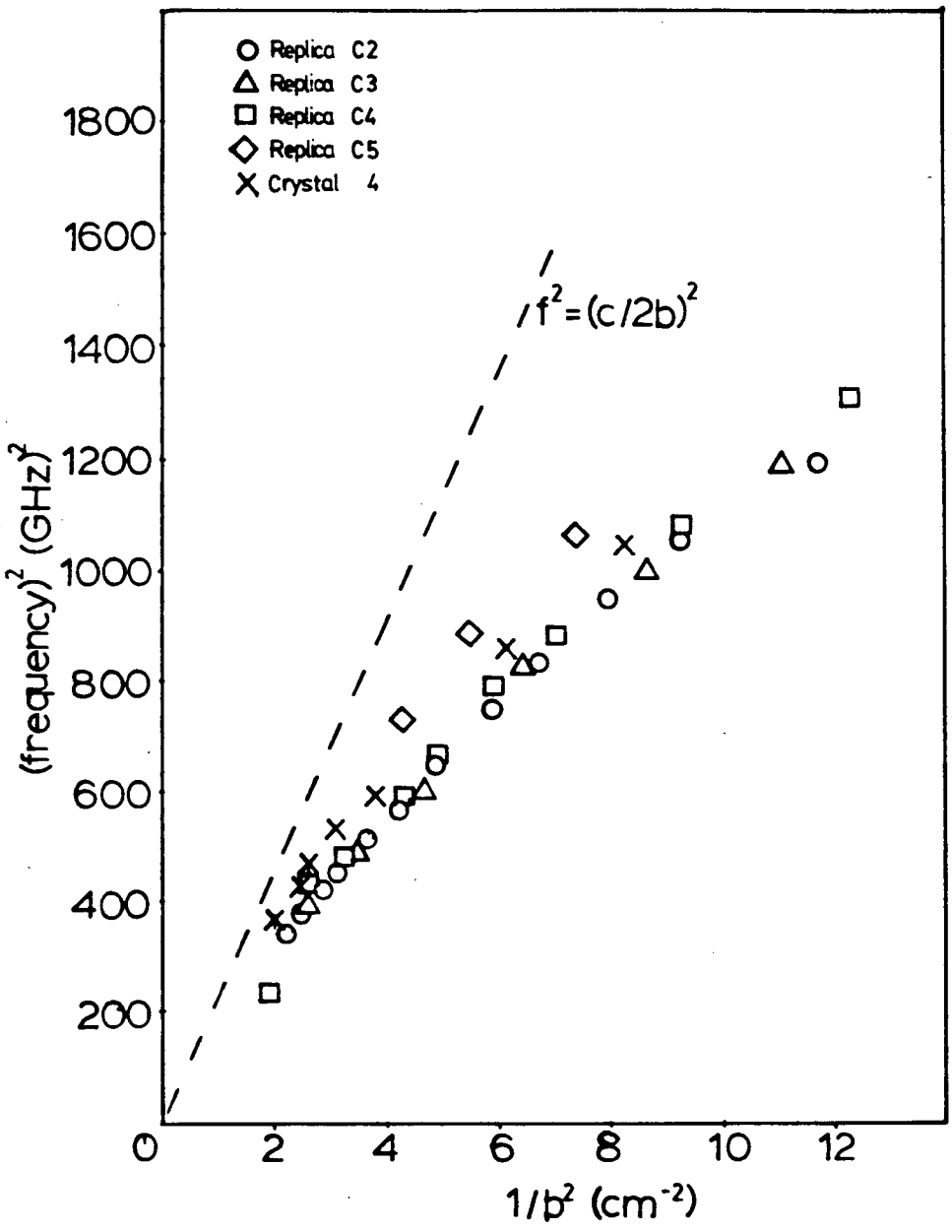

Figure 36. Mode plots for copper replicas in study of coaxial modes.

slope of the A mode to be about 90% of that for the purely coaxial mode. The crystals studied were not long enough to test this point.

The deviation of the purely coaxial mode from $f^2=c^2/(4b^2)$ can be represented by a model in which b is replaced by $(b+\Delta)$. For replicas 2, 3, and 4, Δ was found to be $(0.13\pm.01)$ cm. That Δ is constant implies that, in the range of lengths studied, the fields at the end of the crystal are affected by the presence of the boundaries and not, directly, by the length of the crystal.

The behaviour of the A mode is thus found to be consistent with that for a coaxial mode. The deviation from a slope of about $c^2/4$ is not intrinsic to TTF-TCNQ but is likely just a characteristic of the coaxial mode in a resonator with end effects.

6.1b The Dielectric Mode Plots

The initial results, such as those displayed in the mode plots for crystals 4, 9, and 12, seemed to confirm that the dielectric modes B, C, and D, did give straight line mode plots with a slope similar to that of the A mode plot. It was, however, possible to carry out detailed studies using 2 crystals, 18 and 19, with large enough a and initial b dimensions to observe a number of higher modes as well as resonances for lower modes low values of $k_z = \pi/b$. The mode plots for all of these crystals appear in Appendix 3. These results were obtained at 5K.

For crystal 18, it was possible to observe E^z_{lm} resonances for $l=1$; $1 \leq m \leq 5$ and $l=2$; $m=1$. A third type of resonance, labelled B_x on the mode plot, will be discussed below. With the exception of B_x, crystal 19 displayed all of the above modes plus $l=2$; $m=2$ and $m=3$ and $l=3$; $m=1$. The m values for the higher l modes are determined by noting that the frequency becomes independent of l as k_z goes to zero. The most striking feature of the mode plot for crystal 18 is the fact that, for the higher modes in particular, the slope appears to decrease for smaller values of 1/b . At higher values of 1/b , the $l=1$ mode plots all seem to be parallel to that for the A mode. Crystal 19, unfortunately, broke before the short crystal behaviour could be confirmed but it also showed the tendency for

higher modes to approach the ordinate axis with smaller slopes.

Table 4 shows the values of ϵ_q' calculated from each of the dielectric modes assuming that the limiting slope for $1/b \rightarrow 0$ is given by $c^2 l^2/(4\epsilon_q')$. It can be seen that, for a given value of l, the derived value of ϵ_q' increases with increasing m. This trend can be rationalized by arguing that k_z^2 approaches $l^2\pi^2/(4b^2)$ only if the fields in the crystal approach the limit in which they approximate the open circuit boundary condition solutions. For each dimension, this limit can be approached in two ways. For a given mode, the propagation constant in a given direction will go to zero as that dimension gets large. This is the situation as we approach large values of b. Alternatively, if one takes a given crystal, the true propagation constant and the OCB solution in a given direction will tend to approach each other for increasing mode indices in that direction. It is not immediately obvious that a better approximation of k_y to the OCB solution should improve the agreement between k_z and its OCB value. It was, however, found, as discussed in chapter 4, that situations in which OCB conditions were applied to the face perpendicular to Y yielded solutions for which k_z also approximated the OCB condition solution. An obvious problem is then presented by the results for crystal 19 where, for corresponding m values, ϵ_q' is found to be smaller for l=2 than for l=1. This is not understood at present. Within the l=2 modes, however, the trend for increasing m is still observed.

TABLE 4

Values of ϵ_a' obtained from dielectric resonance studies for TTF-TCNQ

crystal	mode (E^z_{lm})		ϵ_a'
	l	m	
18	1	1	2.3
18	1	2	3.5
18	1	3	4.7
18	1	4	5.6
18	1	5	9.0
19	1	1	2.0
19	1	2	3.5
19	1	3	5.6
19	1	4	6.1
19	1	5	7.5
19	2	1	2.0
19	2	2	2.5
19	2	3	3.0
19	3	1	3.7

It would appear, then, that one should obtain a lower limit for ϵ_a' by using long crystals and higher modes. The values of ϵ_a' obtained for the modes observed in this work do not seem to be approaching an upper limit. On this basis, the actual value is expected to be greater than 9.

With the observation that the limiting mode plot slope for long crystals is not equal to the slope at shorter lengths, it is clear that the extrapolation back to the ordinate axis to obtain ϵ_b' must be approached cautiously. The best values of will likely be obtained by extrapolating those mode plots giving the highest values of ϵ_a'.

For given values of a and c^*, the values of k_{xi}^2 and k_{yi}^2 obtained using Eqs. 5.28a, 5.28b, and 5.28c, are largely insensitive to k_o^2. The value of ϵ_b' obtained is thus inversely proportional to the k_o^2 used. As it is clear that, for the lower modes, the value of k_o^2 obtained is a lower limit, the ϵ_b' obtained should be an upper limit.

The largest source of uncertainty in estimating ϵ_b' lies in the measurement of c^* and the fact that it may not be constant over the whole crystal. c^* is typically about 5×10^{-3} cm and can be measured to about $\pm 10^{-3}$ cm. This results in an error in ϵ_b' of about 10%.

Fig. 37 shows values of ϵ_b' for several crystals plotted against $f_{\parallel}$ where $f_{\parallel}$ is the square root of the mode plot

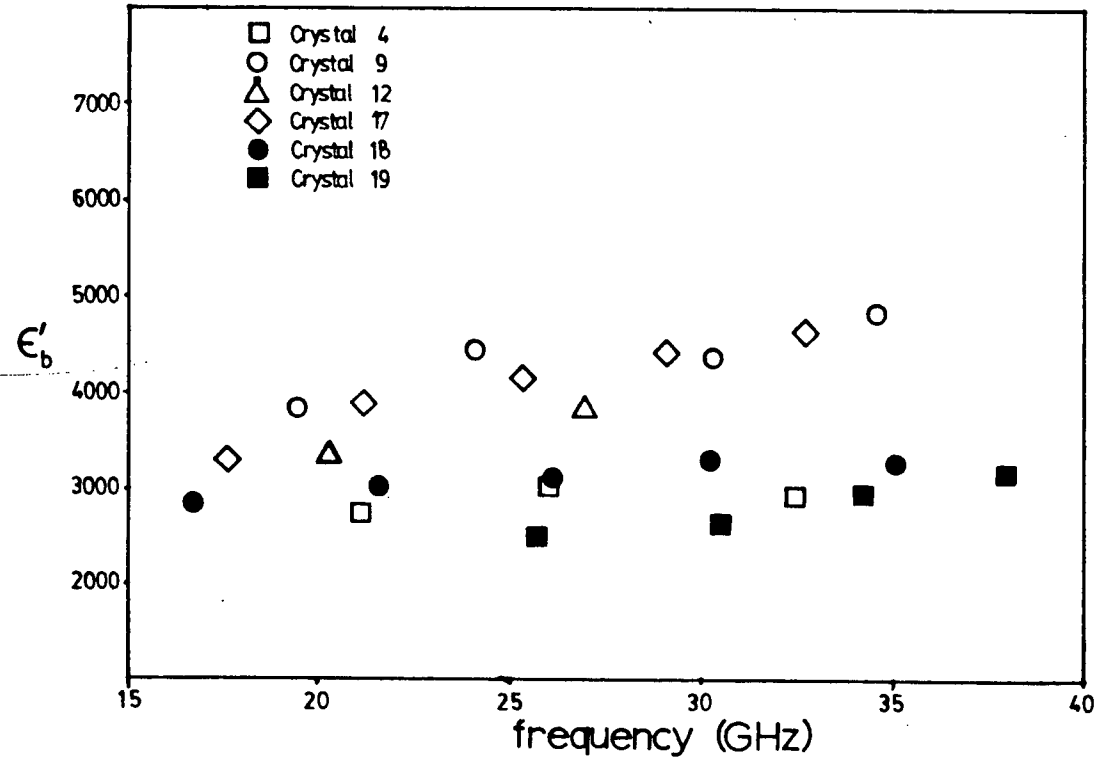

Figure 37. ϵ'_b plotted against f_{fl} for several TTF-TCNQ crystals studied

intercept for each mode. Crystals 18 and 19 are represented by solid symbols. The other crystals, because of the systematic error in the slope, are expected to give upper limits to ϵ_b'. They do, in fact, give higher values. On the basis of the results for crystals 18 and 19, it would appear that there is little frequency dependence in ϵ_b' from 15 GHz to 40GHz. The lower frequency values are again, however, less accurate and should be taken as upper limits so that the lack of frequency dependence may be a result of the systematic error in the slope as discussed above. Setting this aside, we obtain $\epsilon_b' = (3.0 \pm 0.4) \times 10^3$. It should be noted that there are some erratic results. The B mode for crystal 19, for example, gives an anomalously high value for ϵ_b'. It is possible that such anomalies arise because of the fact that some modes may be more sensitive than others to macroscopic imperfections at a particular point on the crystal.

It is interesting to compare the frequency dependence of the observed ϵ_b' with that predicted for a pinned charge density wave as given by Eq. 1.10. The real part of $\epsilon(\omega)$ is then given by

$$\epsilon'(\omega) = \epsilon^{sp} + \frac{(\epsilon(0) - \epsilon^{sp})\,\omega_o^2(\omega_o^2 - \omega^2)}{(\omega_o^2 - \omega^2)^2 + \Gamma^2\omega^2} \tag{6.1}$$

This model predicts a change in ϵ_b' of about 260 in going from 20GHz to 40GHz if one uses the parameters given by Eldridge and

Bates (1979) with $\epsilon'(0)$ adjusted to give $\epsilon'(20\ \text{GHz})=3000$. While this is not inconsistent with the observed weak frequency dependence, the range of frequencies covered is too small to attach much significance to the comparison.

Before leaving the mode plots, it is interesting to consider two other points briefly. As has been mentioned, crystal 18 displayed a mode, labelled B_X, with an anomalously small slope. This has tentatively been identified as a mode, analogous to the B mode, in which the relationships of the fields to the X and Y axes are reversed. This identification is supported by the observation that the maximum coupling angle for B_X and D differ by $\pi/2$. Using this identification, it is found that the intercept corresponds to $\epsilon_b'=4177$. This indicates, at least, that the appearance of such a mode in this frequency range may not be unreasonable for a crystal of this size. There are two possible sources for the very small slope. The fact that there is a component of π orbital overlap in the c* direction and not in the a direction suggests that ϵ_c' could be considerably larger than ϵ_a'. It is also possible that such a mode, with the electric field forming a loop perpendicular to the Y direction, could have very different end effects from those encountered for the B mode. The lack of understanding of end effects for this mode limits the information that can be extracted from it at this time.

The other interesting result involves modes with l=2. It

can be seen, in the mode plot for crystals 18 and 19, that some of these modes appear as doublets. It was found that the separation of the two resonances is not constant as the crystal is shortened. As the crystal is further shortened, however, one seems to lose a clear indication of a double resonance. The doubling phenomenon was studied in some detail for the E_{21}^{z} mode in crystal 19. A sequence showing how the two resonances couple as a function of the distance of the crystal centre from the short appears in Fig. 38. It can be seen that there are positions for which both resonances can be coupled. Maximum coupling for the lower resonance is at about 9.4 mm from the short while the higher one couples at about 5.4 mm from the short. The rotational dependence is the same for both resonances.

The origin of the double resonances remains somewhat of a mystery. There is no difficulty in accepting that a strongly coupled resonance can have a frequency which depends on the position in the guide . It is more difficult to understand how a resonance could couple at two different frequencies for a single position of the crystal. A possible clue is illustrated in Fig. 39 where the crystal, at the two maximum coupling positions, is superimposed on a diagram representing the standing wave out to 1 guide wave length from the short. If the identification of this mode as E_{21}^{z} is correct, we can think of the E_z and E_y fields as forming two loops as shown. Because the

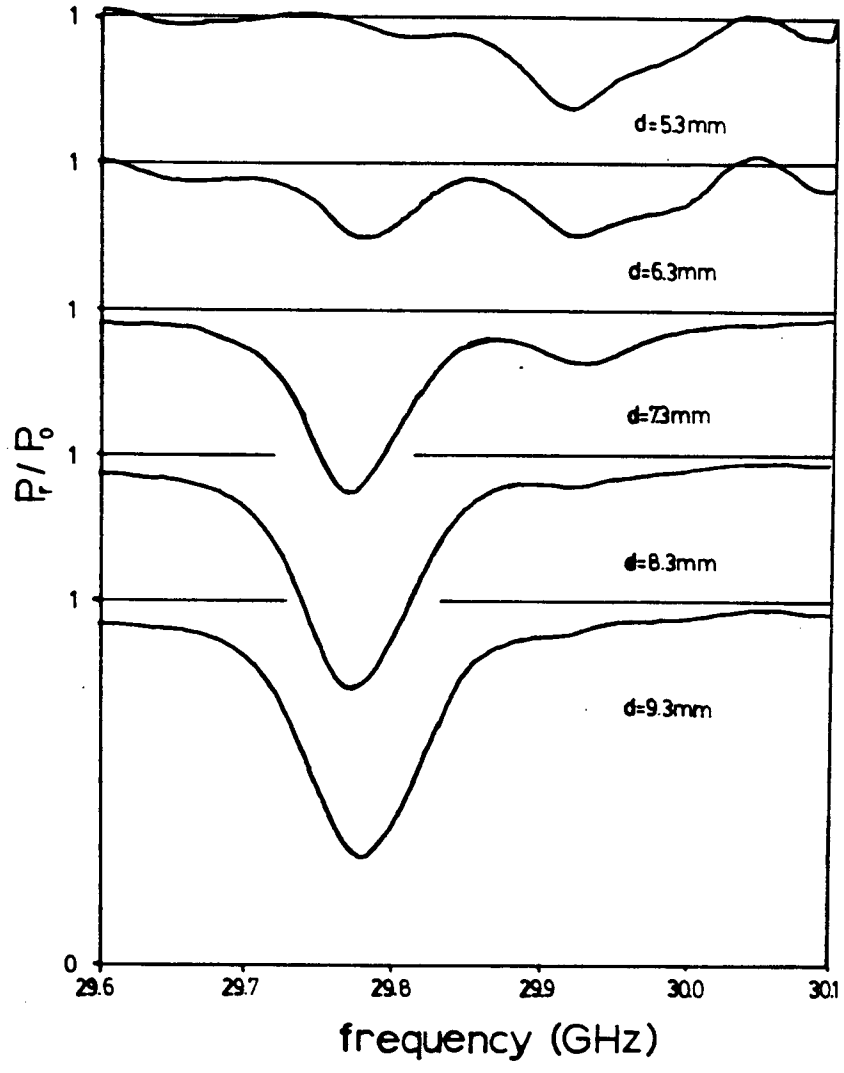

Figure 38. Coupling of the double dielectric resonance in crystal 19 at several distances of the crystal centre from the short.

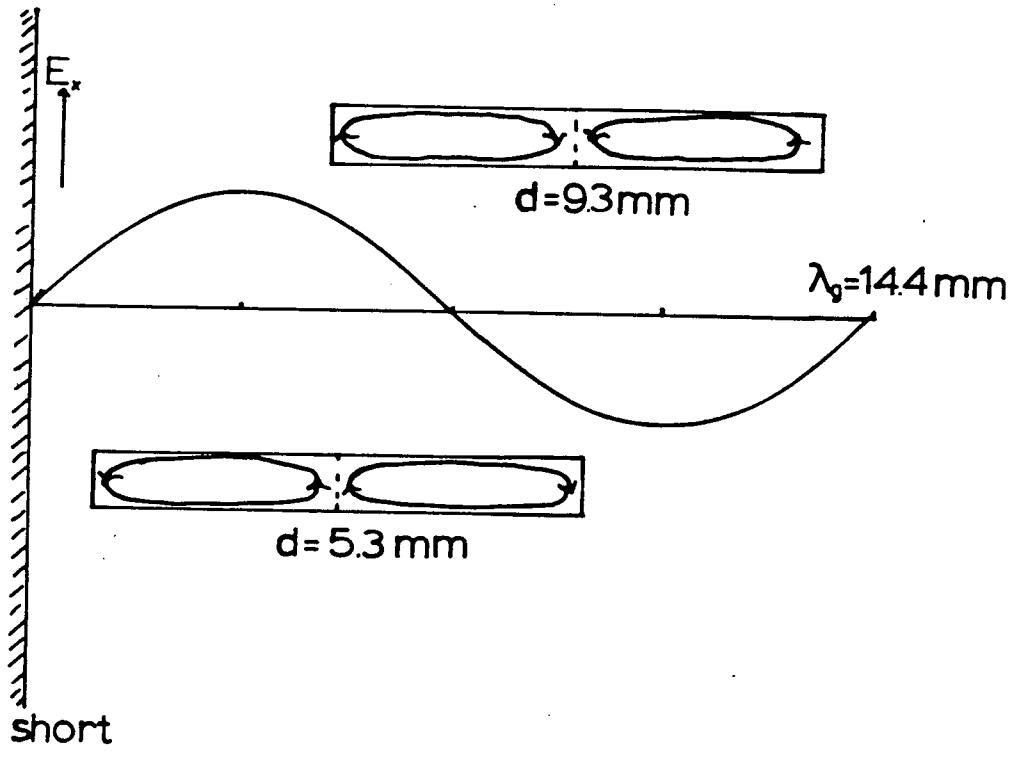

Figure 39. Diagram showing relationship of the wave guide fields to the proposed dielectric resonance fields for double resonance

guide wave length does not correspond to the wave length in the crystal, we expect that when one of the loops is in a position where it couples strongly to the fields in the guide, the other loop is roughly orthogonal to the wave guide fields. One can see that the two maximum coupling positions correspond to the positions for one or the other loop to be strongly coupled at $\lambda_g/2$. Both resonances are coupled when the centre of the crystal is at $\lambda_g/2$. The ratio of the couplings, at this position, is similar to the ratio of the maximum couplings.

In the weak coupling limit, it seems clear that there should be only one resonant frequency which should not be dependent on the position of the crystal. Even if we take the system to be strongly coupled, one simply expects the coupling to add vectorially and affect, at most, the phase of the resonance relative to the guide fields. At present, then, aside from some apparent significance of the relationship between the fields in the crystal and those in the guide, the origin of the double resonances remains a mystery.

6.2 The Imaginary Part of the Dielectric Constant

Information about the imaginary part of the dielectric constant, $\epsilon'' = 4\pi\sigma/\omega$, is accessible through the Q of the resonances. By substituting the imaginary dielectric constant, $\epsilon_b = \epsilon_b' + i\epsilon_b''$, into Eq.5.9, one can obtain the real and imaginary parts of the squared frequency if we neglect any loss due to ϵ_a''.

$$\text{Re}(f^2) = \frac{c^2}{4\pi^2}\left(\frac{k_x^2 + k_y^2}{\epsilon_b'^2 + \epsilon_b''^2}\right)\epsilon_b' + \frac{k_z^2}{\epsilon_a'} \tag{6.2}$$

$$\text{Im}(f^2) = -\frac{c^2}{4\pi^2}\left(\frac{\epsilon_b''}{\epsilon_b'^2 + \epsilon_b''^2}\right)(k_x^2 + k_y^2) \tag{6.3}$$

But the complex frequency for a lossy cavity is given by,

$$f = f_o - if_o/(2Q_o) \tag{6.4}$$

so that

$$f^2 = f_o^2 - f_o^2/(2Q_o) - 2if_o/(2Q_o) \approx f_o^2 - if_o/Q_o \tag{6.5}$$

Identifying the real and imaginary parts and assuming $\epsilon_b' >> \epsilon_b''$, we have

$$f_o^2 = f_{\parallel}^2 + f_{\perp}^2 \tag{6.6}$$

(6.7) $$f_o^2/Q_o = f_{||}^2\, \epsilon_b''/\epsilon_b'$$

where

(6.8) $$f_{||}^2 = (k_x^2 + k_y^2)\, c^2/(4\pi^2\epsilon_b')$$

(6.9) $$f_\perp^2 = c^2\, k_z^2\, /(4\pi^2\epsilon_a').$$

$f_{||}^2$ is just the mode plot intercept and f_o^2 is the squared frequency of a particular resonance. Eq. 6.7 can be rearranged to give

(6.10) $$\epsilon_b'' = \epsilon_b' f_o^2\, /(f_{||}^2\, Q_o\,).$$

Q_o is the intrinsic Q of the resonator. It is related to the observed Q_T and the coupling Q, Q_c, through

(6.11) $$1/Q_T = (1/Q_o) + (1/Q_c)$$

The reflection from a cavity is given by (Hidy et al. ,1972)

(6.12) $$R(\omega) = \frac{P_r}{P_i} = \frac{\frac{1}{4}\left(\frac{1}{Q_o} - \frac{1}{Q_c}\right)^2 + \left(\frac{\omega - \omega_o}{\omega_o}\right)^2}{\frac{1}{4}\left(\frac{1}{Q_o} + \frac{1}{Q_c}\right)^2 + \left(\frac{\omega - \omega_o}{\omega_o}\right)^2}$$

where P_r is the reflected power and P_i is the incident power.

On resonance, one has $(1/Q_T)\sqrt{R(\omega_o)} = |(1/Q_o) - (1/Q_c)|$, so that

$$1/Q_o = (1/2Q_T)(1 \pm \sqrt{R(\omega_o)}) \tag{6.13}$$

where the upper sign is for undercoupling and the lower for overcoupling.

σ_b' has been extracted, in this way, for six crystals and is plotted against frequency in Fig. 40. Error bars are shown for a number of resonances. The largest source of error lies in obtaining the width, and thus Q, from poorly shaped resonances. A possible systematic error arises in Eq. 6.10 where the ϵ_b' derived from each $f_{\parallel}$, for a given crystal, can be different. For the conductivities shown, the value of ϵ_b' used is the one appropriate to $f_{\parallel}$ for the resonance in question.

The most notable feature of Fig. 40 is that, for lower frequencies, the conductivities approach a single value whereas, for frequencies approaching 40 GHz, the conductivities are spread from about $0.2\,(\Omega\text{-cm})^{-1}$ to $1.4\,(\Omega\text{-cm})^{-1}$. There does appear to be a lower limit which is roughly frequency independent. Crystal 4 and 12, lying near this limit, were from the same batch.

An immediate question raised by these results has to do with the effect of the epoxy used to mount the crystals. This does not, in fact, appear to be a valid source of concern. There is no correlation between the observed losses and the

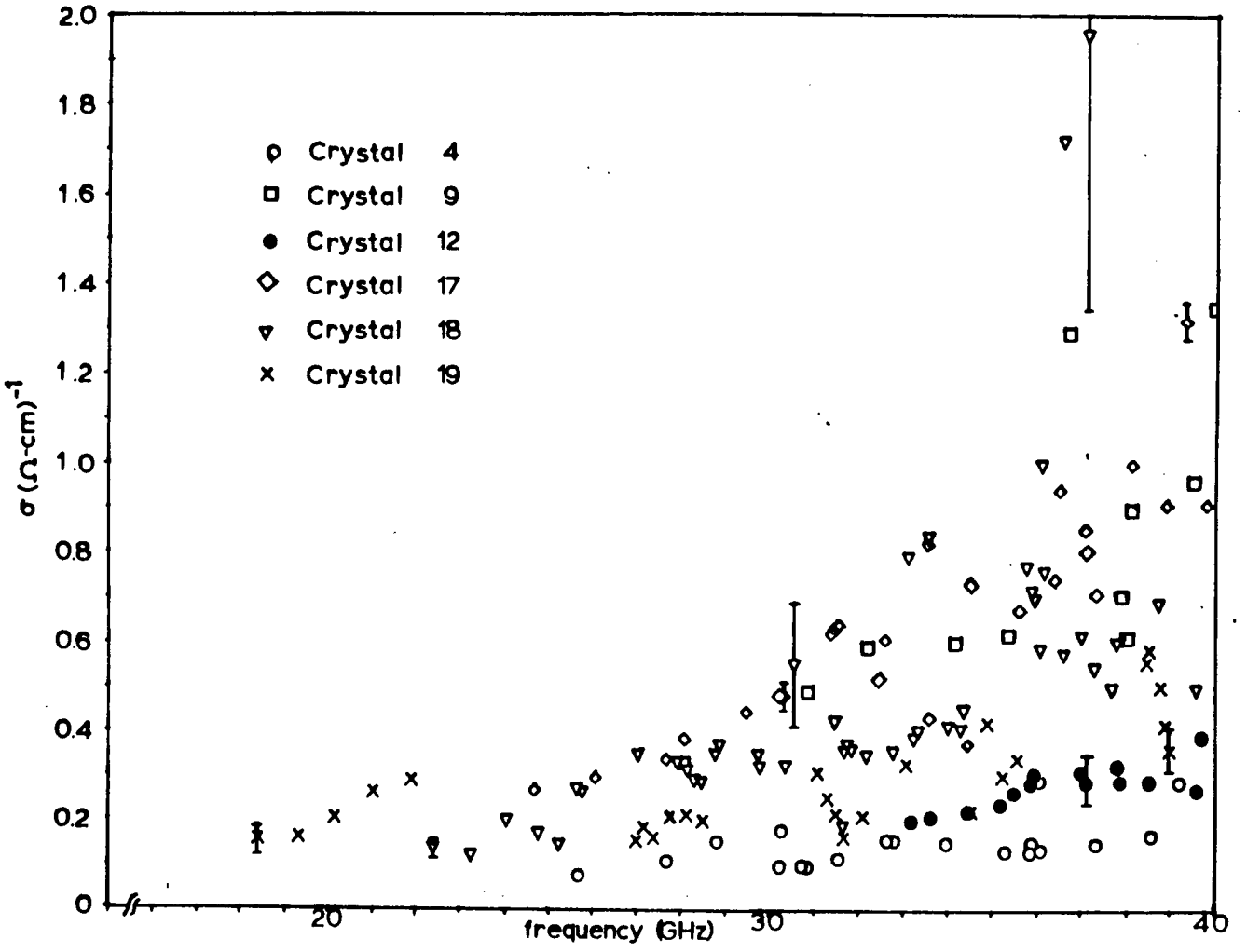

Figure 40. Plot of conductivity versus frequency for several TTF-TCNQ crystals studied by dielectric resonance.

quality of application of the epoxy. This was confirmed with measurements in which a quartz fibre was attached, with a large excess of epoxy, to the bottom of an already mounted crystal. The decrease in the Q of the resonance was found to be from 0 to 30%. While σ_b is proportional to 1/Q, this would not account for the range in observed σ_b even if the high σ_b crystals were those with excess epoxy. The lower limit of the observed conductivities lies slightly below the values observed by Barry (1977) in the earlier measurements.

The temperature dependence of the conductivities has also been studied. $\ln\sigma_b$ is plotted against 1/T for crystal 19 in Fig. 41. The data is taken from the B mode for a number of lengths of the crystal. It can be seen that, for 14K < T < 25K, there is an activation temperature of about 73K. The other crystals studied yield temperatures of 71K and 55K. Below 14K, there is a region in which σ_b does not appear to follow an $e^{-1/T}$ dependence. The average slope in this region is about -10K. A feature which is present in most of the temperature dependence data is a small local maximum around 10K. For lower frequency resonances, this can move up to 14K.

These results are notably different from those obtained using d.c. methods. Tiedje (1975) found the conductivity below 10K to be less less than $0.005(\Omega\text{-cm})^{-1}$ with an activation temperature of about 210K. Barry attributed the excess conductivity to a frequency dependent hopping conductivity

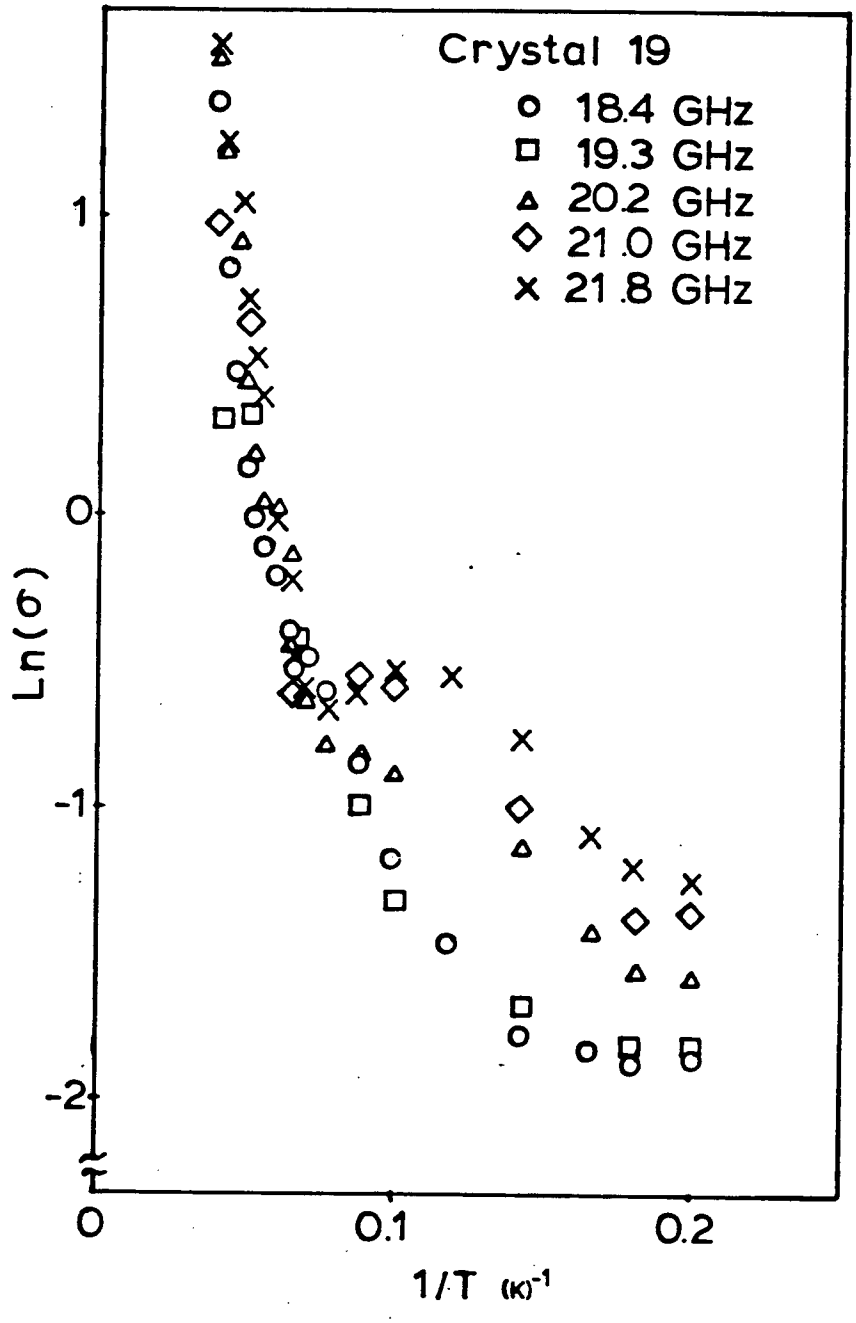

Figure 41. Plot of ln(σ) versus 1/T for crystal 19 at several frequencies.

associated with impurity states in the band gap. Mott and Davis (1971) consider such models in detail. There are a number of possible contributions to the conductivity. Two thermally activated processes involve thermally activated hopping within the impurity band and activated excitation from the impurity to the conduction band. The thermally activated hopping will normally be to the nearest neighbour and the conductivity will have the usual activated temperature dependence. At very low temperatures, variable range hopping can occur giving $\ln\sigma$ proportional to $(T)^{-\frac{1}{4}}$. In addition to these mechanisms, Mott and Davis discuss two mechanisms which can operate at finite frequency to give a temperature independent conductivity. The first involves a.c. hopping conduction and gives

$$\sigma(\omega) \propto \omega (\ln(\gamma_{ph}/\omega))^4$$

where γ_{ph} gives the strength of the electron-phonon interaction. If the impurity states are localized near the Fermi energy, optical transitions will be more important and there will be a contribution

$$\sigma(\omega) \propto \omega^2 (\ln(I_o/\hbar\omega))^4$$

where I_o is related to the depth and volume of the potential well in which the impurity is localized.

With this background, it seems possible to attribute the observed frequency dependence to optical transitions from the impurity to the conduction band. The temperature dependence observed below 10K is probably also related to the impurity band although it is not clear whether it is thermally activated nearest neighbour hopping or thermal excitations to the conduction band. The activated regime above 14K is likely due to transitions across the semi-conductor gap of TTF-TCNQ itself. The observed d.c. conductivity (Tiedje, 1975) is comparable to the microwave conductivity around 20K. The difference in d.c. and microwave activation temperature is not understood since one would expect the thermally activated impurity conduction to be present in the d.c. measurement as well as in the microwave measurement. The presence of the small local maximum between 10K and 14K has not been accounted for.

It would seem necessary, on the basis of these results, to consider the contribution to $\epsilon'(0)$ from the observed frequency dependent conductivities. This was done by using the Kramers-Kronig relations and terminating the integral at 40GHz. The contribution to $\epsilon'(0)$ from the observed conductivities is then given by

$$\Delta \epsilon'(0) = 8 \int_0^{2\pi \times 40 \times 10^9} \frac{\sigma(\omega)}{\omega^2} \, d\omega$$

The conductivity was taken to be quadratic with frequency. For crystals 17 and 18, the contribution to $\epsilon'(0)$ was found to be about 250. For crystal 12, the contribution was about 50. This, of course, neglects the contribution from the conductivity above 40GHz. It can be seen that the contribution to $\epsilon'(0)$ from the oscillator strength associated with the impurity conduction is not negligible. As a source of the spread in ϵ_b' as observed in this experiment, however it is probably not as important as the end effects discussed previously.

CHAPTER VII

Microwave Absorption Studies of TTF TCNQ

The infra-red absorption experiments on TTF-TCNQ by Eldridge and Bates (1979) have been interpretted as evidence for a strong mode in the neighbourhood of 102 GHz. It has been suggested that this proposed mode is associated with oscillations of a pinned charge density wave. The relation of such a pinned mode to the low frequency dielectric properties of TTF-TCNQ has been discussed in chapter I.

The region of the spectrum of interest here, roughly 3 cm^{-1} to 4 cm^{-1}, hinders direct observation of the pinned mode absorption in that this region lies just below that normally accessible to infra-red techniques. It is, however, just within the upper limit of microwave sources available in this laboratory.

The dielectric resonance technique, discussed in preceding chapters, is not useful at these frequencies. The major problem in interpreting resonances at these frequencies is the identification and separation of the modes. This might be alleviated, somewhat, by the use of very fine crystals. However, the interpretation of any mode plot obtained would still be hampered by the lack of understanding of potentially substantial end effects for such small crystals. Another source of difficulty in interpretation of a mode plot is that ϵ_b' would

be changing quickly in the region of the pinned mode with the result that the extrapolation technique used to extract ϵ_b' from the mode plots would break down.

It has been proposed (Hardy, 1979) that it should be possible to use a microwave analogue to the infrared bolometric techniques of Eldridge and Bates. In this technique, the absorption of incident radiation results in a temperature rise in the crystal. This rise in temperature is dectected by monitoring the d.c. conductivity of the crystal. In this chapter, we will discuss the initial results from an experiment of this type which is now in progress. The actual absorption measurements have been made in several microwave bands. While the construction of the crystal mounts and execution of the experiment is similar in all of the bands used, the microwave properties of the mount and the details of the measurement are more critical for the high frequency experiments. We will concentrate on the 75 to 110 GHz measurement and just mention, briefly, the qualitative results from the 26 to 40 GHz and 60 to 90 GHz experiments.

7.1 The Experiment

7.1a The Spectrometer

These experiments utilized the computer controlled microwave spectrometer described in Chapter IV. The 26 to 40 GHz spectrometer was run in the slow sweep mode in which a pre-calculated voltage ramp is output, via a D/A converter, to the external sweep input of a Weinschel sweep oscillator controlling a backward wave oscillator. Data was collected simultaneouly via an A/D convertor and stored for processing. For the 60 to 90 GHz and 75 to 110 GHz runs, the voltage ramp was supplied to a Singer sweep oscillator controlling a Micro-Now BWO power supply. The microwave power was modulated at between 50 and 100 Hz using the AM input on the 26-40 GHz source and using a Hughes model 44714H modulator for the higher bands. A variable attenuator was used after the source to control the power.

The crystal and microwave termination were located in a tubular can which could be pumped independently of the liquid helium space in the dewar. A carbon resistor thermometer and a wound heater were attached to the wave guide to allow for temperature regulation.

7.1b The Crystal Mount

There were several considerations in the design of the crystal mount. Firstly, in order that the microwave fields be polarized along the axis of interest, the crystal had to be mounted with the b axis across the centre of the wave guide and parallel to the electric fields. The absorbed power was detected by monitoring the d.c. conductivity of the crystal.

One end of the crystal was shorted to the guide. The other end was attached to a lead which was insulated from, and taken out through, the joint between two wave guide flanges. It was necessary to capacitively short this lead to the wave guide in order to minimize the extraction of R.F. power along it. This was done by using, as the d.c. lead, mylar sheathed copper foil sandwiched between the guide flanges. For the higher frequencies, it was important that the guide flanges mate properly. To facilitate this, the face of the guide flange was recessed to accept the foil.

It was also necessary that the crystal mount be flexible in order to allow for differential thermal contraction of the crystal and guide. This was most serious for the high frequency mounts for which the crystals used were normally very thin. For this mount, the connection between the crystal and the foil or flange was through gold wires silver painted onto the crystal. The high frequency mount is sketched in figure 42.

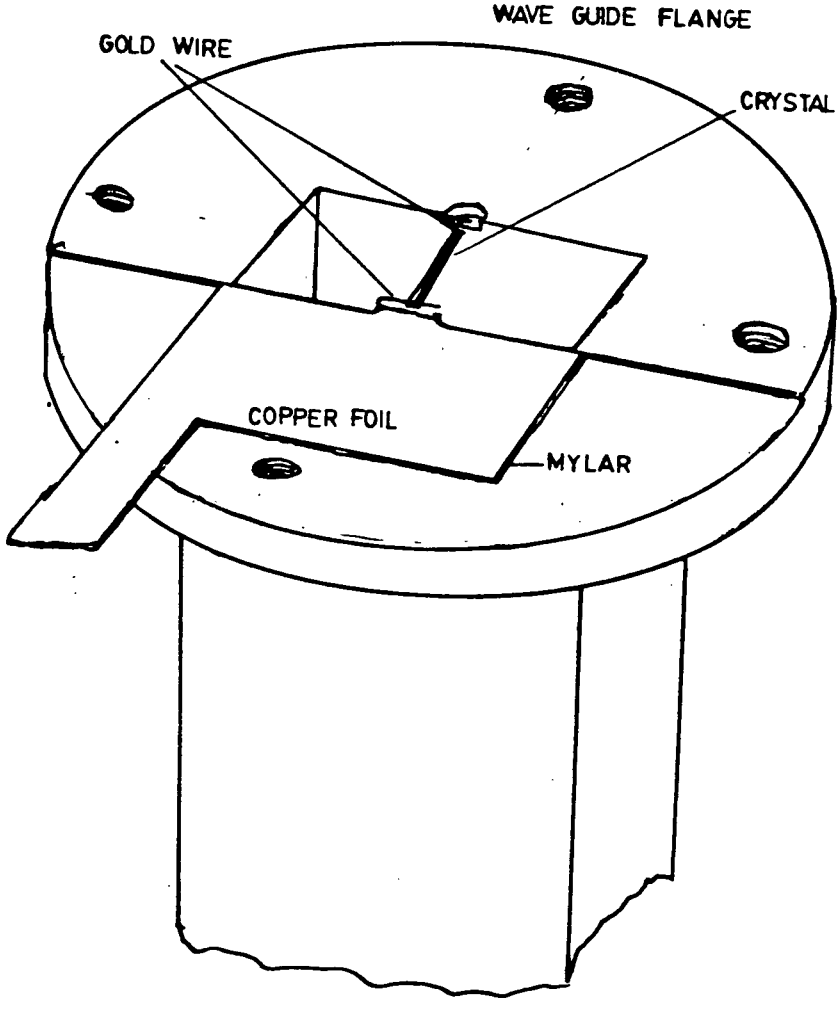

Figure 42. High frequency mount for microwave absorption studies in TTF-TCNQ.

7.1c Detection

The crystal bias circuit was simply a 10M metal film resistor and a 9 Volt Eveready 1222 battery in series with the crystal. The 10MΩ resistor was at low temperature and connected to the crystal through the waveguide. The voltage across the 10MΩ resistor was fed to an Ithaco Dynatrac 391A lock-in amplifier. The analogue output from the lock-in amplifier was fed to the computer for storage.

It was also necessary to correct for variations in the incident power. For the 26 to 40 GHz and 60 to 90 GHz bands, this was done by attaching a power meter or a crystal detector below the crystal and recording the power across the band in a separate room temperature experiment. Using these traces to ratio the raw data gave spectra which were proportional to the absorption, except for a weakly frequency dependent factor correcting for the change in wave guide velocity across the band. This procedure has two disadvantages; a) the incident power will certainly change with temperature of the cryostat and b) the response of the crystal detector is not very flat with frequency. Of course, an absolute measurement also also requires an absolute measurement of incident power as well as a calibration of the absorbed power signal.

The necessary steps to obtain the absolute absorption have been carried out for one crystal in the 75 to 110 GHz band. The

incident power was detected in situ using a five couple Au-Fe/Chromel-p thermopile with one end anchored to the wave guide termination below the crystal and the other end anchored to the crystal mount. The signal from the thermopile was detected with a Keithly 148 nanovoltmeter. The output of the BWO was also monitored using a directional coupler and crystal detector. The "SYNSWEEP" option of "SWCONTROL" was altered to allow simultaneous input on three channels so that output from the lock-in, nanovoltmeter, and crystal detector could be recorded together. The phase locking feature of the option was not used. The three channel modification of the program allowed continuous adjustment of the BWO grid voltages with no effect on the ratio operation. The thermopile output was calibrated using a 200Ω heater wound on the terminator at the thermopile anchor. The thermopile signal corresponding to a given d.c. power input could be plotted. The assumption was then made that this calibration would be appropriate to the R.F. power absorbed. Because of the modulation, the peak R.F. power was, in fact, twice the observed power level indicated by this calibration.

The signal from the crystal also had to be calibrated. The change in voltage across the 10MΩ resistor was related to the change in the crystal resistance, ΔR_c, by

$$V=-V_B \Delta R_c R_B/(R_B+R_c)^2$$

where $R_B = 10M\Omega$, V_B is the battery voltage, and R_c is the crystal resistance. This resistance depended strongly on the d.c. bias current and was typically $10M\Omega$ to $100M\Omega$ at a temperature of 10K. The calibration of ΔR_c to incident microwave power was obtained by passing a d.c. current through the crystal and plotting the observed resistance against the power deposited in the crystal this procedure then assumes that the heating effect of the d.c. power and microwave absorption is equivalent. Using the curve obtained, it was possible to first find the d.c. "operating point" due to the biasing battery. The slope then gave $\Delta R_c / P$. This finally allowed one to calibrate the signal from the lock-in amplifier in terms of power absorbed. The ratioed spectrum could then be calibrated in terms of absorption.

We note here that in the presence of intrinsic non-ohmic effects, the equivalence of d.c, and r.f heating may not be valid. This point is currently under investigation.

7.2 Results

The use of TTF-TCNQ crystals as bolometers was first tested in the 26 to 40 GHz band. By first calibrating a variable attenuator and then using the attenuator to measure the signal as a function of incident power, it was found that the signal was linear with power up to at least 2mW incident power at 30 GHz.

Two crystals were studied in the 26 to 40 GHz band. Both spectra showed some sharp features which were attributed to dielectric resonances. For one crystal studied, the background absorption was found to be roughly flat while, for the other, it was found to increase by a factor of 3 across the band. This behaviour is not inconsistent with the variation in the frequency dependent conductivity across this band as observed by dielectric resonance.

One crystal was studied in the 60 to 90 GHz band. The absorption appeared to be decreasing slightly from 60 to 70 GHz although the apparent presence of strong standing waves in both the ratioed and the background spectra, in this region, casts some doubt on the success of the ratioing in this instance. Above 70 GHz, the absorption was flat with the exception of one feature near 90 GHz. This is believed to be a dielectric resonance.

The same crystal was also studied in the 75 to 110 GHz

band. The non-linearity of the resistance versus d.c. power calibration has been a source of some concern in that the absorbed power calibration becomes strongly dependent on the position of the biasing point. Figure 43 shows an absorption spectrum obtained using the most reliable R_c versus power curve obtained. It can be seen that, in addition to several features between 85 and 100 GHz, there is a prominent feature at about 107.5 GHz. If we mentally smooth the sharp spikes ... which are likely due to higher modes associated with the use of 60 to 90 GHz wave guide well above 100 GHz, we find a peak ratio (absorbed power/ incident power) of about $150X10^{-5}$, where we have included the factor of 2 associated with the fact that we have only measured the average incident power. The ratio between 75 GHz and 85 GHz is between $3X10^{-5}$ and $5X10^{-5}$.

We can convert these into rough measures of the conductivity if we make some assumptions about the electric fields in the crystal. The relation of power down a wave guide to the peak electric field, E_{ox}, can be found in electromagnetism texts such as Lorrain and Corson (1970). They give, in MKS units,

$$\text{power} = (E_{ox}^2\, ab/4c\mu_o)\,(1-(\lambda_o/2b)^2)^{\frac{1}{2}}$$

where a is the height of the wave guide, b is the width of the wave guide, c is the speed of light, and λ_o is the free space

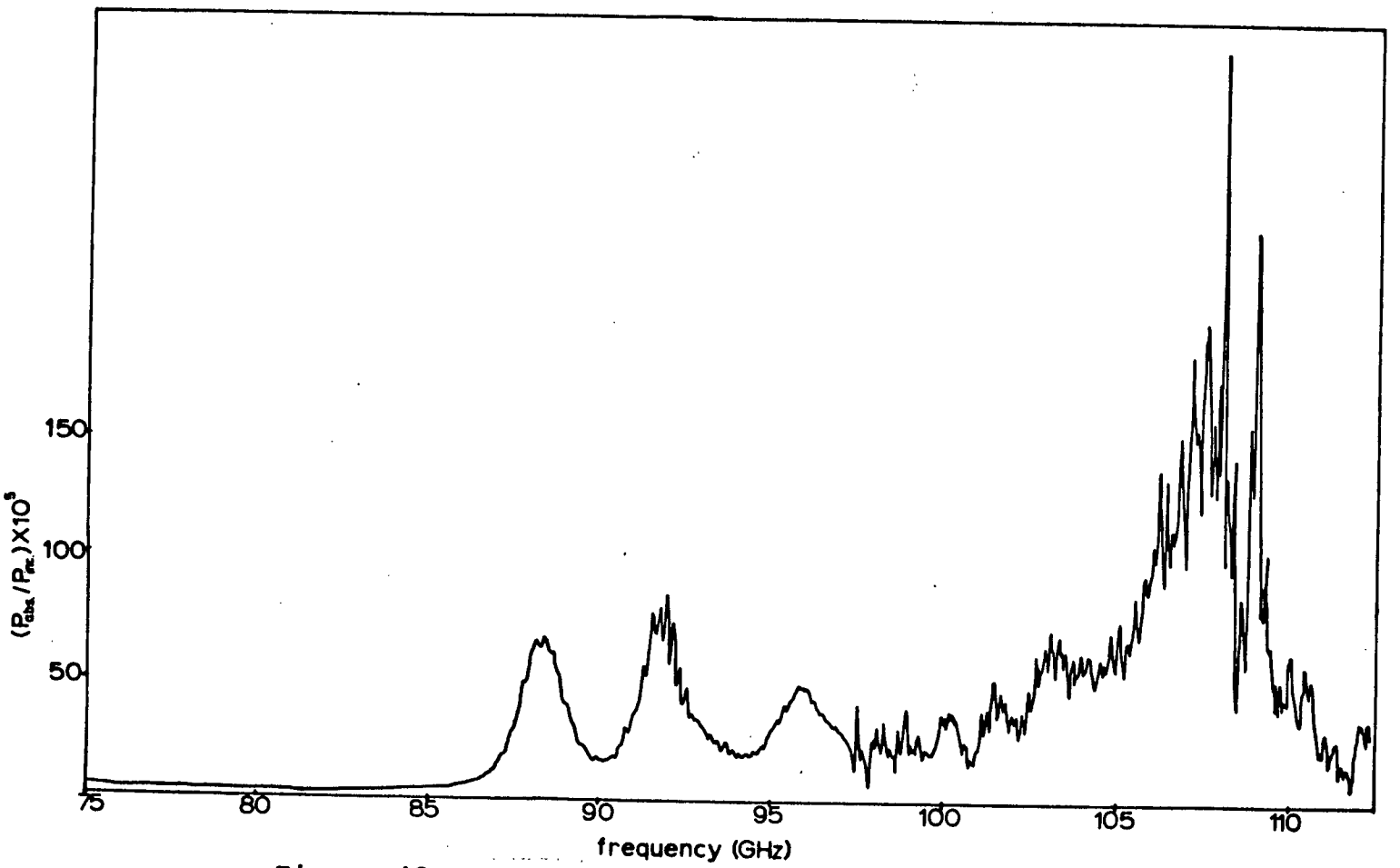

Figure 43. Spectrum showing the ratio of absorbed to incident power for the TTF-TCNQ crystal studied in the 75 to 110 GHz band.

wave length. If we assume that the effect of depolarizing fields are removed by the a.c. shorting of the crystal to the guide, then the power absorbed by the crystal is

$$P_{abs} = a' b' \Delta z E_{ox}^2 \sigma/2 \text{ watts}$$

where a', b', and Δz are dimensions of the crystal and σ is the conductivity in $(\Omega\text{-M})^{-1}$. This is correct assuming a crystal length equal to the wave guide height. The dimensions of the crystal used were 1.16 mm by 0.065 mm by 0.038 mm. The guide dimensions were 1.5 mm by 3 mm. For these conditions, we find

$$\sigma(f)\,(\Omega\text{-M})^{-1} = 2.1\text{X}10^{3}\,(1-(49.97/f)^{2})^{\frac{1}{2}}\,(P_{abs}/P_{inc.})$$

where f is the frequency in GHz. Using this formula, we find that, between 75 and 85 GHz, $\sigma(f)$ is about $6.6\text{X}10^{-4}$ $(\Omega\text{-cm})^{-1}$ and that, near 107.5 GHz, σ is about $2.8\text{X}10^{-2}$ $(\Omega\text{-cm})^{-1}$. The resistance at the d.c. operating point was 26 MΩ which implies a d.c. conductivity of about $2\text{X}10^{-4}(\Omega\text{-cm})^{-1}$. The 75 GHz conductivity appears to be of this order of magnitude whereas one would expect it to be at least as large as the conductivity at lower frequencies. The typical conductivity at 40 GHz and 10K was between $0.3(\Omega\text{-cm})^{-1}$ and $1(\Omega\text{-cm})^{-1}$. If we accept that the 75 GHz conductivity at 10K should be at least 0.5 $(\Omega\text{-cm})^{-1}$, then the peak conductivity is raised to about 20 $(\Omega\text{-cm})^{-1}$. It is thus

important to determine whether the apparent low conductivity at 75 GHz is real or just an artifact of the experimental analysis.

It is of interest to calculate the expected peak conductivity required for a mode of width 5 GHz centred at 107 GHz to give rise to the observed low frequency dielectric constant of about 3000. This conductivity is found to be about 2400 $(\Omega\text{-cm})^{-1}$. For a mode of width 3 GHz, this goes to about 4000 $(\Omega\text{-cm})^{-1}$.

The observed peak conductivity is clearly unable to account for the low frequency dielectric constant. The effect of the depolarizing fields, if the crystal were not shorted to the walls, would be to decrease the absorption. For the present crystal, with a depolarizing factor of about $5X\ 10^{-3}$, the observed absorption would be decreased by a factor of about $1.6X10^{-5}$. If this were the case, the observed feature might be able to account for the missing oscillator strength. Again, however, we point out that depolarizing effects should not be significant in the present experiment so that the fields in the crystal should approximate those in the guide. Of course for high enough σ one gets a strong reflection from the crystal, in which case the electric field in the guide is less than that of the incident wave. It is not yet clear whether we are in this regime or not.

At present, then, the observed feature at 107.5 GHz is not found to have sufficient oscillator strength to account for the

high values of ϵ_b' observed at low frequency.

7.3 Future Directions

Absorption experiments of this type still seem to offer some hope for direct observation of the pinned charge density wave if its pinning frequency lies below 120 GHz. Experiments are presently underway in which the calibration of the absorption signal and the microwave properties of the crystal mount will be refined. One benefit of using a variety of crystals and mounts will be to allow mount-specific and dielectric resonances to be distinguished.

The present experiment, then, must be taken as inconclusive. There appears to be some question as to the validity of the absorption to conductivity conversion in light of the low conductivity obtained at 75 GHz. It is also necessary to identify the components of the spectrum which are specific to certain crystals and mounts so that the features due to microscopic properties of TTF-TCNQ can be isolated and studied.

CHAPTER VIII

Summary

In the first part of this work, the electrical properties of $MEM(TCNQ)_2$ were studied in the neighbourhood of the dimer to monomer transition at 60 ° C. The microwave and d.c. conductivities were found to be in general agreement. Just below the transition, the microwave conductivity was found to be between 0.014 and 0.017 $(\Omega\text{-cm})^{-1}$. Above the transition, σ rose to between 14 and 32 $(\Omega\text{-cm})^{-1}$. The activated behaviour of the conductivity in the dimerized phase, as observed by d.c. methods, was confirmed down to room temperature.

Some discussion was offered regarding the difficulty inherent in interpreting these results in terms of the Hubbard models for the TCNQ chains. Clarification of the role of the on-site repulsion in determining the properties of this material will have to come from other measurements such as the magnetic susceptibility and thermopower.

In the second part of this work, the dielectric resonator studies on TTF-TCNQ as done by Barry (1977) were extended. The main results were the clarification of the behaviour of the coaxial-like mode and some understanding of the systematic errors introduced by end effects into the extraction of dielectric constants from the mode plots. The low frequency value of ϵ_b' was estimated to be $(3.0\pm0.4)X10^3$. It was suggested

that the value of ϵ_a' is at least 9 and there were indications that ϵ_c' could be considerably larger. The spread in conductivities as obtained in the dielectric resonance measurements was felt to imply that below 40 GHz, the frequency dependence of the conductivity was specific to particular crystals and thus, likely, due to impurity effects. This was to some extent confirmed by the temperature dependence of the conductivity.

The final part of the work involved some preliminary attempts at direct observation of the pinned charge density wave using microwave absorption in a TTF-TCNQ bolometer. There is still work needed, both in refining the technique and obtaining sufficient data to distinguish between the effects of microwave resonances in the apparatus and intrinsic properties of the crystals. The results of these experiments are awaited with some anticipation.

APPENDIX A

Tight Binding Calculations for a Linear Chain with a Basis

We first consider a linear chain of atoms with alternating separations of b and (c-b). The unit cell dimension is then c. The wavefunction for the atom at site R is a(r-R). We can construct a wave function, satisfying the Bloch conditions, of the form,

A.1 $$\Psi_\alpha(r) = (N)^{-\frac{1}{2}} \sum_{R_n} e^{ikR_n} \; a(r-R_n-z_\alpha)$$

where α=1 or 2, z_1=0, z_2=b, and R_n =nc. We thus have,

(A.2a) $$\Psi_1(r) = N^{-\frac{1}{2}} \sum_{R_n} e^{ikR_n} \; a(r-R_n)$$

(A.2b) $$\Psi_2(r) = N^{-\frac{1}{2}} \sum_{R_n} e^{ikR_n} \; a(r-R_n-b)$$

The off diagonal elements of the Hamiltonian are given by

(A.3a) $$(\Psi_1(r) \mathcal{H} \Psi_2(r)) = N^{-1} \sum_{R_n R_n'} e^{ik(R_n'-R_n)} \int a^*(r-R_n) \mathcal{H} \, a(r-R_n'-b) \, dr$$

(A.3b) $$(\Psi_2(r) \mathcal{H} \Psi_1(r)) = N^{-1} \sum_{R_n R_n'} e^{ik(R_n'-R_n)} \int a^*(r-R_n-b) \mathcal{H} \, a(r-R_n') \, dr$$

Defining

(A.4) $$-t_1 = \int a^*(r-R_n)\,\mathcal{H}\,a(r-R_n-b)\,dr$$

and

(A.5) $$-t_2 = \int a^*(r-R_n)\,\mathcal{H}\,a(r-R_{n-1}-b)\,dr$$

we get

(A.6) $$(\psi_1(r)\,\mathcal{H}\,\psi_2(r)) = t_1 + t_2 e^{-ikc}$$

and

(A.7) $$(\psi_2(r)\,\mathcal{H}\,\psi_1(r)) = t_1 + t_2 e^{ikc} \quad .$$

Defining E_o, the diagonal element, we obtain the electronic energy,

(A.8) $$\epsilon_k = E_o \pm \sqrt{t_1^2 + t_2^2 + 2t_1 t_2 \cos(kc)} \quad .$$

At $k=0$, $\epsilon_k - E_o = \pm(t_1+t_2)$ and at $k = \pi/c$, $\epsilon_k - E_o = \pm|t_1-t_2|$. This relation thus describes two bands each of width $2t_2$ separated by a gap of $2|t_1-t_2|$.

APPENDIX B

Anisotropic Dielectric Wave Guides with and without Outer Conductors

We will begin by reviewing some of the results given by Barry (1977), and then extend these to the case where E_z contains an $e^{i\phi}$ azimuthal dependence.

We will deal with an infinite dielectric rod of radius R_1 within a circular metallic tube of radius R_2. The axis of symmetry is the Z axis. The dielectric rod has $\epsilon_x = \epsilon_y = \epsilon_\perp \neq \epsilon_z$. Taking μ to be 1, the fields inside of the guide are shown, by Barry, to satisfy

B.1 $$E_r = \frac{i}{k_\perp^2}\left(k_z \frac{\partial E_z}{\partial r} + \frac{\omega}{c}\frac{1}{r}\frac{\partial H_z}{\partial \phi}\right)$$

B.2 $$E_\phi = \frac{i}{k_\perp^2}\left(\frac{k_z}{r}\frac{\partial E_z}{\partial \phi} + \frac{\omega}{c}\frac{\partial H_z}{\partial r}\right)$$

B.3 $$H_r = \frac{i}{k_\perp^2}\left(\frac{\partial H_z}{\partial r} - \frac{\omega \epsilon_\perp}{c}\frac{1}{r}\frac{\partial E_z}{\partial \phi}\right)$$

B.4 $$H_\phi = \frac{i}{k_\perp^2}\left(\frac{k_z}{r}\frac{\partial H_z}{\partial \phi} + \frac{\omega \epsilon_\perp}{c}\frac{\partial E_z}{\partial r}\right)$$

where

B.5 $$k_\perp^2 = (\omega^2/c^2)\epsilon_\perp - k_z^2$$

Outside of the dielectric, the fields are the same but with $\epsilon_\perp$ replaced by 1 and $k_\perp^2$ replaced by

B.6 $$k_2^2 = (\omega^2/c^2) - k_z^2$$

The wave equations for E_z and H_z, inside the dielectric, can be shown to be

B.7 $$\frac{\partial^2 F}{\partial r^2} + \frac{1}{r}\frac{\partial F}{\partial r} + \left[k_1^2 - \frac{n^2}{r^2}\right] F = 0$$

and

B.8 $$\frac{\partial^2 G}{\partial r^2} + \frac{1}{r}\frac{\partial G}{\partial r} + \left[k_\perp^2 - \frac{n^2}{r^2}\right] G = 0$$

where

B.9 $$k_1^2 = (\epsilon_z/\epsilon_\perp) k_\perp^2$$

and

B.10 $$E_z(r,\phi) \propto F(r) e^{in\phi}$$

B.11 $$H_z(r,\phi) \propto G(r)e^{in\phi}$$

Outside of the dielectric, k_1^2 and $k_\perp^2$ are replaced by k_2^2. The solutions to Eqs. B.7 and B.8 are cylindrical Bessel functions. In general, inside the dielectric, one uses

B.12 $$F(r) = A_1 J_n(k_1 r)$$

B.13 $$G(r) = A_2 J_n(k_\perp r)$$

and outside of the dielectric, one uses

B.14 $$F(r) = B_1 H_n^1(k_2 r) + C_1 H_n^2(k_2 r)$$

B.15 $$G(r) = B_2 H_n^1(k_2 r) + C_2 H_n^2(k_2 r)$$

One can then consider various situations. For n=0 and $R_2=\infty$, one requires that k_2^2 be less than or equal to 0 in order for the wave to be guided. It is also necessary to have C_1 and C_2 equal to 0 for the fields at the centre to be finite. For imaginary k_2, it is convenient to replace $H_0^1(k_2 r)$ by

$$-(2i/\pi)K_0(\gamma r)$$

where $\gamma^2=-k_2^2$. The solutions for n=0 can be separated into

T.E. and T.M. modes. Application of the boundary conditions allows one to construct equations for the coefficients. The condition for a non-trivial solution for these coefficients is that the determinant of the coefficient matrix be 0. This is found to imply

B.17 $$\epsilon_2 \gamma K_0(\gamma R_1) J_1(k_1 R_1) + k_1 J_0(k_1 R_1) K_1(\gamma R_1) = 0$$

When R_2 is made finite, one must include the terms involving C_1 and C_2. k_2^a can now be both positive and negative. One can still set $H_z=0$. For $k_2^a > 0$, E_z outside of the dielectric is given by

B.18 $$E_z(r) = (B_1 J_0(k_2 r) + C_1 Y_0(k_2 r))\, e^{i k_z Z}$$

and the characteristic equation becomes

B.19
$$\{J_0(k_1 R_1)/k_2\}\{Y_1(k_2 R_1) J_0(k_2 R_2) - J_1(k_2 R_1) Y_0(k_2 R_2)\}$$
$$-\{\epsilon_z J_1(k_1 R_1)/k_1\}\{Y_0(k_2 R_1) J_0(k_2 R_2) - J_0(k_2 R_1) Y_0(k_2 R_2)\} = 0$$

For $k_2^a < 0$, the fields outside of the dielectric are given in terms of $I_n(\gamma r)$ and $K_n(\gamma r)$. The characteristic equation is then

$$\{J_0(k_1 R_1)/\gamma\}\{I_1(\gamma R_1)K_0(\gamma R_2)-K_1(\gamma R_1)I_0(\gamma R_2)\}$$

B.20

$$-\{(\epsilon_z/k_1)J_1(k_1R_1)\}\{I_0(\gamma R_2)K_0(\gamma R_1)-I_0(\gamma R_1)K_0(\gamma R_2)\} = 0$$

The solutions of these characteristic equations have been discussed in Chapter V.

One can then go on to discuss the case for n=1. H_z cannot be set to 0 for this case so the solutions become considerably more complicated. For the dielectric wave guide case, it is again necessary that k_2 be imaginary. The external fields are then conveniently discussed in terms of $K_0(\gamma r)$ and $K_1(\gamma r)$. The resulting characteristic equation is Eq. B.21 and appears on the following page.

When R_2 is made finite, k_2 can again be both real and imaginary. The boundary equations again result in equations for the coefficients which have non-trivial solutions only if the determinant of the coefficient matrix is 0. For the $k_2^2 > 0$ case, the resulting characteristic equation, Eq. B.23, appears below. For the $k_2^2 < 0$ case, the convenient replacements for the Bessel functions are

$$K_1(\gamma r) \text{ for } J_1(k_2 r)$$

B.22

$$K_0(\gamma r) \text{ for } J_0(k_2 r)$$

EQUATION B.21

$$\frac{\omega^2}{c^2} R_1^2 \epsilon_1 \left[-J_1(k_1 R_1)\left\{1 - \frac{k_1^2}{\epsilon_1 k_2^2}\right\} + k_1 R_1 J_0(k_1 R_1) + J_1(k_1 R_1) \frac{k_1^2}{k_2^2} \frac{\gamma R_1}{\epsilon_2} \frac{K_0(\gamma R_1)}{K_1(\gamma R_1)} \right]$$

$$\cdot \left[J_1(k_2 R_1)\left\{1 - \frac{k_1^2}{k_2^2}\right\} - k_2 R_1 J_0(k_2 R_1) - J_1(k_2 R_1) \frac{k_1^2}{k_2^2} \frac{\gamma R_1}{\epsilon_2} \frac{K_0(\gamma R_1)}{K_1(\gamma R_1)} \right]$$

$$+ k_2^2 R_1^2 J_1(k_2 R_1) J_1(k_1 R_1) \left\{1 - \frac{k_1^2}{k_2^2}\right\}^2 = 0$$

EQUATION B.23

$$-\left[\frac{k_z}{R_1}\right]^2\left[1-\frac{k_1^2}{k_2^2}\right]^2\left[J_1(k_1R_1)\,J_1(k_1R_1)\right]\left[J_1(k_2R_1)Y_1(k_2R_2)-J_1(k_2R_2)Y_1(k_2R_1)\right]$$

$$\cdot\left[J_1(k_2R_1)\left\{k_2Y_0(k_2R_2)-\frac{Y_1(k_2R_2)}{R_2}\right\}-Y_1(k_2R_1)\left\{k_2J_0(k_2R_2)-\frac{J_1(k_2R_2)}{R_2}\right\}\right]$$

$$+\frac{\omega^2}{c^2}\left(\epsilon_\perp\left[k_1J_0(k_1R_1)-\frac{J_1(k_1R_1)}{R_1}\right]\left[J_1(k_2R_1)Y_1(k_2R_2)-J_1(k_2R_2)Y_1(k_2R_1)\right]\right.$$

$$-\frac{k_1^2}{k_2^2}J_1(k_2R_1)\left[\left\{k_2J_0(k_2R_1)-\frac{J_1(k_2R_1)}{R_1}\right\}Y_1(k_2R_2)-\left\{k_2Y_0(k_2R_1)-\frac{Y_1(k_2R_1)}{R_1}\right\}J_1(k_2R_2)\right]\Big)$$

$$\cdot\left(\left[J_1(k_2R_1)\left\{k_2Y_0(k_2R_2)-\frac{Y_1(k_2R_2)}{R_2}\right\}-\left\{k_2J_0(k_2R_2)-\frac{J_1(k_2R_2)}{R_2}\right\}Y_1(k_2R_1)\right]\left[k_1J_0(k_1R_1)-\frac{J_1(k_1R_1)}{R_1}\right]\right.$$

$$\frac{k_1^2}{k_2^2}J_1(k_1R_1)\left[\left\{k_2J_0(k_2R_1)-\frac{J_1(k_2R_1)}{R_1}\right\}\left\{k_2Y_0(k_2R_2)-\frac{Y_1(k_2R_2)}{R_2}\right\}\right.$$

$$\left.\left.-\left\{k_2Y_0(k_2R_1)-\frac{Y_1(k_2R_1)}{R_1}\right\}\left\{k_2J_0(k_2R_2)-\frac{J_1(k_2R_2)}{R_2}\right\}\right]\right)=0$$

$$I_1(\gamma r) \text{ for } Y_1(k_2 r)$$

B.22 cont.

$$I_0(\gamma r) \text{ for } Y_0(k_2 r) \ .$$

Terms of the form $(k_2 Z_0(k_2 r) - (Z_1(k_2 r)/r))$ are derivatives of $Z_1(k_2 r)$ and k_2 is replaced by γ while the the Bessel functions are replaced according to B.22. The solutions for this equation are also discussed in Chapter V.

APPENDIX C

Dielectric Resonance Mode Plots for Several TTF-TCNQ Crystals

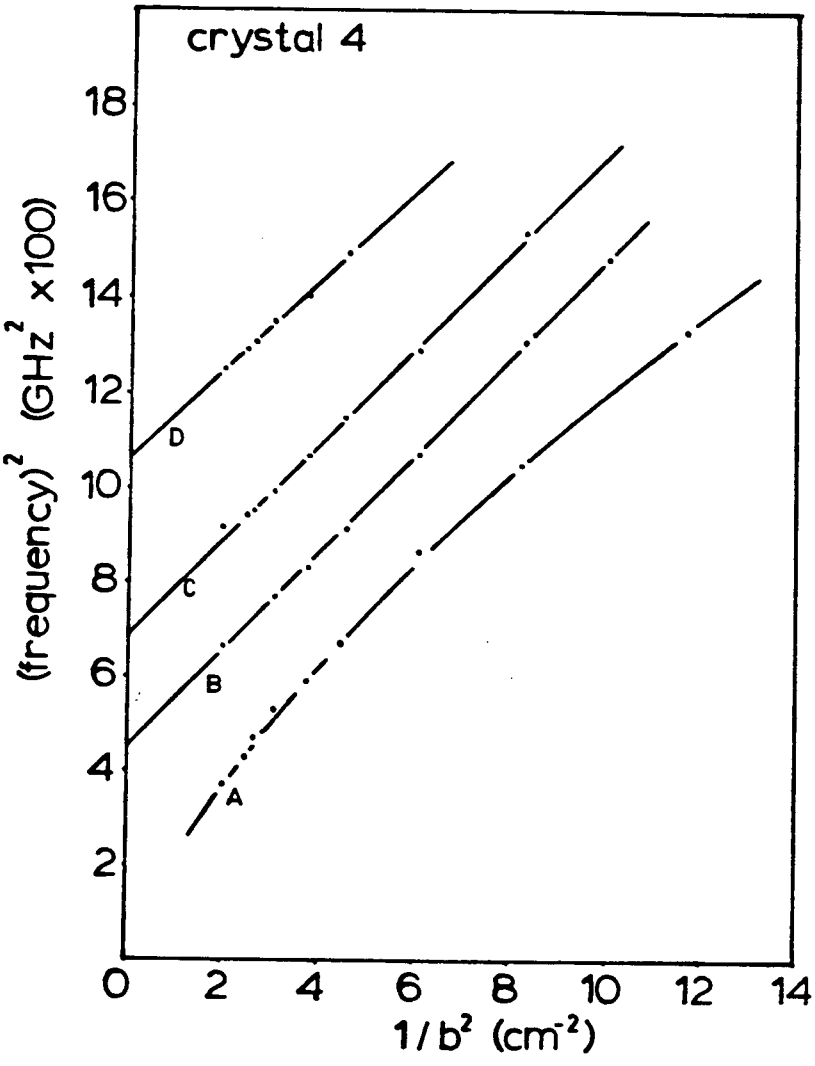

Figure 44. Dielectric resonance mode plot for TTF-TCNQ crystal 4

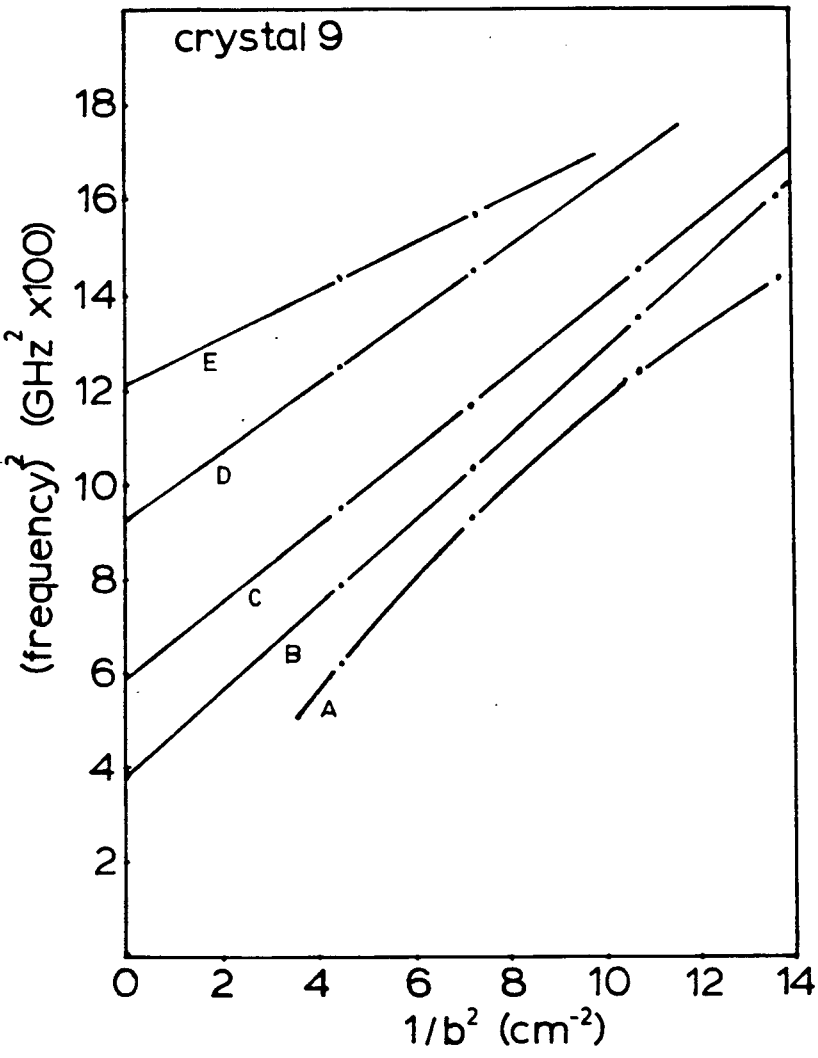

Figure 45. Dielectric resonance mode plot for TTF-TCNQ crystal 9.

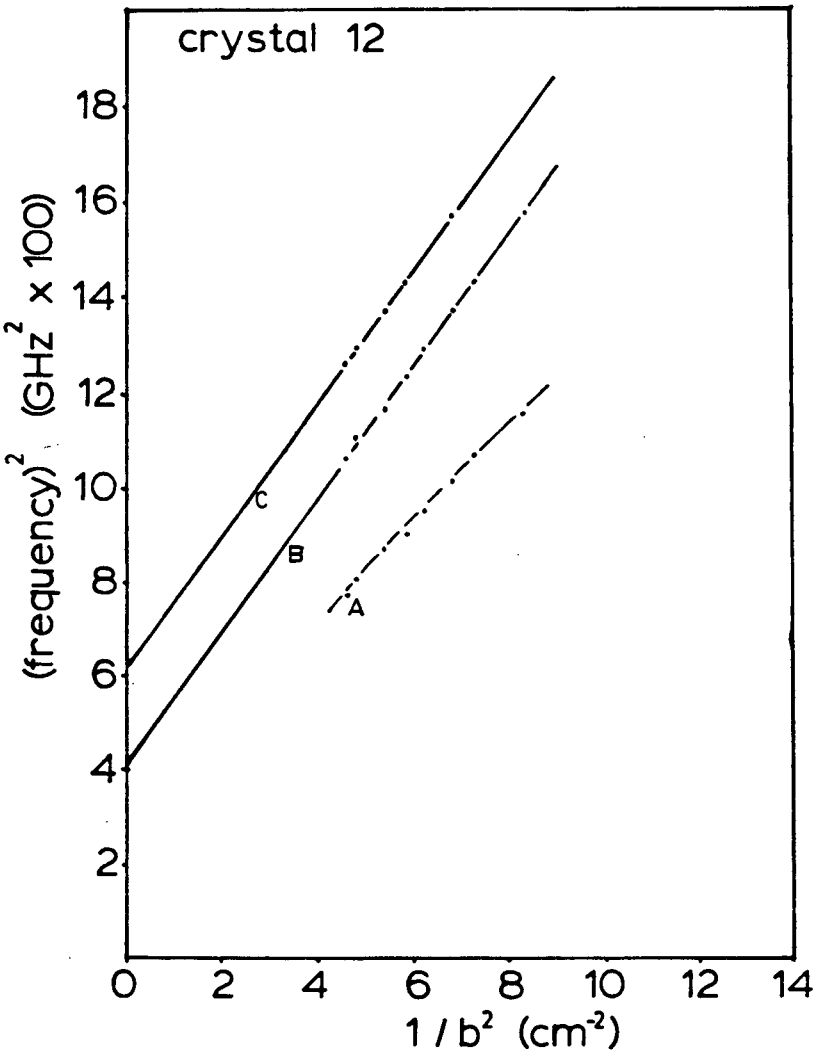

Figure 46. Dielectric resonance mode plot for TTF-TCNQ crystal 12

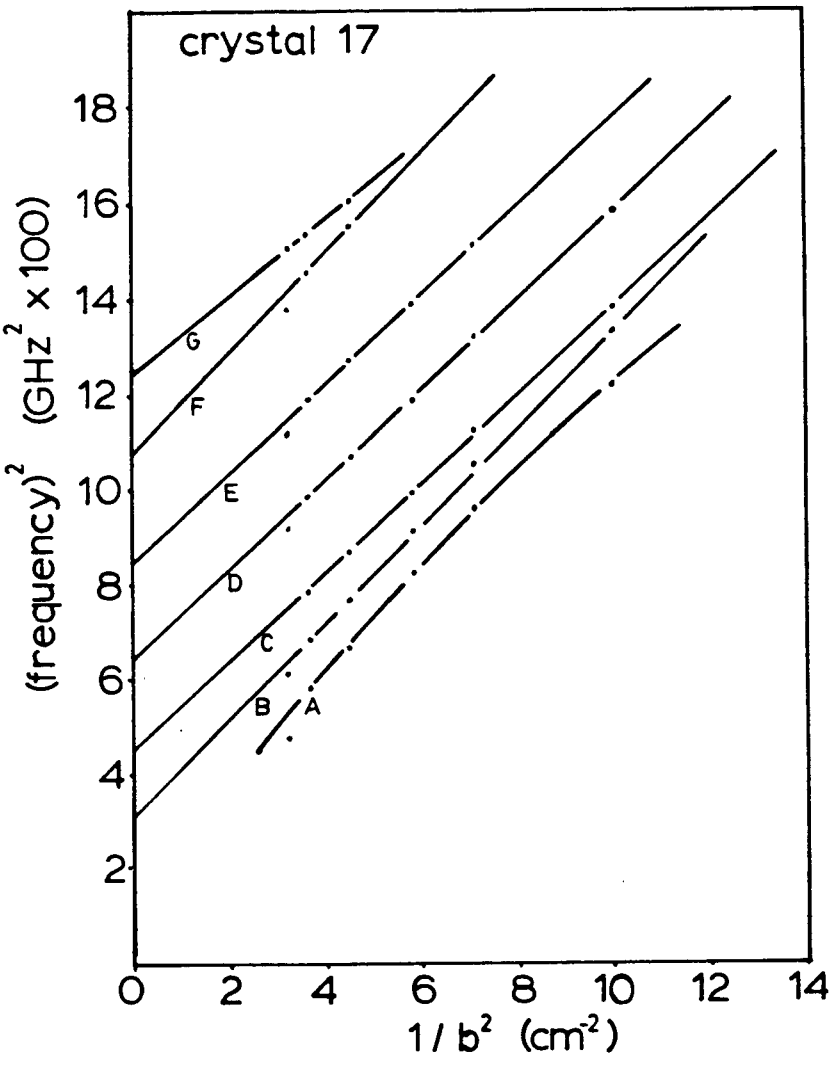

Figure 47. Dielectric resonance mode plot for TTF-TCNQ crystal 17.

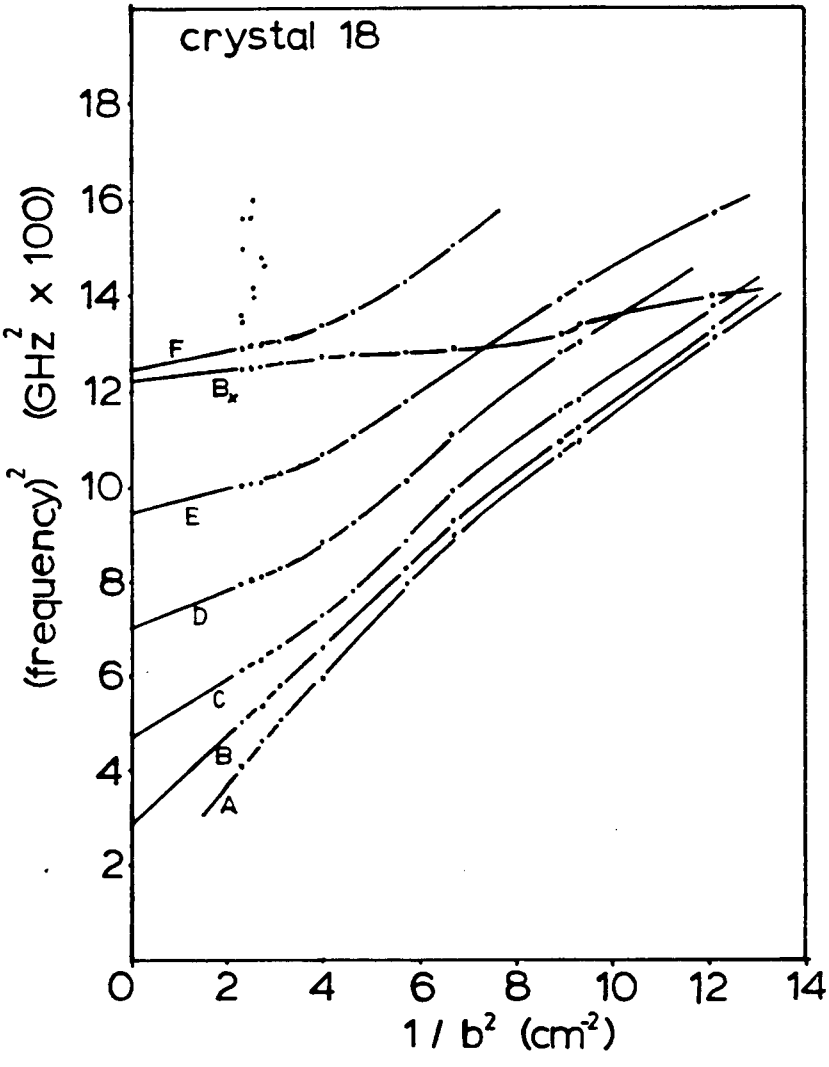

Figure 48. Dielectric resonance mode plot for TTF-TCNQ crystal 18.

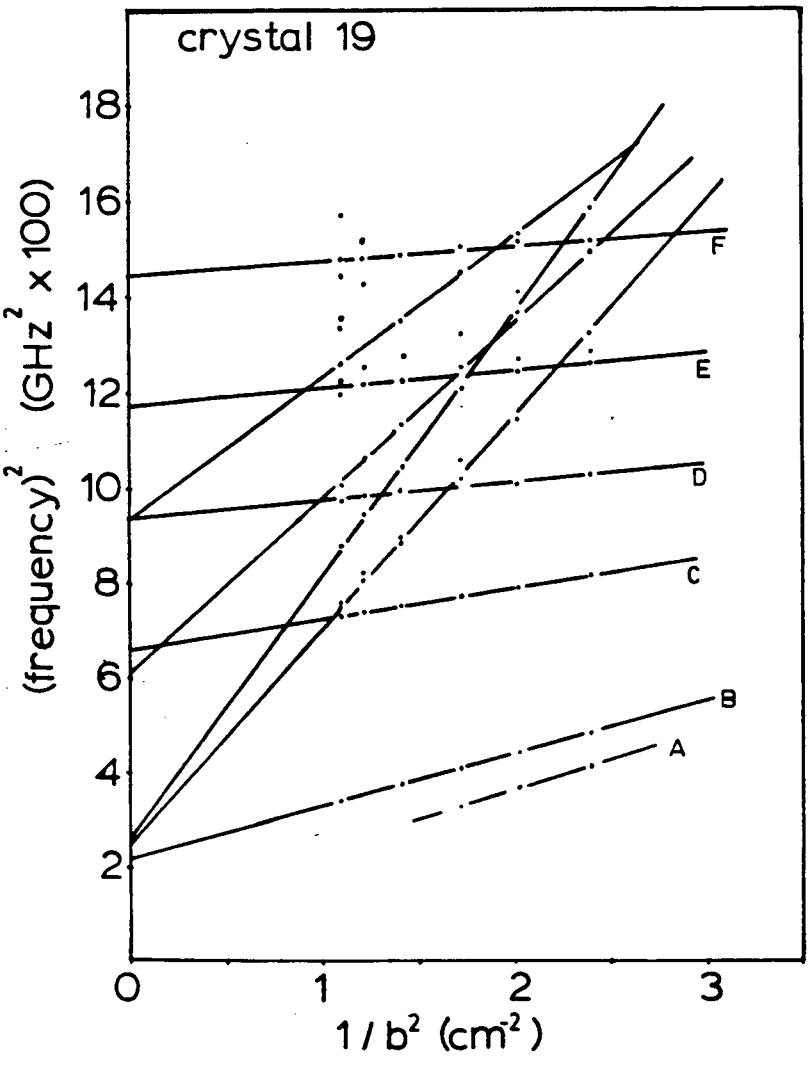

Figure 49. Dielectric resonance mode plot for TTF-TCNQ crystal 19.

References

Ashcroft, N.W., and Mermin, N.D., Solid State Physics, Holt, Rhinehart, and Winston, New York(1976)

Balkanski, M, in Optical Properties of Solids, F. Abeles (ed.), North-Holland Publishing(1972)

Bardeen, J., Solid State Comm. 13; 357(1973)

Barry, C.P., MSc. Thesis, U.B.C.(1977)

Berlinsky, A.J., Carolan, J., Weiler, L., Solid State Comm. 15, 795(1974)

Berlinsky, A.J., Reports on Progress in Physics 42, 1243 (1979)

Bosch, A., and van Bodegom, B., Acta Cryst. B33, 3013(1977)

Buravov, L., and Schegolev, I.F., Prib. i Tek. Eksp. 2, 171(1971)

Chaikin, P., Garito, A.F., Heeger, A.J., J. Chem. Phys. 58, 2336(1973)

Chaikin, P., and Beni, G., Phys. Rev. B13, 647(1976)

Chaikin, P., and Beni, G.,, Phys Rev. B13, 647(1976)

Chaikin, P., Private communication (1979)

Coll, C., Phys. Rev. B9, 2150(1974)

Comes, R., in Chemistry and Physics of One-Dimensional Metals, H.J. Keller (ed.), Plenum, New York(1977)

Conwell, E., Phys. Rev. B18; 1818(1978)

Eldridge, J.E., and Bates, F., Solid State Comm. 30, 195(1979)

Emery, V.J., in Chemistry and Physics of One-Dimensional Metals, H.J. Keller (ed.), Plenum, New York(1977)

Epstein, A.J., Etemad, S., Garito, A.F., Heeger, A.J., Phys. Rev. B5, 952(1972)

Frohlich, H., Proc. Roy. Soc. A223, 296(1954)

Hardy, W.N., Berlinsky, A.J., Weiler, L., Phys. Rev. 14B, 3356(1976)

Hardy W.N., (1979) private communication

Heeger, A.J., in Chemistry and Physics of One-Dimensional Metals, H.J. Keller (ed.), Plenum, New York(1977)

Hidy, G.M. Et al., North American Rockwell Science Centre, Thousand Oaks, California, Report NASA CR-1960, 54(1972)

Hubbard, J., Proc. Roy. Soc. A276, 238(1963)

Hubbard, J., Phys. Rev., B17, 494(1978)

Huizinga, S., Kommandeur, J., Sawatsky, G., Thole, B., Kopinga, K., de Jonge, W., Roos, J., Phys. Rev. B19, 4723(1979)

Jaklevic, R., and Saillant, R., Solid State Comm. 15, 307(1974)

Jaworski, M., Private communication to W. Hardy (1978)

Friend, R.H, Miljak, M., Jerome, D., Decker, D.L., Debray, D., J. Phys (Paris) Lett., 39, L134, (1978)

Khanna, S.K.; Ehrenfreund, E., Garito, A.F., Phys. Rev., B10, 2205(1974)

Khanna, S.K., Garito, A.F., Heeger, A.J., and Jaklevic, R., Solid State Comm., 16, 667(1975)

Klimenko, V., Krinov, V., Ovchinnikov, A., Ukrainskii, I., and Shvets, A., Sov. Phys. JETP 42, 123(1976)

Kwak, J., and Beni, G., Phys. Rev. B13, 652(1976)

Lee, P.A., Rice, T.M., and Anderson, P.W., Solid State Comm. 14, 703(1974)

Lorrain, P., and Corson, D., Electromagnetic Fields and Waves, Freeman and Co., San Fransisco(1970)

Morrow, M., Hardy, W.N., Carolan, J., Berlinsky, A.J., Weiler, L., Gujral, V., Janossy, A., Holczer, K., Mihlay, G., Gruner, G., Huizinga, S., Verwey, A., Sawatsky, G., to be published in Can. J. Phys. (1980)

Okaya, A., and Barash, L., , IRE Proc., 50, 2081(1962)

Oostra, S., Huizinga, S., Kommandeur, J., Sawatzky, G., Nechtschein, M., to be published

Osborne, J., Phys. Rev. 67, 351(1945)

Ovchinnikov, A., Sov. Phys. JETP 30, 1160(1970)

Peirels, R., Quantum theory of Solids, Oxford University Press, London(1955)

Richtmeyer, R., J. App. Phys. 10, 391(1939)

Sawatsky, G., Private communication (1979)

Statt, B.W., MSc. Thesis, U.B.C.(1979)

Toombs, G.A., Physics Reports 40, 181(1978)

Torrance, J., and Silverman, B., Phys. Rev. B15, 788(1977)

Torrance, J., in Chemistry and Physics of One-Dimensional Metals, H.J. Keller (ed.), Plenum, New York(1977)

Torrance, J., Phys. Rev. B17, 3099(1978)

Waldron, P., Theory of Guided Electromagnetic Waves, van Nostrand Rheinhold Co., London(1969)

Yee, IEEE Trans. On MTT, 13, (1965)